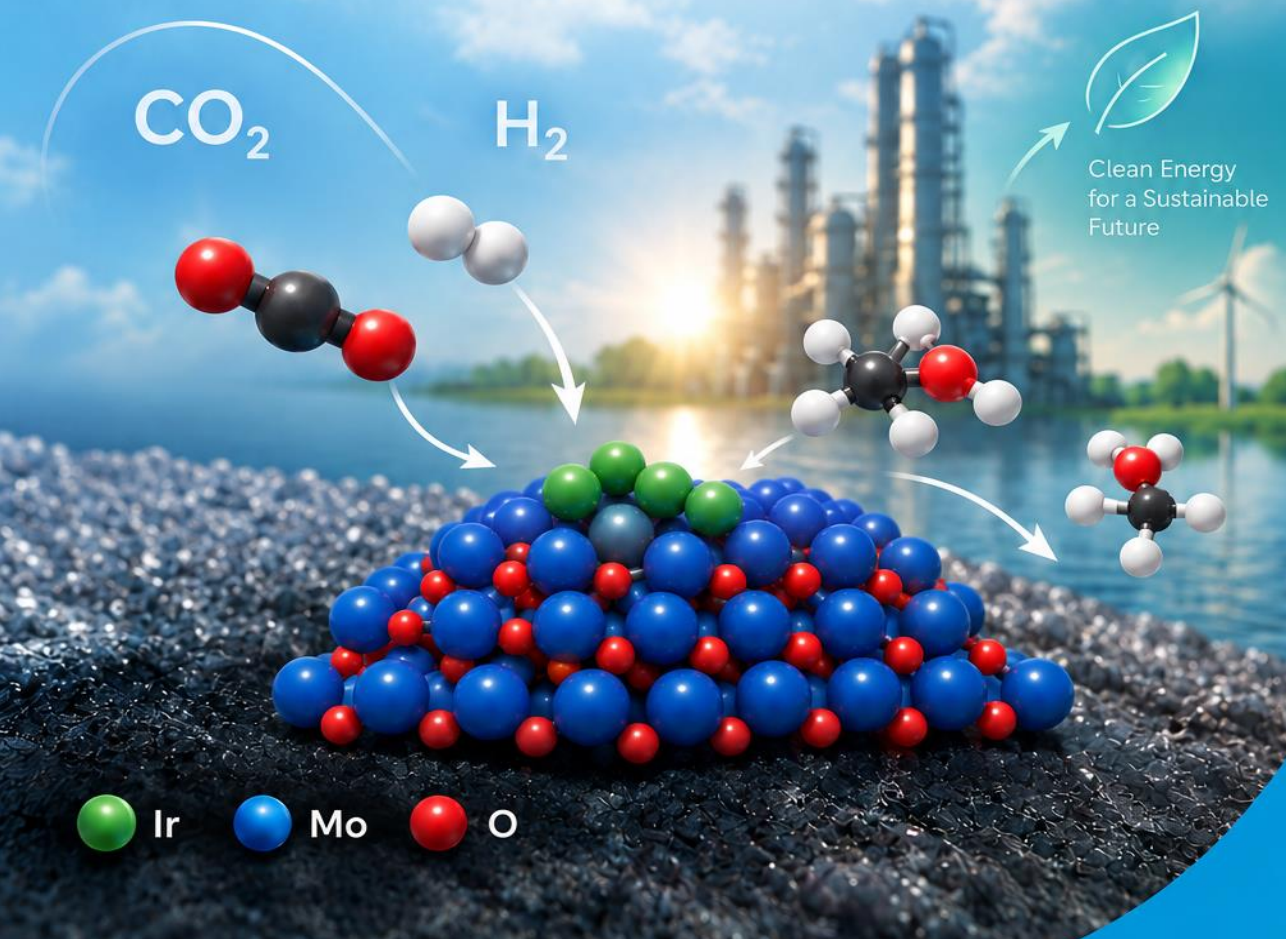
TU Delft

CO_2 Hydrogenation to Chemical Energy Carriers over Ir and Mo Containing Catalysts

by

Ahmad Hamied ALREFAEI



Proposition

accompanying the dissertation
CO_2 Hydrogenation to Chemical Energy Carriers over Ir and Mo Containing Catalysts
By Ahmad Alrefaei

1. Carbon capture and utilization (CCU) should NOT be identified as a replacement for decarbonization, but as a complementary strategy to increase storable energy sources.
2. *Operando* techniques are essential to accurately correlate catalyst structure with performance, as ex-situ characterization may not reflect the true active phase. (Chapter 2)
3. An optimal metal loading always exists in catalysts; exceeding this optimum can negatively affect the performance in several ways, due to structural and kinetic limitations. (Chapter 3)
4. Separating the effects of dispersion and loading is essential for rational catalyst design. (Chapter 4)
5. Catalyst stability in CO2 hydrogenation is strongly influenced by support surface area and metal–support interaction, particularly under RWGS conditions. (Chapter 5)
6. Scientific impact depends not only on the quality of the research but also on the scientist's ability to communicate it clearly.
7. The AI revolution will play a decisive role in accelerating catalyst discovery; however, preserving scientific critical thinking and creativity remains essential.
8. A large quantity of produced data is not a measure of high-quality science unless it is accompanied by a deep understanding, leading ultimately to meaningful and valuable conclusions.
9. A true leader stays silent in moments of success to empower others and speaks firmly in moments of crisis to protect the team.
10. Long-term success is built on consistency and determination rather than on moments of exceptional performance.

These propositions are regarded as opposable and defendable, and have been approved by the promoter Prof.dr.ir. A. Urakawa and the copromoter Dr. A.B. Bansode

CO_2 Hydrogenation to Chemical Energy Carriers over Ir and Mo Containing Catalysts

Dissertation

for the purpose of obtaining the degree of doctor
at Delft University of Technology
by the authority of the Rector Magnificus,
Prof.dr.ir. H. Bijl,
Chair of the Board of Doctorates
to be defended publicly on
Thursday, 24 September 2026, 17:30

By

Ahmad Hamied ALREFAEI

This dissertation has been approved by the (co)promotors.

Composition of the doctoral committee:

Rector Magnificus	Chairperson
Prof.dr.ir. A. Urakawa	Delft University of Technology, promotor
Dr. A. B. Bansode	Delft University of Technology, copromotor

Independent Members:

Prof.dr.ir. W. De Jong	Delft University of Technology
Prof.dr. E. A. Pidko	Delft University of Technology
Prof.dr.ir. E. J. M. Hensen	Eindhoven University of Technology
Dr. J. Ruiz-Martínez	King Abdullah University for Sciences and Technology, Saudi Arabia
Prof.dr. F. M. Mulder	Delft University of Technology, *reserve member*

Key words: CO_2 hydrogenation, iridium, high pressure, operando DRIFTS,
Printed by ProefschrifMaken
Cover by: Maryam Alquarshi/ Designer

An electronic version of this dissertation is available at: http://repository.tudelft.nl

Acknowledgements

First and foremost, I would like to thank my family for their unconditional love, patience, and support throughout my PhD journey. I am deeply grateful to my mother, father, sisters, and brother for always believing in me and encouraging me to keep going. I would also like to give my deepest thanks to my lovely wife, Maryam, for her endless support, patience, and understanding throughout these years. Abdulmalik and Abdulaziz, thank you for filling my life with love, happiness, and countless reasons to keep going; you are my greatest motivation and the most precious part of this journey. This PhD would not have been possible without all of you. I am truly grateful to have you all in my life.

I would like to express my deepest gratitude to my promoter, Prof. Atsushi Urakawa, for his solid and continuous support throughout my PhD. He suffered a lot while teaching me, but I finally made it. He was always pushing me to bring out the best version of myself. I am truly proud to have him as my father in science, and I am sure I will continue learning from him for many years to come.

A very special thank you goes to my copromotor, Dr. Atul Bansode, for his continuous support and guidance throughout my PhD. Atul has been the engine that kept pushing my PhD forward and helped me bring it to an end. I am truly grateful for everything he has done for me. He was not only my scientific copromotor, but he also taught me to become a better person.

I would also like to thank my friends Afreen, Bennie, and Jose. You are very special to me, and you have supported me throughout my entire PhD journey. I have learned a lot from each of you, both scientifically and personally. Even during the final stages of my dissertation, you continued to give me valuable advice and support. Even after I submitted my dissertation, they were asking about the feedback from the committee. People who do this are not only friends but also true sisters and brothers. I am very grateful to have shared this journey with you.

A special thanks to my Italian friend, Martino, for all his help and good times. And, of course, thank you for being the best Master's student in the universe, even though you are now doing a PhD! My sincere thanks also go to Damian, Shota, and Charlotte for their help and support during the beamtime in

Barcelona. I would also like to thank Bart, Liliana, Willy, and Harrie for their valuable technical support throughout my PhD.

I would also like to thank Min and Ezgi for the lovely moments and the beautiful presence they brought into my PhD life. Thank you, Nat, for teaching me how to work with the high-pressure setup and for your help along the way. Also, special thanks go to my other Italian friend, Donato, for his support throughout my PhD journey.

A very special thank you goes to Hisham, Pietro, Ivan, Manoj, and Dhanaji. Thank you for all the wonderful times we shared together and for making this PhD journey much more enjoyable. I am sure that the friendship we built during these years will last forever. I am very lucky to have shared so many great memories with such lovely people.

I would like to sincerely thank all my examiners for their valuable feedback and support in evaluating my PhD dissertation. Their comments and suggestions helped improve the quality and scientific rigor of this work. I am also very grateful to them for serving as members of my PhD defence committee.

Finally, I would like to thank everyone in the Catalysis Engineering groups, including the groups of Atsushi and Atul. I may forget to mention some names, but please know that every one of you has contributed to this journey in one way or another. Without your support, help, and friendship, I would not have been able to complete this PhD.

I would also like to sincerely thank Saudi Aramco for believing in me, giving me this opportunity, and supporting me throughout my PhD.

Content

Summary		v
Samenvatting		vii
CHAPTER 1	Introduction	1
CHAPTER 2:	Dynamic surface restructuring of Ir/MoO_x steering CO_2 hydrogenation toward methanol-derived products	27
CHAPTER 3	Investigating the influence of molybdenum loading on the performance of $(1.5)Ir/xMo/Al_2O_3$ catalysts in CO_2 hydrogenation to methanol	71
CHAPTER 4	Role of molybdenum dispersion in enhancing the catalytic performance of $Ir/\gamma\text{-}Al_2O_3$ for CO_2 hydrogenation to methanol	99
CHAPTER 5	On the kinetics of CO_2 hydrogenation to CO on Ir/Mo-based catalytic systems	131
Outlook		163
Curriculum Vitae		167

Summary

The increasing global energy demand, driven by population growth and industrial development, remains heavily reliant on fossil fuels, contributing significantly to climate change. Carbon capture, utilization, and storage (CCUS) has emerged as a critical strategy to mitigate CO_2 emissions while enabling the production of sustainable fuels and chemicals. Among CCUS pathways, catalytic CO_2 hydrogenation to methanol (MeOH) and MeOH-derived products represents a promising route for carbon recycling, particularly when coupled with green hydrogen. However, achieving high activity and selectivity under industrially acceptable conditions requires a deep understanding of catalyst structure and reaction mechanisms. This thesis investigates iridium–molybdenum-based catalytic systems for CO_2 hydrogenation to MeOH and its derived products, with the last study focusing on the reverse water–gas shift (RWGS) reaction.

The first part of this work examines Ir supported on different reducible oxides for CO_2 hydrogenation to MeOH and MeOH-derived products. Among the investigated systems, Ir/MoO_3 demonstrated superior activity toward MeOH-derived products, reaching 15 $mg \cdot h^{-1} \cdot g_{cat}^{-1}$ at 225 °C and 20 bar. The catalytic performance was found to be highly sensitive to the reduction temperature. Moderate reduction at 200 °C produced partially reduced Mo species (predominantly Mo^{4+}), while reduction at 400 °C generated more metallic Mo (Mo^0). These changes significantly altered MeOH selectivity. The *in situ* X-ray absorption near-edge structure (XANES) confirmed that Ir was fully reduced at 200 °C and that variations in MeOH selectivity were primarily linked to changes in the Mo chemical state. Repeated reaction cycles were found to lead to additional *in situ* Mo reduction, correlating with enhanced MeOH formation. These findings highlight that the catalytic behavior of Ir/MoO_3 is governed primarily by the redox and structural dynamics of the MoO_x support.

The second part of the thesis investigates the effect of Mo loading in (1.5)Ir/*x*Mo/Al_2O_3 catalysts (19, 32, and 48 wt% Mo). Structural characterization showed that low Mo loading resulted in highly dispersed amorphous Mo species, while higher loadings promoted the formation of crystalline MoO_3 phases. Interestingly, IrO_2 crystallites were prominent at low Mo loading but became negligible at higher Mo loading, indicating stronger Ir-Mo interactions. Catalytic testing at 300 bar revealed that low Mo loading

yielded the highest MeOH-derived product selectivity (48% at 150 °C), whereas increasing Mo loading suppressed MeOH formation. *Operando* diffuse reflectance infrared Fourier transform spectroscopy (DRIFTS) analysis revealed that higher Mo loading diminished Lewis acid-associated bidentate formate species, while monodentate formate remained unaffected. The suppression of these Lewis acid-associated intermediates directly correlated with reduced MeOH selectivity, establishing Mo loading as a critical parameter controlling surface chemistry, intermediate stabilization, and catalytic performance.

In the second part of the investigation, the low Mo-loading catalyst yielded the highest selectivity for MeOH-derived products. However, it remains unclear whether the high selectivity is primarily due to Mo loading or dispersion, as lower loadings often led to higher dispersion. To decouple the effects of dispersion, the third part of this study focuses on catalysts with identical Mo loading (32 wt%) but different Mo dispersions (high and low). The catalytic activity result demonstrated that highly dispersed Mo species enhance MeOH and MeOH-derived product selectivity. Using a reduction temperature of 400 °C for 1.5 h (R400), the highly dispersed catalyst achieved 97% MeOH-derived product selectivity, whereas the low-dispersion catalyst predominantly produced CO. *Operando* DRIFTS identified one of the bidentate formate and the monodentate formate species as essential intermediates for MeOH formation.

The Ir/Mo-based system is flexible, and its role and function can be tuned based on the condition used. To show the flexibility of the Ir/Mo-based system, the final part of the thesis explores the RWGS reaction over Ir/MoO_3 and $Ir/MoO_3/Al_2O_3$ catalysts under atmospheric pressure. Both systems exhibited complete selectivity toward CO across the investigated temperature range, confirming their suitability for RWGS. However, Ir/MoO_3 showed partial deactivation at elevated temperatures due to its low surface area and associated Ir sintering. In contrast, $Ir/MoO_3/Al_2O_3$ displayed excellent thermal stability with negligible deactivation. A detailed kinetic study was conducted for the stable $Ir/MoO_3/Al_2O_3$ catalyst. The reaction was modeled assuming direct CO_2 dissociation with C–O bond cleavage as the rate-determining step. Oxygen vacancies in MoO_x were identified as the active sites for CO_2 activation, while Ir facilitated H_2 activation and oxygen vacancy regeneration through hydrogen spillover. Kinetic parameter estimation yielded a model that accurately described the experimental data. Sensitivity analysis was performed, and based on the analysis result, it was hypothesized that CO and

H_2O adsorption is negligible, allowing simplification of the model without compromising predictive capability.

Samenvatting

De toenemende wereldwijde energievraag, gedreven door bevolkingsgroei en industriële ontwikkeling, blijft sterk afhankelijk van fossiele brandstoffen en draagt aanzienlijk bij aan opwarming van de aarde. koolstofafvang, -hergebruik en -opslag, carbon capture, utilization and storage (CCUS) is naar voren gekomen als een cruciale strategie om CO_2-emissies te beperken en tegelijkertijd de productie van duurzame brandstoffen en chemicaliën mogelijk te maken. Binnen de verschillende CCUS-routes vormt de katalytische hydrogenering van CO_2 naar methanol en methanol-afgeleide producten een veelbelovende route voor koolstofrecycling, met name wanneer deze wordt gecombineerd met groene waterstof. Het realiseren van hoge activiteit en selectiviteit onder industrieel relevante omstandigheden vereist echter een diepgaand inzicht in de katalysatorstructuur en de onderliggende reactiemechanismen. Dit proefschrift onderzoekt iridium–molybdeen-gebaseerde katalytische systemen voor CO_2-hydrogenering naar methanol en methanol-afgeleide producten, waarbij de laatste studie zich richt op de reverse water–gas shift (RWGS)-reactie.

Het eerste deel van dit werk onderzoekt Ir ondersteund op verschillende reduceerbare oxiden voor CO_2-hydrogenering naar methanol. Van de onderzochte systemen vertoonde Ir/MoO_3 de hoogste activiteit voor methanol-afgeleide producten, met een opbrengst van 15 $mg \cdot h^{-1} \cdot g_{cat}^{-1}$ bij 225 °C en 20 bar. De katalytische prestaties bleken sterk afhankelijk van de reductietemperatuur. Reductie bij 200 °C leidde tot gedeeltelijk gereduceerde Mo-(voornamelijk Mo^{4+}), terwijl reductie bij 400 °C resulteerde in meer metallisch Mo (Mo^0). Deze veranderingen hadden een significante invloed op de methanolselectiviteit. *In situ* XANES bevestigde dat Ir volledig gereduceerd was bij 200 °C en dat variaties in methanolselectiviteit voornamelijk samenhingen met veranderingen in de chemische toestand van Mo. Daarnaast werd vastgesteld dat herhaalde reactiecycli leidden tot verdere in situ reductie van Mo, wat correleerde met een verhoogde methanolvorming. Deze bevindingen tonen aan dat het katalytisch gedrag van Ir/MoO_3 voornamelijk wordt bepaald door de redox- en structurele dynamiek van de MoO_x-drager en niet door veranderingen in de oxidatietoestand van Ir.

Het tweede deel van het proefschrift onderzoekt het effect van de Mo-lading in (1.5)Ir/*x*Mo/Al_2O_3-katalysatoren (19, 32 en 48 gew.% Mo). Structurele karakterisering toonde aan dat een lage Mo-lading resulteerde in sterk gedispergeerde amorfe Mo-soorten, terwijl hogere ladingen leidden tot de vorming van kristallijne MoO_3-fasen. Opvallend was dat IrO_2-kristallieten prominent aanwezig waren bij lage Mo-lading, maar vrijwel verdwenen bij hogere Mo-gehalten, wat wijst op sterkere Ir–Mo-interacties. Katalytische testen bij 300 bar lieten zien dat een lage Mo-lading de hoogste methanol-afgeleide productselectiviteit opleverde (48% bij 150 °C), terwijl een hogere Mo-lading de methanolvorming onderdrukte. *Operando* DRIFTS-analyse toonde aan dat hogere Mo-belading de aan Lewis-zuurcentra geassocieerde bidentate formiaatsoorten verminderde, terwijl monodentaat formiaat onveranderd bleef. De onderdrukking van deze Lewis-zuur-geassocieerde tussenproducten correleerde direct met een afname in methanolselectiviteit, wat bevestigt dat Mo-belading een cruciale parameter is die oppervlaktechemie, intermediairstabilisatie en katalytische prestaties bepaalt.

Hoewel in het tweede deel werd vastgesteld dat lage Mo-belading resulteert in de hoogste methanolselectiviteit, bleef onduidelijk of deze verhoogde selectiviteit primair toe te schrijven is aan de Mo-belading zelf of aan de daarmee samenhangende hogere dispersie, aangezien lagere beladingen doorgaans leiden tot betere dispersie. Om het effect van dispersie te ontkoppelen van De samenstelling, richt het derde deel van deze studie zich op katalysatoren met een identieke Mo-belading (32 gew.%) maar met verschillende Mo-dispersies (hoog en laag). De katalytische resultaten toonden aan dat sterk gedispergeerde Mo-soorten de methanol- en methanol-afgeleide productselectiviteit aanzienlijk verhogen. Na reductie bij 400 °C gedurende 1,5 uur (R400) bereikte de sterk gedispergeerde katalysator een methanol-afgeleide productselectiviteit van 97%, terwijl de laag-gedispergeerde katalysator voornamelijk CO produceerde. *Operando* DRIFTS identificeerde één type bidentaat formiaat en het monodentaat formiaat als essentiële tussenproducten voor methanolvorming.

Het laatste deel van het proefschrift onderzoekt de RWGS-reactie over Ir/MoO_3- en Ir/MoO_3/Al_2O_3-katalysatoren bij atmosferische druk. Beide systemen vertoonden volledige selectiviteit naar CO over het gehele onderzochte temperatuurbereik, wat hun geschiktheid voor de RWGS-reactie bevestigt. Ir/MoO_3 vertoonde echter gedeeltelijke deactivatie bij verhoogde temperaturen, toegeschreven aan het lage oppervlak en de daarmee samenhangende sintering van Ir. Daarentegen vertoonde Ir/MoO_3-

Al_2O_3uitstekende thermische stabiliteit zonder significante deactivatie. Voor de stabiele Ir/MoO_3/Al_2O_3-katalysator werd een gedetailleerde kinetische studie uitgevoerd. De reactie werd gemodelleerd op basis van directe CO_2-dissociatie, waarbij de C–O-bindingbreuk als snelheidsbepalende stap werd aangenomen. Ledig zuurstof in MoO_x werden geïdentificeerd als actieve centra voor CO_2-activatie, terwijl Ir verantwoordelijk werd geacht voor H_2-activatie en regeneratie van Ledig zuurstof via waterstofoverloop. De geschatte kinetische parameters leverden een model op dat de experimentele resultaten nauwkeurig beschreef. Gevoeligheidsanalyse toonde aan dat CO- en H_2O-adsorptie verwaarloosbaar waren, waardoor het aantal kinetische parameters kon worden gereduceerd zonder verlies van voorspellende nauwkeurigheid.

1 Introduction

CO_2 hydrogenation

Summary

Human civilization's progress has always been correlated with energy consumption. Despite advances in energy technologies, fossil fuels remain the primary energy source globally. The world population is expected to reach 9.66 billion by 2050; therefore, developing sustainable and renewable energy sources is essential. Renewable technologies have grown rapidly; however, carbon-intensive industries remain dominant, making carbon capture, utilization, and storage (CCUS) a necessary solution to address this imbalance. Among CCUS strategies, CO_2 hydrogenation to methanol (MeOH) and its derivatives is a promising route for producing clean fuel and chemical feedstocks. This reaction is thermodynamically favored under low-temperature and high-pressure conditions, but it also requires highly selective catalysts to suppress side reactions. Recent research highlights iridium- and molybdenum-based catalytic systems for efficient CO_2 hydrogenation. Iridium catalysts demonstrate tunable selectivity depending on their supports, while molybdenum-based systems exhibit unique structural flexibility that enhances CO_2 activation. In this chapter, the reported efficiency of iridium-based catalysts used for CO_2 hydrogenation is explored. Furthermore, molybdenum-based materials were explored to better understand their unique role in CO_2 hydrogenation.

1.1 Energy, society, and the need for alternative fuel resources

The trajectory of human social development is primarily linked to energy consumption [1,3]. As civilizations have advanced, methods for obtaining energy have evolved; however, reliance on hydrocarbon-based fuels continues to increase. This continued reliance poses a major challenge for the future, as future global demands will necessitate the development of alternative renewable energy technologies to support a continuously growing population and its technological needs. The global population, currently estimated at approximately 8.23 billion in 2026, is expected to reach nearly 9.66 billion by 2050 [1]. Concurrently, rapid technological advancement across all sectors of society will certainly increase the demand for resources and energy. According to the International Energy Agency (IEA), global energy demand increased by 2.2% in 2024, compared to an average annual growth rate of 1.3% over the past decade, highlighting the significant rise in energy consumption in recent years. [2]. Currently, the global energy supply is predominantly derived from fossil fuels, coal, natural gas, and petroleum. These resources remain the primary feedstocks for transportation fuels, electricity generation, heating, and the production of chemicals, including plastics and agricultural fertilizers.

It is challenging to predict the proven global oil reserves, as they are frequently updated based on production capacity and the discovery of new reservoirs, as recently reported by Saudi Aramco [3]. A sudden depletion is unlikely; however, considering the economic constraints driven by the supply-demand balance, significant price instability is expected. Furthermore, the concentration of these resources in specific regions creates energy security concerns for other importing nations. Therefore, these challenges, rising energy demand, resource constraints, and mounting environmental concerns regarding greenhouse gas emissions, highlight the urgent need for innovative technologies in energy production. As a result, governments and international agencies have prioritized, published, and funded research programs dedicated to advancing cost-effective and sustainable energy solutions. These initiatives involve a wide range of approaches, including renewable power generation and carbon capture technologies, as well as the development of cleaner fuels and more efficient catalytic processes. All of this with the aim of achieving long-term decarbonization.

1.1.1 The current sources for sustainable energy

Sustainable energy production has become a basis of global strategies to address the challenges of rising energy demand and climate change. The increase in energy demand observed in 2024 was 4.3%, a significant increase compared to the previous year [2]. Different energy sources were used to compensate for the increase in energy demand. Figure 1.1 shows the contribution of each sector to this increase in the total energy demand (the 4.3% increase). As shown in Figure 1.1, renewable sources accounted for the largest share of the sources contributing to the increase in energy demand in 2024. Current sustainable energy sources include renewable technologies such as solar photovoltaics, wind power, hydropower, geothermal systems, and bioenergy, all of which provide low-carbon alternatives to fossil fuel-based generation [4]. Solar and wind energy have experienced rapid technological advancement and cost reductions, positioning them as the fastest-growing contributors to the renewable energy mix. Hydropower remains the largest renewable source globally, while bioenergy and geothermal systems contribute to electricity and heat production in certain regions [2,4,5]. This confirms the significant return on investment in renewable energy research, encouraging global organizations and governments to further support and fund this research. However, despite these advances, the persistence of carbon-intensive industries highlights the need for complementary strategies that utilize carbon.

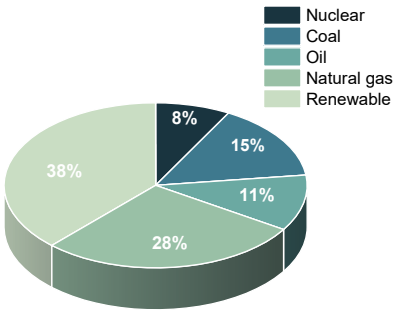


Figure 1.1 Energy sectors contribution to the total increase in energy demand in percentage at 2024 [2]

As such, carbon capture, utilization, and storage (CCUS) has emerged as a critical technology, offering direct mitigation of emissions from existing technology while converting CO_2 into valuable materials, thereby moving toward a sustainable and circular energy system. CO_2 hydrogenation to chemical energy carriers constitutes a critical technology within the broader framework of CO_2 utilization. Its significance stems from the dual advantage of utilizing CO_2, an abundant carbon resource, and producing chemical energy carriers to meet rising global energy demands. Moreover, the widespread availability of CO_2 makes this technology globally accessible. When coupled with green hydrogen produced from renewable energy sources, CO_2 hydrogenation offers a pathway toward sustainable carbon in fuels and chemicals.

1.2 CO_2 hydrogenation to valuable chemicals

Since the Industrial Revolution, the concentration of CO_2 in the atmosphere has increased significantly, primarily due to the combustion of fossil fuels [6]. Given the impossibility of stopping CO_2 emissions, global attention has shifted towards its conversion into valuable materials to mitigate its environmental impacts [7]. Among the various technologies being used to utilize CO_2, the catalytic conversion of CO_2 is a promising approach for producing highly desired products such as methanol (MeOH), methyl formate (MF), dimethyl ether (DME), or carbon monoxide (CO) [8]. These products can serve as a crucial feedstock in the chemical industry and find growing utilization in various chemical processes [8]. Additionally, the chemical energy carriers, such as MeOH, can be used as chemical fuels for zero-emission applications due to their high energy content. Table 1.1 shows the lower heating value (LHV) of currently used fuels and chemical fuels. Although conventional fuels, such as gasoline and diesel, can produce more energy during combustion, they contribute significantly to CO_2 emissions, necessitating the need for more sustainable fuels, such as MeOH.

Table 1.1 Comparison between the lower heating value (LHV) in MJ/kg for the chemical fuels and the currently used fuels

Fuel	LHV (MJ/kg)	References
MeOH	22.0	[9]
DME	28.8	[10]
Gasoline	44	[11]
Diesel	42.5	[12]

CO_2 hydrogenation to MeOH is an exothermic reaction that proceeds via Eq. 1, favoring low temperatures. However, at low temperatures, the activation rate of CO_2 is slow, necessitating the presence of a highly active and selective catalytic system. Non-selective catalysts may result in the competing methanation reaction, known as the Sabatier reaction, which maximizes methane (CH_4) production (see Eq. 2) [13,14]. Additionally, increasing the reaction temperature will activate the endothermic reaction, reverse water-gas shift reaction (RWGS), as shown in Eq. 3, thereby maximizing CO production. It is worth noting that maximizing CO production at low temperatures is also considered an attractive approach to reduce the high energy demand for this reaction. However, a highly selective catalytic system is also required to activate the CO_2.

$CO_2 + 3H_2 \rightleftharpoons CH_3OH + H_2O$ $\Delta H_{298\ K,\ 50\ bar} = -40.9$ kJ/mol (Eq. 1) [17]

$CO_2 + 4H_2 \rightleftharpoons CH_4 + 2H_2O$ $\Delta H_{(298\ K,\ 50\ bar)} = -165$ kJ/mol (Eq. 2) [18]

$CO_2 + H_2 \rightleftharpoons CO + H_2O$ $\Delta H_{(298\ K,\ 50\ bar)} = 49.8$ kJ/mol (Eq. 3) [17]

According to Le Châtelier's principle, applying high pressure in the MeOH synthesis is thermodynamically favorable, shifting the reaction to the right [8,15]. This is due to the reduction in the number of molecules during the reaction, from 4 to 2 moles, as shown in Eq.1. It is worth noting that high pressure and low temperature are also favorable for CO_2 hydrogenation to form CH_4, underscoring the need for a selective catalytic system [13,14]. Despite extensive research, most investigated low-temperature catalytic systems have exhibited suboptimal performance concerning CO_2 conversion and selectivity towards MeOH-derived products [16].

1.2.1 Importance of high-pressure conditions in CO_2 hydrogenation to MeOH-derived products

High-pressure conditions are critical in the efficient catalytic hydrogenation of CO_2 to MeOH and its downstream derivatives, such as DME and MF. The thermodynamic equilibrium calculations confirm that increasing the pressure would increase conversion, reaching almost a complete conversion towards MeOH, as shown in Figure 1.2 (a) [19]. This elevated pressure is believed to improve the availability of CO_2 and H_2 at the catalyst surface by increasing their concentrations and promoting higher surface coverage of reactive intermediates, as presented in Figure 1.2 (b) [20]. The increase in the surface coverage of reactive intermediates leads to more favorable kinetics and, if a selective catalytic system is present, often improved selectivity toward MeOH.

Additionally, high-pressure operation increases molecular collisions, reactant concentration, and possibly diffusion rates within the catalyst's pores, which generally help minimize mass transfer limitations (Fick’s law) in the catalytic system [19,20]. Exception for certain cases, where the diffusivity is highly affected by the pressure. Moreover, in more complex reaction systems where MeOH is further reacted to form DME or MF, high pressure enhances the thermodynamic driving force and product phase transition. In these tandem reaction systems, the continuous formation and possible condensation of MeOH near the active sites will result in higher product selectivity toward DME or MF (via dehydration to DME or esterification to MF) [21-24]. The condensation is often pressure-dependent, as it can easily be achieved at elevated pressures.

The importance of MeOH condensation was also recognized during the reaction equilibrium study of MeOH synthesis, where the Soave-Redlich-Kwong (SRK) equation of state has been the standard thermodynamic model for describing reaction equilibria in MeOH synthesis from syngas. The model was mainly used to represent the nonideal gas behavior. However, the SRK equation exhibits limitations at high pressure and low temperature conditions, where deviations between theoretical predictions and experimental observations become substantial. These deviations arise primarily from the condensation of MeOH and water into a liquid phase, which was not accounted for in the SRK equation. To address this gap, another modified SRK-based model was developed that resolves both phase and chemical equilibria for MeOH synthesis [25]. Their approach aligns with the experimental data obtained at 190-280 °C and 200 bar, performed in a packed-bed reactor. This finding confirmed the role of condensation in directing the reaction equilibrium [25].

Additionally, in systems that use different processes to achieve higher product purity, high pressure can help integrate the reaction and separation steps, thereby improving energy efficiency and potentially minimizing the space needed for additional equipment. Moreover, applying high-pressure conditions also enhances heat transfer, which is notably beneficial in exothermic systems, such as CO_2 hydrogenation to MeOH, where thermal management is essential for controlling the reaction. Mass and heat transfer could also be enhanced by applying high pressure if the CO_2 phase is shifted to a supercritical state [25].

Furthermore, in multiphase or liquid-phase systems, increased pressure raises the solubility of gaseous reactants, which is crucial for maintaining sufficient reactant availability in the liquid phase [25]. This is particularly important when using liquid solvents or reaction media that require adequate hydrogen dissolution. Lastly, in membrane-assisted systems, high pressure can be used to create pressure gradients that selectively remove products, such as MeOH or H_2O, during the reaction, leading to higher single-pass conversions by keeping the reaction away from equilibrium.

In summary, the synthesis of chemicals such as MeOH represents a well-established example of how high-pressure conditions effectively drive equilibrium-limited reactions forward [19,26]. Although a catalytic system is required for this process, high pressure is also a key factor in improving overall performance. However, despite the high energy and safety trade-offs associated with high-pressure operation, the overall benefits, including higher yield, greater selectivity, better control of phase behavior, and the potential integration of different processes, often make the disadvantages less critical, particularly in processes aiming for scalable and sustainable CO_2 valorization. When suitably engineered,

high-pressure CO_2 hydrogenation systems can also align with key principles of green chemistry, such as minimizing waste, by enabling compact, efficient, and continuous processing routes for converting CO_2 into high-value chemical feedstocks.

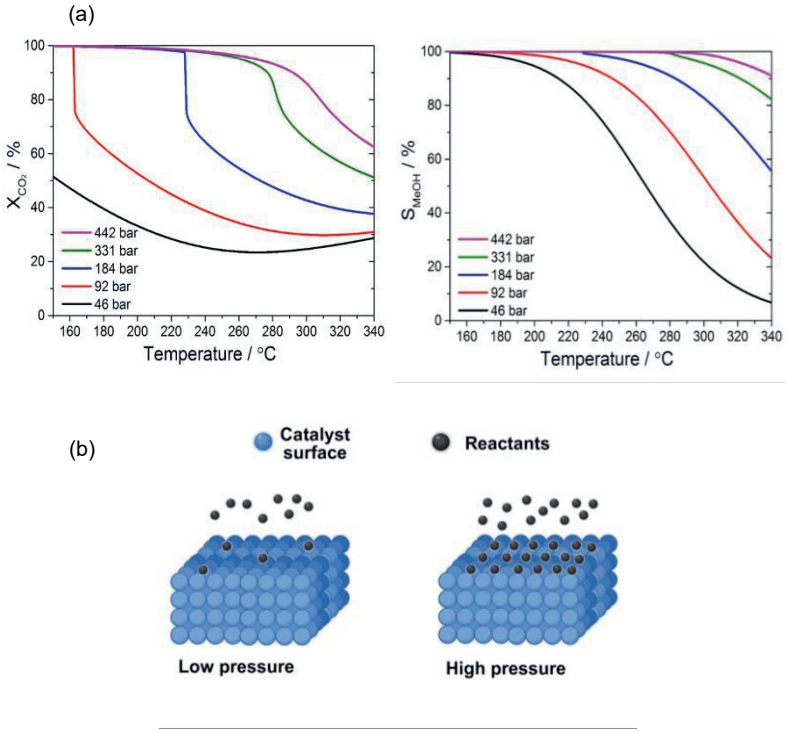


Figure 1.2 (a) Equilibrium CO_2 conversion and MeOH selectivity at different temperatures and pressures with H_2/CO_2 ratio mixtures of 3 [19]. Reproduced from [19] under the CC BY-NC-ND 4.0 **(b)** Difference in the surface coverage between two surfaces. The left is under low pressure, and the right is under high pressure

1.2.2 Catalytic systems for CO_2 hydrogenation

Several catalytic systems were investigated for CO_2 hydrogenation to MeOH-derived products, as shown in Figure 1.3 [8]. Most of these catalytic systems were tested at moderate to high temperatures. While elevated temperatures accelerate the reaction, they simultaneously reduce the saturation concentration of the condensable product, MeOH. Consequently, selecting an appropriate catalytic system that enables sufficient conversion at lower temperatures, where condensation is more favorable, is highly desirable. The availability of highly active and selective catalysts for different applications has opened up new pathways for

designing and engineering suitable catalytic systems for higher MeOH production. The catalyst design process should begin with selecting the most suitable active metal. Subsequently, an appropriate support should be chosen to ensure optimal metal-support interactions.

1.2.2.1 Copper (Cu)-based catalysts

The commercial catalyst ($Cu/ZnO/Al_2O_3$) used for syngas to MeOH has demonstrated optimal performance in CO_2 hydrogenation to MeOH. Notably, higher MeOH selectivity was observed when the feed composition was adjusted with CO [27]. The addition of CO_2/CO mixture was reported to help in optimizing the Zn state by keeping both metallic Zn (CO as a reducing agent) and ZnO particles (CO_2 as an oxidizing agent) [27]. The mixture of both Zn oxidation states was found to enhance MeOH production. Moreover, a series of transition metals with different combinations was tested, as shown in Figure 1.3. These catalytic systems were tested over a range of temperatures owing to their pronounced hydrogenation activity. At low temperatures, the methanation reaction prevailed, whereas at higher temperatures, the RWGS reaction was dominant, which makes this catalytic system optimal for CO production at high temperatures [28-31].

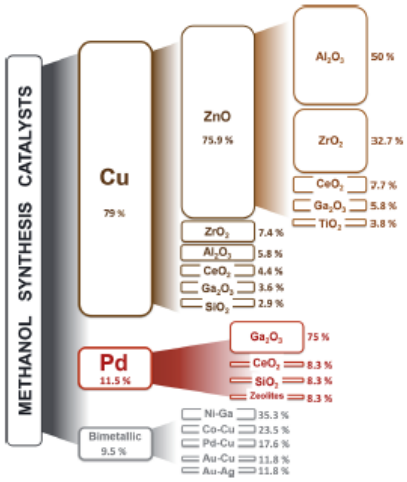


Figure 1.3 The catalytic systems reported in the literature for CO_2 hydrogenation to methanol. The percentages shown are derived from an analysis of approximately 200 publications from 2006 to 2016 [8]. Reproduced from [8] under the CC BY-NC-ND 4.0.

1.2.2.2 Rhenium-based catalysts

Recently, the rhenium (Re)-catalytic system has shown an outstanding performance in low-temperature CO_2 hydrogenation to MeOH [29,32]. The Re was impregnated onto several supports, and its performance was remarkable, with a MeOH selectivity of 82% over the TiO_2 support in the batch system [29]. The reaction conditions used for this investigation were 150 °C and 60 bar. The Re/TiO_2 was further investigated, but it was tested in a continuous-flow system at 150 °C and a high pressure of 331 bar [32]. The results show comparable performance to the commercial catalyst at low temperatures, with even better stability, as shown in Figure 1.4 (a) [32]. The investigation of the reaction mechanism over Re/TiO_2 indicates that the presence of both metallic Re^0 and $Re^{\delta+}$ cation is essential for the selective conversion of CO_2 to MeOH, as shown in the simplified figure in Figure 1.4 (b) [32]. The metallic Re^0 species is crucial in facilitating hydrogen dissociation, while the $Re^{\delta+}$ cation species activates the CO_2 molecule. Both functions contribute to the overall efficiency of the process [32]. However, Re species exhibit complex interactions with the support, leading to the coexistence of multiple oxidation states. Among these, the Re^0 - Re^{4+} oxidation state range has been suggested to be the most favorable for enhanced MeOH formation [32]. This narrow oxidation state implies that Re-based catalysts must be carefully treated and maintained under specific conditions to achieve optimal performance, limiting their flexibility for further catalyst optimization or process upgrading during the upscaling.

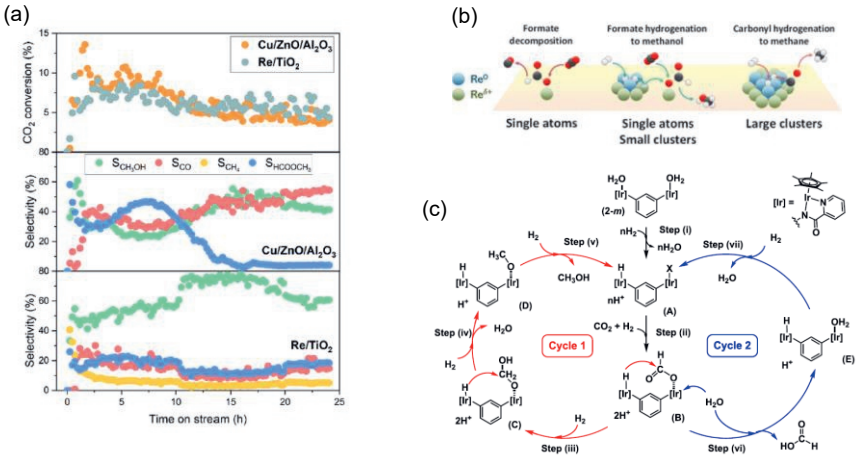


Figure 1.4 (a) Comparison of the CO_2 conversion and product selectivity between the $Cu/ZnO/Al_2O_3$ and 3 wt% Re/TiO_2 in CO_2 hydrogenation, H_2/CO_2 = 3, T = 150 °C, and P = 331 bar [32] **(b)** The proposed reaction mechanism of CO_2 hydrogenation over Re/TiO_2 system [32]. Both figures a and b Reproduced from [32] under the CC BY-NC-ND 4.0 **(c).** The proposed CO_2 hydrogenation mechanism for Ir-complex under solid-gas system [33]. Reproduced from [33] under the CC BY-NC-ND 4.0

1.2.2.3 State of the art in Iridium-based catalysts

Iridium (Ir)-based catalysts have attracted growing interest in CO_2 hydrogenation due to their unique ability to activate hydrogen at low temperatures (100 -175 °C) and to tune product selectivity by varying the support type [34-38]. Mechanistic studies of low-temperature CO_2 hydrogenation over an Ir complex system in a gas-solid reaction revealed unique behavior comparable to that of the Re-based system, which is expected to account for the higher MeOH selectivity observed over the Re system [33]. The findings indicate that the presence of two distinct Ir sites, separated by a specific distance and functioning synergistically, is critical for achieving high MeOH selectivity [33]. It is proposed that these dual sites facilitate the concurrent activation of CO_2 molecules and the dissociation of H_2, thereby optimizing the pathway for MeOH production, as shown in Figure 1.4 (c). These similarities between Re and Ir make the investigation of heterogeneous Ir-based catalytic systems for low-temperature CO_2 hydrogenation a highly promising path for further research.

Additionally, in heterogeneous systems, Ir is typically dispersed well on oxide supports, and the support's nature plays a significant role in determining both catalytic performance and the mechanistic pathway. The reducible supports have attracted more attention for their ability to enhance CO_2 activation and their interactions with the metal, which can form a unique metal-support interface [39-42]. The metal-support interactions of Ir species with the support significantly influence the formation of oxygen vacancies, which can be critical for stabilizing the active intermediates [38]. Consequently, varying the reducible support type can markedly alter both the overall activity and the specific function of Ir in the hydrogenation process.

1.2.2.3.1 Iridium over indium oxide (Ir/In_2O_3)

Shen *et al.* reported the preparation of highly active Ir/In_2O_3 catalysts for CO_2 hydrogenation to MeOH using the incipient wetness impregnation method. At 300 °C, 5 MPa, and $H_2/CO_2 = 4$, increasing the Ir loading significantly enhanced both CO_2 conversion and MeOH selectivity. The optimal 10 wt% Ir/In_2O_3 catalyst converted 17.7% CO_2 with over 70% MeOH selectivity, yielding a space-time yield of 0.765 g. g_{cat}^{-1} h^{-1}. Detailed characterization and DFT calculations identified the active site as the Ir/In_2O_3 interface, stabilized by strong metal-support interactions (SMSI). This interface promotes high Ir dispersion and creates oxygen vacancies for CO_2 activation, a common feature of many effective In_2O_3-based systems [38,43,44]. The primary role of Ir was to enhance hydrogen dissociation and spillover, generating surface vacancies while preventing over-reduction of the In_2O_3 support. This mechanistic insight is critical; unlike systems that follow the formate pathway, Ir/In_2O_3 primarily utilizes the RWGS route. However, a key limitation persists: significant activity requires high temperatures (>300 °C). This

high-temperature condition primarily limits the equilibrium, which has a substantial impact on MeOH selectivity, as discussed in Section 2.1.

1.2.2.3.2 Iridium over cerium oxide (Ir/CeO_2)

In a study by Li et al., the influence of the strong metal-support interaction (SMSI) on product selectivity in CO_2 hydrogenation was demonstrated using Ir/CeO_2 catalysts [36]. The authors developed a ligand-free synthesis method to produce highly dispersed Ir nanoparticles with sizes ranging from 1.0 to 2.2 nm by varying the Ir loading from 5 to 20 wt%. The catalytic performance at 300 °C revealed a dramatic selectivity switch: while 20 wt% Ir/CeO_2 functioned primarily as a methanation catalyst (88% CH_4 selectivity at 8.8% CO_2 conversion), 5 wt% Ir/CeO_2 exclusively produced CO (>99% selectivity at 6.8% conversion). This variation in product formation is attributed to both the particle size and the chemical state of the Ir species. Higher Ir loadings led to metallic Ir^0 particles active for deep hydrogenation to CH_4. In contrast, lower loadings facilitated a stronger SMSI, resulting in partially oxidized $Ir^{\delta+}$ species. The primary role of Ir in this system is to dissociate H_2, but its chemical state critically determines the reaction intermediates. The partially oxidized surface weakens the adsorption of CO (carbonyl species), favoring its desorption as the final product rather than further hydrogenation to CH_4. Therefore, tuning the chemical state of Ir via SMSI is a powerful strategy for steering catalytic selectivity. In general, the Ir/CeO_2 system performed well in terms of conversion, with CO and CH_4 as the only detected products, with no observable MeOH.

1.2.2.3.3 Iridium over titanium oxide (Ir/TiO_2)

In an investigation to demonstrate the effect of SMSI on tuning selectivity, Zhang *et al.* reported that the product distribution of CO_2 hydrogenation over Ir/TiO_2 catalysts could be entirely switched from CH_4 to CO by varying the catalyst's pretreatment temperature [37]. The authors prepared a series of catalysts, represented as Ir/TiO_{2-x} (where x is the reduction temperature from 200 to 700 °C), which all maintained highly dispersed, and similarly sized Ir nanoparticles (~1.2 nm). The catalytic performance at 280 °C revealed a systematic evolution in selectivity: catalysts reduced at low temperatures (≤300 °C) were exclusively selective to CH_4 (near 100%), while those reduced at high temperatures (≥600 °C) produced exclusively CO (>99%), as shown in Figure 1.5 (a). This fascinating selectivity switch was not due to changes in Ir particle size or its chemical state (which became more metallic with higher reduction temperature), but was directly correlated to the formation of a reduced TiO_x overlayer that encapsulated the Ir nanoparticles, a classic manifestation of SMSI [37,45]. Catalyst characterization confirmed that higher reduction temperatures led to more extensive encapsulation, progressively blocking the Ir sites as shown in Figure 1.5 (b). Exposed metallic Ir sites are highly active for CO dissociation and deep hydrogenation to CH_4, while the SMSI, where the TiO_x overlayer is

formed, physically covers these sites. This encapsulation process is suggested to suppress the methanation pathway but still enables the RWGS reaction to proceed on the TiO_x surface or at the Ir-TiO_x interface, leading to exclusive CO production. The investigation demonstrates that SMSI can be carefully engineered to physically tune the active sites and steer reaction pathways without altering the intrinsic properties of the metal. However, it also shows that Ir's role can be modified by the changing of the pre-treatment method, which can entirely shift the product selectivity. In addition, it can be observed from the catalytic activity that the Ir/TiO_2 mainly results in the production of CO and CH_4 [29,37].

1.2.2.3.4 Iridium over molybdenum oxide (Ir/MoO_3)

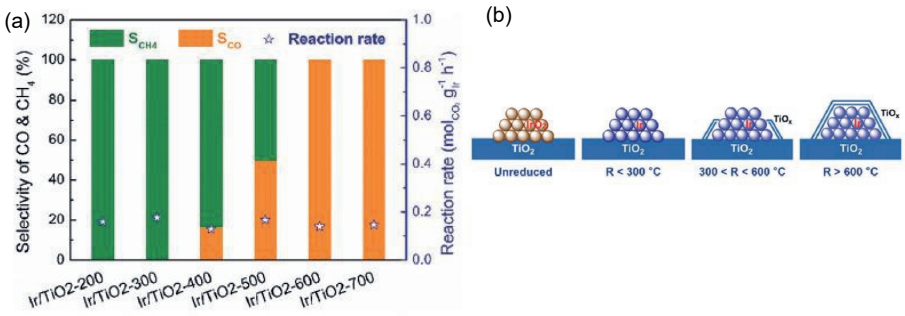


Figure 1.5 (a) CO_2 conversion and product selectivity of Ir/TiO_2 system for CO_2 hydrogenation at different reduction temperatures. The reaction conditions: 280 °C, 0.1 MPa, space velocity 9000 mL h^{-1} g_{cat}^{-1}, and $H_2/CO_2/N_2$ = 70/20/10 [37]. **(b)** Simple schematic of the structural evolution of Ir/TiO_2. The purple color of Ir species indicates the reduction of Ir NPs, while the yellow color indicates unreduced Ir species [37]. Both figures reproduced from [37] under the CC BY-NC-ND 4.0

Sun *et al.* demonstrated a highly efficient and stable catalyst for CO_2 conversion via the RWGS reaction, utilizing an Ir-promoted molybdenum oxide system synthesized via flame spray pyrolysis [46]. The catalyst exhibited exceptional catalytic activity, with CO_2 conversion of 44%, and achieved a CO production rate of 17.5 mol. g_{cat}^{-1} h^{-1} at 600 °C. The catalyst was remarkably stable over 2000 hours without deactivation. The key findings of this investigation reveal that trace amounts of Ir (as low as 0.02 wt%) act as a structural promoter, facilitating the formation of an oxygen-deficient $Mo_{17}O_{47}$ phase. The formation of this phase ($Mo_{17}O_{47}$) enables a carburization under reaction conditions to form unsaturated molybdenum oxycarbide (MoO_xC_y) surface species on a cubic α-MoC support. These MoO_xC_y sites are identified as the active centers responsible for this system's high activity and stability. Isotope labeling and DFT calculations further confirmed a carbon cycle mechanism, wherein CO_2 inserts into Mo vacancies and CO is released by extracting carbon from the oxycarbide lattice, a

pathway more favorable than the conventional redox route, as shown in Figure 1.6. The work highlights the role of Ir not as an active site but as a critical promoter that enhances reducibility and accelerates carburization to form a highly active RWGS catalyst.

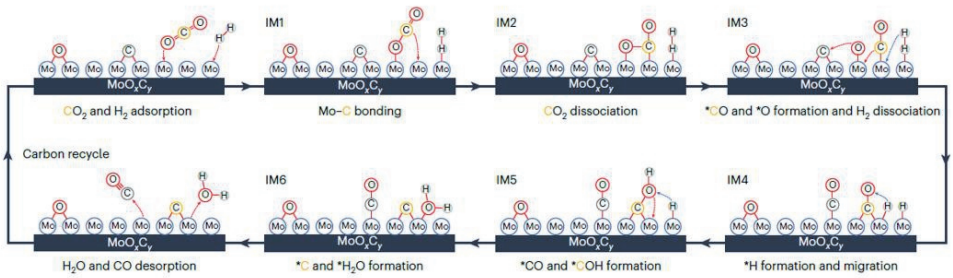


Figure 1.6 The proposed reaction mechanism for the RWGS reaction from the DFT calculations. [46] Reproduced from [46] under the CC BY-NC-ND 4.0.

1.2.2.3.5 Summary of the Ir-based systems

Among the various Ir-based catalytic systems explored for CO_2 hydrogenation, the role of Ir is profoundly influenced by its support, which governs its chemical state, dispersion, and interactions with the support and active intermediates. It was found that the Ir on In_2O_3 enhances hydrogen dissociation and spillover, promoting MeOH formation via the RWGS route. However, its chemical state on CeO_2 (influenced by SMSI) also switched selectivity between CO and CH_4. Additionally, its function on TiO_2 can be physically covered by an SMSI-induced overlayer, allowing it to exclusively produce CO. Finally, the Ir/MoO_3 system represents a significant change, where Ir acts not as a conventional or promotional active site, but as a structural promoter. In this unique case, traces of Ir facilitate the formation of a defective $Mo_{17}O_{47}$ precursor that undergoes in situ carburization under reaction conditions to generate highly active MoO_xC_y sites for RWGS reaction. This evolution in function from promotional effect (Ir/In_2O_3) to conventional active site (Ir/CeO_2 and Ir/TiO_2) to structural promoter (Ir/MoO_3) highlights the critical and versatile influence of the support in defining the role of Ir, which indicates the importance of further investigating these complex systems.

1.2.2.4 Molybdenum-based catalysts

While noble metals have dominated the landscape of CO_2 hydrogenation catalysis, earth-abundant molybdenum (Mo)-based catalysts have emerged as a promising class of materials. Sun *et al.* exemplifies a novel example in Mo-based

catalysis, where the role of the metal was shifted from a traditional active site to a structural promoter that facilitates the in situ formation of a highly active site for RWGS [46]. The reaction mechanism shown in Figure 1.7, explored by DFT, clearly indicates the unique flexibility of Mo species as a support (especially MoO_3) in activating CO_2 molecules and producing CO. On the other hand, Mo as a support was not only reported for the RWGS reaction but also for MeOH synthesis, where Mo was reported to boost MeOH formation. For instance, the distinct approach to MeOH reported by Kuwahara et al. demonstrated the efficacy of a platinum-supported oxygen-deficient molybdenum suboxide catalyst (Pt/H_xMoO_{3-y}) for liquid-phase CO_2 hydrogenation under mild conditions (200 °C, 4.0 MPa). [47] The catalyst exhibited a notable MeOH formation rate of 1.53 mmol. g_{cat}^{-1} h^{-1} at 25% CO_2 conversion and 33% MeOH selectivity. The result indicates that the bifunctionality of the system: the quasi-stable H_xMoO_{3-y} support, rich in oxygen vacancies and low-valence Mo species (Mo^{5+}/Mo^{4+}), served as the site for activating CO_2 molecules. In addition, active noble metal was found to be responsible for the subsequent hydrogenation of the active intermediate to MeOH. In conclusion, the investigation of Pt/H_xMoO_{3-y} highlights the critical importance of Mo species in CO_2 hydrogenation to MeOH, eventually boosting MeOH formation.

Another example of the unique role of Mo is the study reported by Toyao et al., which focused on achieving MeOH synthesis under notably mild conditions. It is reported that a Pt-MoO_x/TiO_2 catalyst, prepared by sequential impregnation, demonstrated exceptional performance for CO_2 hydrogenation to MeOH. Under low-temperature conditions (150 °C, 6 MPa total pressure), the optimized catalyst with 3 wt% Pt and 30 wt% MoO_x ($Pt(3)/MoO_x(30)/TiO_2$) achieved a remarkable 73% yield of MeOH at 48 hours, a value approaching the thermodynamic equilibrium and far surpassing the performance of an industrial $Cu/ZnO/Al_2O_3$ catalyst under the same conditions [30]. A key finding was the critical synergy between the active noble metal and the reduced MoO_x species, which requires further investigation. The proposed mechanism suggests a bifunctional role: metal nanoparticles act as the primary site for H_2 dissociation and activation, while reduced MoO_x species (likely possessing oxygen vacancies) are responsible for the adsorption and activation of CO_2. This work opens the way for further investigation and understanding of the exact role of Mo species in enhancing MeOH production.

In addition, the catalytic versatility of Mo-based materials, specifically MoO_3, is often attributed to the redox flexibility of the Mo species under reaction conditions. A closer analysis of the MoO_3 structure is essential to understand this property. Mo^{6+} can form several structurally distinct oxides (see Table 1.2), each with unique applications. Among these, the orthorhombic phase is predominant in catalysis due to its high thermodynamic stability. Its primary function is often linked to the

formation of oxygen vacancies (OVs), which are crucial for processes like CO_2 activation. The possible existence of mixed valency Mo^{6+}, Mo^{5+}, and Mo^{4+} under the reaction conditions for this structure could indicate the formation of these OVs as reported previously [47-49].

Density functional theory (DFT) calculations indicate these vacancies form preferentially at terminal oxygen (O_t) sites located between bilayers along the a-axis (Figure 1.7) [48]. Their formation creates two adjacent Mo^{5+} species, which induces an expansion of the van der Waals gap along the b-axis, increasing interlayer spacing. Structurally, the expansion of the van der Waals gap along the b-axis was reported from 13.886 Å in fully oxidized MoO_3 to 14.062 Å in the oxygen-deficient material [21,48].

However, the literature debates the most favorable site for vacancy formation. Contrary to the above, one investigation found that OVs form readily at intralayer oxygen sites rather than at the O_t sites within the van der Waals gap [49,50]. This specific vacancy placement induced lattice distortion, while the overall α-MoO_3 crystal structure remained preserved. This ongoing debate highlights the structural flexibility of MoO_3 and underscores the need for further investigation to understand its structure-activity relationship.

Beyond OVs, another fascinating aspect of this system is the formation of hydrogen molybdenum bronzes (H_xMoO_{3-y}). These reduced phases exhibit several distinct structures (phases) depending on the hydrogen content (x) and the position of the incorporated protons. Phase I, where the hydrogen content x is between 0.23 and 0.4, is thermodynamically stable and mainly forms protons in a cluster of 6 O-H groups with corner-sharing oxygen atoms in the channels [51,52]. Another phase (Phase II), where the hydrogen content x is between 0.85 and 1.04. In this phase, the protons predominantly reside as -OH_2 groups in the van der Waals gap, bonded to terminal oxygen atoms [51]. This bronze phase exhibits high proton conductivity among other phases, as the protons are primarily located within the van der Waals gaps, rather than in the channels. Another metastable phase exists in Phase II, where x is between 0.6 and 0.8 (Phase IIa). In this phase, the protons are positioned within the layer and in the terminal (Van der Waals gap) [51]. The disorder in the proton position causes a high proton conductivity and destroys the crystallite structure of the MoO_3. Phase III, where x is between 1.55 and 1.72, is the most thermodynamically stable phase [52]. In this phase, the protons are also located in the van der Waals gaps, but with a higher density. This ordering creates an extensive hydrogen bond network that stabilizes the structure [52]. In conclusion, the exceptional catalytic and functional properties of MoO_3 are fundamentally governed by its remarkable structural flexibility. This can be observed through two key phenomena: the debated formation of OVs at various

lattice sites, which modulates their oxidation state and reactivity, and the formation of HMB with distinct phases, where the proton position dictates properties such as stability and proton conductivity.

Table 1.2 MoO_3 structures reported in the literature.

Structure Type	Symmetry	Typical Synthesis Method	Key Application Areas	Primary Source
α-MoO_3	Orthorhombic	Calcination >450 °C	Batteries, Catalysis, Sensing	[53,54]
β-MoO_3	Monoclinic	Moderate Temp. (300-400 °C)	Catalysis	[55]
h-MoO_3	Hexagonal	Low-T Hydrothermal	Ion Exchange, Precursor, Catalysis	[53,56]
MoO_3-II	Monoclinic, High-Pressure	High Pressure (>3 GPa)	-	[57,58]
Amorphous	-	Sputtering, Sol-Gel	Electrochromic, Sensors, Catalysis	[53,59,60]

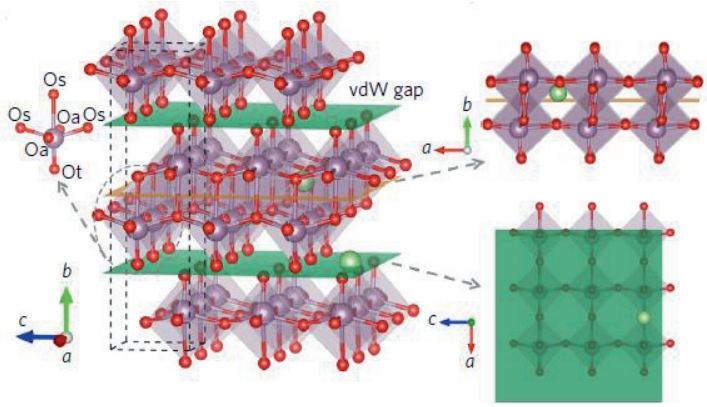


Figure 1.7 The crystal structure of MoO_3, which includes bilayers formed by edge-sharing MoO_6 octahedra (shown in grey). The bilayers are set along the b-axis (Green plane) and connected together by weak van der Waals interactions. The main framework includes three different types of oxygen atoms: the terminal oxygen (O_t), forms a Mo-O_t bond that extends perpendicularly to the van der Waals gap (shown in green), O_a, connects asymmetrically to two Mo atoms along the a-axis, and the symmetric oxygen (O_s), which exhibits three-fold coordination, forming two shorter Mo-O bonds along the [001] direction and one longer bond along [010] [48]. Reproduced from [48] under the CC BY-NC-ND 4.0

1.3 Summary

CO_2 hydrogenation to chemical energy carriers can be a highly selective technology for minimizing the carbon footprint and closing the gap for the high energy demand. Different catalytic systems have shown a potential for further investigation due to their high performance. However, most of these catalytic systems have shown poor performance at low temperatures. This review outlines the diverse landscape of catalysts for CO_2 hydrogenation, highlighting a clear structure-activity relationship where the support material critically dictates the reaction pathway and product selectivity. For noble metal systems, particularly Ir-based catalysts, the support's nature governs the catalytic performance via strong metal-support interactions (SMSI), steering selectivity between MeOH, CH_4, and CO. A notable exception is the Ir/MoO_3 system, where trace Ir acts not as an active site but as a structural promoter, facilitating the formation of a highly active molybdenum oxycarbide phase for the RWGS reaction. Concurrently, Mo-based catalysts demonstrate exceptional versatility. Their catalytic flexibility stems from the unique structural properties of MoO_3, including its ability to form oxygen vacancies and hydrogen molybdenum bronze (HMB) phases, which are crucial for activating CO_2. This is exemplified by Pt-MoO_x synergy, which achieves high MeOH yields under mild conditions. The overarching conclusion is that catalytic

performance is not intrinsic to the metal alone but also is engineered through metal-support interactions, which can be tailored to control the formation of active sites and optimize the reaction pathway for a desired product. However, the exact mechanism of the active sites' formation remains controversial.

1.4 Research gap

The catalytic hydrogenation of CO_2 to MeOH has been extensively investigated as a promising route for sustainable fuel and chemical production. Conventional $Cu/ZnO/Al_2O_3$ systems remain the industrial benchmark; however, their operation at moderate pressures and relatively high temperatures limits MeOH selectivity. Recent studies have highlighted noble metal catalysts, particularly Re- and Ir-based systems, for their superior hydrogen activation at low temperatures and tunable selectivity through metal-support interactions.

Among these, Ir-based catalysts supported on reducible oxides have demonstrated promising activity and selectivity toward MeOH-derived products. In a specific Ir/MoO_3, which exhibited enhanced MeOH-derived product formation compared to other reducible oxides. The specific role of Mo in governing activity and selectivity remains insufficiently understood.

In particular, there is a lack of systematic investigation into:

- The effect of Mo loading on structural evolution, dispersion, and crystallinity of Mo species.
- The influence of Ir-Mo interactions on reducibility and active site formation.
- The correlation between Mo content, surface intermediate formation, and MeOH selectivity under high-pressure conditions.
- The structural and catalytic behavior of Ir-Mo systems under moderate to high-pressure operation (20 - 300 bar), where condensation effects strongly influence reaction pathways.
- Finally, the Ir/MoO_3 system was reported for its high performance in the RWGS reaction. However, there is a clear lack of kinetic investigation of this system under RWGS reaction conditions. Such a study will provide valuable information on the effect of the Ir- Mo interaction under different reaction conditions.

1.5 Scope of this dissertation

This dissertation aimed to understand the unique role of Ir and Mo in boosting the catalytic activity of CO_2 hydrogenation to MeOH, its derived products, and CO, since CO can serve as a crucial intermediate for MeOH. Several techniques were employed to investigate the role of each metal, including *operando* Diffuse Reflectance Infrared Fourier Transform Spectroscopy (DRIFTS) and *in situ* X-ray Absorption Near-Edge Structure (XANES). Understanding the role of these metals will facilitate the design of a rational catalytic system. The dissertation involved four main chapters.

In **Chapter 2**, the Ir was impregnated over different reducible supports to investigate its activity towards MeOH-derived products. The results indicated the high activity of Ir/MoO_3. Further investigation was conducted to understand its unique activity. Furthermore, the reduction temperature was found to have a significant effect on the product selectivity and CO_2 conversion, as explained in sections 1.2.2.3.2 and 1.2.2.3.3. Based on this finding, the reduction temperature protocol was investigated, which eventually led to different results. The findings of this chapter shed light on the potential role of Mo, which was discussed in Chapters 3 and 4.

To further understand and investigate the Mo role, the loading effect was explored to examine the structure-activity relationship. Therefore, in **Chapter 3**, different Mo loadings were impregnated over γ-Al_2O_3, followed by Ir impregnation. The γ-Al_2O_3 support was selected for its high surface area, which allows higher Mo loading. In addition, Mo/γ-Al_2O_3 is a well-established catalyst system for various reactions, including hydrodesulfurization and other hydrotreating reactions, making it highly attractive for investigation in CO_2 hydrogenation. The result indicated that the low Mo loading enhances the catalyst's selectivity towards MeOH-derived products. *Operando* DRIFTS was performed to understand the effect on surface species as Mo loading increased. In this study, the Mo-related species in the low-loading Mo catalyst were well dispersed. As mentioned, this catalyst with a low Mo loading achieved the highest MeOH selectivity. This finding opened the way for further investigation into whether the high MeOH selectivity is due to the low Mo loading or to well-dispersed Mo species.

In **Chapter 4**, the role of Mo dispersion was investigated, since it was identified as a potential parameter for boosting MeOH selectivity in Chapter 3. Similar to the loading effect, the dispersion can also explore the structure-activity relationship and provide mechanistic insight into how the catalyst works if small clusters are present by identifying changes in surface species. Therefore, to further investigate whether this high selectivity toward MeOH in the Ir-Mo-based system is due to a

loading or dispersion effect, two catalysts, Ir/Mo-Al_2O_3 with similar Mo loading but different Mo dispersions, were used. The catalytic activity indicated that the catalyst with higher dispersion showed full selectivity towards MeOH-derived products, with all other side reactions suppressed. The low dispersion catalyst resulted in a dominant CO selectivity. To investigate this effect, the surface species were analyzed by DRIFTS. The results indicated a significant difference in both the surface species environment and Ir particle dispersion. Additionally, the second temperature sequence was performed on the catalyst with high Mo dispersion to investigate its effect. Finally, different reduction protocols were implemented to further investigate their effects on the catalytic activity, as it was found to affect the catalytic activity in the previous chapters.

Ir/MoO_3 was investigated under conditions relevant to MeOH synthesis, where catalytic behavior was shown to be highly sensitive to reaction conditions (Chapter 2). Furthermore, as discussed in Section 1.2.2.3.4, Ir/MoO_3 exhibits high selectivity toward CO under conditions favorable for the RWGS reaction. These variations in catalytic behavior under different operating conditions highlight the tunability of this system. Although **Chapter 5** explores high-temperature conditions beyond the main scope of this thesis, examining catalyst performance under such conditions provides valuable insights into the changes in catalyst structure and behavior. Therefore, in **Chapter 5**, the kinetics of both Ir/MoO_3 and Ir/MoO_3/Al_2O_3 catalysts were evaluated for the RWGS reaction at atmospheric pressure over a range of temperatures (400 - 550 °C). A stability test was also conducted on both systems to assess potential catalyst deactivation under reaction conditions, an essential step for accurate kinetic modeling. The results revealed that the Ir/MoO_3 catalyst exhibited noticeable deactivation, whereas the Ir/MoO_3/Al_2O_3 system remained stable throughout the testing period. Consequently, the kinetic model was developed solely on the basis of the performance of the Ir/Mo/Al_2O_3 catalyst.

References

[1] Institut national d'études démographiques (INED), World population projections by countries, (2024) INED - World Population Prospects.

[2] Laura Cozzi, Alex Martinos, Thomas Spencer, Global Energy Review 2025, (2025) 43. https://iea.blob.core.windows.net/assets/5b169aa1-bc88-4c96-b828-aaa50406ba80/GlobalEnergyReview2025.pdf.

[3] Reuters, Saudi Arabia discovers 14 new oil and gas fields with small volumes, (2025). https://www.reuters.com/business/energy/saudi-arabia-discovers-14-oil-natural-gas-fields-state-news-agency-says-2025-04-09/ (accessed September 17, 2025).

[4] IEA, World Energy Outlook 2023 | Enhanced Reader, World Energy Outlook 2023. (2023) 23-28. https://www.iea.org/news/the-energy-world-is-set-to-change-significantly-by-2030-based-on-today-s-policy-settings-alone.

[5] J. Rigg, The Sustainable Development Goals (SDGS), Companion to Dev. Stud. (2024) 253-257. https://doi.org/10.4324/9780429282348-52.

[6] B. Palmer, Do We Exhale Carbon?, Nat. Resour. Def. Counc. (2015). https://www.nrdc.org/stories/do-we-exhale-carbon.

[7] R. Dębek, Novel catalysts for chemical CO_2 utilization, Paris, 2016. https://tel.archives-ouvertes.fr/tel-01631497.

[8] A. Álvarez, A. Bansode, A. Urakawa, A. V. Bavykina, T.A. Wezendonk, M. Makkee, J. Gascon, F. Kapteijn, Challenges in the Greener Production of Formates/Formic Acid, Methanol, and DME by Heterogeneously Catalyzed CO_2 Hydrogenation Processes, Chem. Rev. 117 (2017) 9804-9838. https://doi.org/10.1021/acs.chemrev.6b00816.

[9] S. GmbH, SYNTHEC Fuels, Methanol, (n.d.) https://www.synthecfuels.com/methanol/.

[10] Swedish knowledge center for renewable and transportation Fuels, Biomass based Dimethyl ether, CH_3OCH_3, 2017.

[11] J. Kurtz, S. Sprik, G. Saur, S. Onorato, Fuel Cell Electric Vehicle Driving and Fueling Behavior Fuel Cell Electric Vehicle Driving and Fueling Behavior, (2019) 1-22.

[12] K. Wipke, S. Sprik, J. Kurtz, T. Ramsden, C. Ainscough, G. Saur, National Fuel Cell Electric Vehicle Learning Demonstration Final Report, Natl. Renew. Energy Lab. / U.S. Dep. Energy. (2012).

[13] D. Heyl, U. Rodemerck, U. Bentrup, Mechanistic Study of Low-Temperature CO_2 Hydrogenation over Modified Rh/Al_2O_3 Catalysts, ACS Catal. 6 (2016) 6275-6284. https://doi.org/10.1021/acscatal.6b01295.

[14] X. Wang, H. Shi, J.H. Kwak, J. Szanyi, Mechanism of CO_2 Hydrogenation on Pd/Al_2O_3 Catalysts: Kinetics and Transient DRIFTS-MS Studies, ACS Catal. 5 (2015) 6337-6349. https://doi.org/10.1021/acscatal.5b01464.

[15] A. Urakawa, Mind the gaps in CO_2 to methanol, Nat. Catal. 4 (2021) 447-448. https://doi.org/10.1038/s41929-021-00638-6.

[16] A. Álvarez, M. Borges, J.J. Corral-Pérez, J.G. Olcina, L. Hu, D. Cornu, R. Huang, D. Stoian, A. Urakawa, CO_2 Activation over Catalytic Surfaces, ChemPhysChem. 18 (2017) 3135-3141. https://doi.org/10.1002/cphc.201700782.

[17] R. Gaikwad, H. Reymond, N. Phongprueksathat, P. Rudolf Von Rohr, A. Urakawa, From CO or CO_2?: Space-resolved insights into high-pressure CO_2 hydrogenation to methanol over $Cu/ZnO/Al_2O_3$, Catal. Sci. Technol. 10 (2020) 2763-2768. https://doi.org/10.1039/d0cy00050g.

[18] X. Su, L. Shen, Advances and challenges about Ni-based dual functional materials for alternating cycles of CO_2 storage and in-situ hydrogenation to CH_4, Carbon Capture Sci. Technol. 13 (2024) 100278. https://doi.org/10.1016/j.ccst.2024.100278.

[19] A. Bansode, A. Urakawa, Towards full one-pass conversion of carbon dioxide to methanol and methanol-derived products, J. Catal. 309 (2014) 66-70. https://doi.org/10.1016/j.jcat.2013.09.005.

[20] N. Phongprueksathat, A. Urakawa, Enhancing Sustainability Through Heterogeneous Catalytic Conversions at High Pressure, in: Heterog. Catal., First Edit, Wiley-VCH, 2021: pp. 633-648. https://doi.org/10.1002/9783527813599.ch35.

[21] E.D. Hanson, L. Lajaunie, S. Hao, B.D. Myers, F. Shi, A.A. Murthy, C. Wolverton, R. Arenal, V.P. Dravid, Systematic Study of Oxygen Vacancy Tunable Transport Properties of Few-Layer MoO_{3-x} Enabled by Vapor-Based Synthesis, Adv. Funct. Mater. (2017) 1-10. https://doi.org/10.1002/adfm.201605380.

[22] N.T. and H.K. Kazunari Takahashi, Mechanism of formation of methyl formate from formaldehyde over copper catalysts, Chem. Lett. 1061-1064 (1983).

[23] G.T. Whiting, S.A. Kondrat, C. Hammond, N. Dimitratos, Q. He, D.J. Morgan, N.F. Dummer, J.K. Bartley, C.J. Kiely, S.H. Taylor, G.J. Hutchings, Methyl Formate Formation from Methanol Oxidation Using Supported Gold − Palladium Nanoparticles, ACS Catal. (2015). https://doi.org/10.1021/cs501728r.

[24] D. Kubas, J.M. Beck, E. Kasisari, T. Schätzler, A. Becherer, A. Fischer, I. Krossing, From CO_2 to DME: Enhancement through Heteropoly Acids from a Catalyst Screening and Stability Study, ACS Omega. 8 (2023) 15203-

15216. https://doi.org/10.1021/acsomega.3c00149.

[25] J.G. Van Bennekom, J.G.M. Winkelman, R.H. Venderbosch, S.D.G.B. Nieland, H.J. Heeres, Modeling and Experimental Studies on Phase and Chemical Equilibria in High-Pressure Methanol Synthesis, Ind. Eng. Chem. Res. (2012).

[26] J.W. Erisman, M.A. Sutton, J. Galloway, Z. Klimont, W. Winiwarter, How a century of ammonia synthesis changed the world, Nat. Geosci. 1 (2008) 636-639. https://doi.org/10.1038/ngeo325.

[27] P. Amann, B. Klötzer, D. Degerman, N. Köpfle, T. Götsch, P. Lömker, C. Rameshan, K. Ploner, D. Bikaljevic, H.Y. Wang, M. Soldemo, M. Shipilin, C.M. Goodwin, J. Gladh, J.H. Stenlid, M. Börner, C. Schlueter, A. Nilsson, The state of zinc in methanol synthesis over a Zn/ZnO/Cu(211) model catalyst, Science (80) 376 (2022) 603-608. https://doi.org/10.1126/science.abj7747.

[28] U.J. Etim, Y. Song, Z. Zhong, Improving the Cu/ZnO-Based Catalysts for Carbon Dioxide Hydrogenation to Methanol, and the Use of Methanol As a Renewable Energy Storage Media, Front. Earth Sci. 8 (2020) 1-26. https://doi.org/10.3389/fenrg.2020.545431.

[29] K.W. Ting, T. Toyao, S.M.A.H. Siddiki, K.I. Shimizu, Low-Temperature Hydrogenation of CO_2 to Methanol over Heterogeneous TiO_2-Supported Re Catalysts, ACS Catal. 9 (2019) 3685-3693. https://doi.org/10.1021/acscatal.8b04821.

[30] T. Toyao, S. Kayamori, Z. Maeno, S.M.A.H. Siddiki, K.I. Shimizu, Heterogeneous Pt and MoO_x Co-Loaded TiO_2 Catalysts for Lowerature CO_2 Hydrogenation to Form CH_3OH, ACS Catal. 9 (2019) 8187-8196. https://doi.org/10.1021/acscatal.9b01225.

[31] R.P. Ye, J. Ding, W. Gong, M.D. Argyle, Q. Zhong, Y. Wang, C.K. Russell, Z. Xu, A.G. Russell, Q. Li, M. Fan, Y.G. Yao, CO_2 hydrogenation to high-value products via heterogeneous catalysis, Nat. Commun. 10 (2019). https://doi.org/10.1038/s41467-019-13638-9.

[32] N. Phongprueksathat, K.W. Ting, S. Mine, Y. Jing, R. Toyoshima, H. Kondoh, K.I. Shimizu, T. Toyao, A. Urakawa, Bifunctionality of Re Supported on TiO_2 in Driving Methanol Formation in Low-Temperature CO_2 Hydrogenation, ACS Catal. 13 (2023) 10734-10750. https://doi.org/10.1021/acscatal.3c01599.

[33] R. Kanega, N. Onishi, S. Tanaka, H. Kishimoto, Y. Himeda, Catalytic Hydrogenation of CO_2 to Methanol Using Multinuclear Iridium Complexes in a Gas-Solid Phase Reaction, J. Am. Chem. Soc. 143 (2021) 1570-1576. https://doi.org/10.1021/jacs.0c11927.

[34] T. Marzialetti, J.L.G. Fierro, P. Reyes, Effect of the nature of the support

on the enantioselective hydrogenation of 1-phenyl-1,2-propanedione over supported iridium catalysts, J. Chil. Chem. Soc. 50 (2005) 391-399. https://doi.org/10.4067/s0717-97072005000100005.

[35] S. Siracusano, V. Baglio, S.A. Grigoriev, L. Merlo, V.N. Fateev, A.S. Aricò, The influence of iridium chemical oxidation state on the performance and durability of oxygen evolution catalysts in PEM electrolysis, J. Power Sources. 366 (2017) 105-114. https://doi.org/10.1016/j.jpowsour.2017.09.020.

[36] S. Li, Y. Xu, Y. Chen, W. Li, L. Lin, M. Li, Y. Deng, X. Wang, B. Ge, C. Yang, S. Yao, J. Xie, Y. Li, X. Liu, D. Ma, Tuning the selectivity of catalytic carbon dioxide hydrogenation over iridium/cerium oxide catalysts with a strong metal-support interaction, Angew. Chemie. 129 (2017) 10901-10905. https://doi.org/10.1002/ange.201705002.

[37] Y. Zhang, Z. Zhang, X. Yang, R. Wang, H. Duan, Z. Shen, L. Li, Y. Su, R. Yang, Y. Zhang, X. Su, Y. Huang, T. Zhang, Tuning selectivity of CO_2 hydrogenation by modulating the strong metal-support interaction over Ir/TiO_2 catalysts, Green Chem. 22 (2020) 6855-6861. https://doi.org/10.1039/d0gc02302g.

[38] C. Shen, K. Sun, Z. Zhang, N. Rui, X. Jia, D. Mei, C.J. Liu, Highly Active Ir/In_2O_3 Catalysts for Selective Hydrogenation of CO_2 to Methanol: Experimental and Theoretical Studies, ACS Catal. 11 (2021) 4036-4046. https://doi.org/10.1021/acscatal.0c05628.

[39] J.A.H. Dreyer, P. Li, L. Zhang, G.K. Beh, R. Zhang, P.H.L. Sit, W.Y. Teoh, Influence of the oxide support reducibility on the CO_2 methanation over Ru-based catalysts, Appl. Catal. B Environ. 219 (2017) 715-726. https://doi.org/10.1016/j.apcatb.2017.08.011.

[40] M. Lopez Luna, J. Timoshenko, D. Kordus, C. Rettenmaier, S.W. Chee, A.S. Hoffman, S.R. Bare, S. Shaikhutdinov, B. Roldan Cuenya, Role of the Oxide Support on the Structural and Chemical Evolution of Fe Catalysts during the Hydrogenation of CO_2, ACS Catal. 11 (2021) 6175-6185. https://doi.org/10.1021/acscatal.1c01549.

[41] X. Li, Z. He, C. Li, D. Kang, J. Chen, Y. Wang, F. Wang, S. Huang, Z. Zhang, Study on the reducible metal oxide carriers to regulate the catalytic reaction performance of CO_2 with ethane, Int. J. Hydrogen Energy. 79 (2024) 45-59. https://doi.org/10.1016/j.ijhydene.2024.06.398.

[42] W. Gac, W. Zawadzki, M. Rotko, M. Greluk, G. Słowik, G. Kolb, Effects of support composition on the performance of nickel catalysts in CO_2 methanation reaction, Catal. Today. 357 (2020) 468-482. https://doi.org/10.1016/j.cattod.2019.07.026.

[43] G. Tian, Y. Wu, S. Wu, S. Huang, J. Gao, CO_2 hydrogenation to methanol over $Pd/MnO/In_2O_3$ catalyst, J. Environ. Chem. Eng. 10 (2022).

https://doi.org/10.1016/j.jece.2021.106965.

[44] M.S. Frei, C. Mondelli, N. López, O. V Safonova, R. García-muelas, K.S. Kley, B. Puértolas, J.A. Stewart, D.C. Ferré, J. Pérez-ramírez, Atomic-scale engineering of indium oxide promotion by palladium for methanol production via CO_2 hydrogenation, Nat. Commun. (2019) 1-11. https://doi.org/10.1038/s41467-019-11349-9.

[45] A. Beck, X. Huang, L. Artiglia, M. Zabilskiy, X. Wang, P. Rzepka, D. Palagin, M.G. Willinger, J.A. van Bokhoven, The dynamics of overlayer formation on catalyst nanoparticles and strong metal-support interaction, Nat. Commun. 11 (2020) 1-8. https://doi.org/10.1038/s41467-020-17070-2.

[46] X. Sun, J. Yu, H. Zada, Y. Han, L. Zhang, H. Chen, W. Yin, J. Sun, Reaction-induced unsaturated Mo oxycarbides afford highly active CO_2 conversion catalysts, Nat. Chem. (2024). https://doi.org/10.1038/s41557-024-01628-4.

[47] Y. Kuwahara, T. Mihogi, K. Hamahara, K. Kusu, H. Kobayashi, H. Yamashita, A quasi-stable molybdenum sub-oxide with abundant oxygen vacancies that promotes CO_2 hydrogenation to methanol, Chem. Sci. 12 (2021) 9902-9915. https://doi.org/10.1039/d1sc02550c.

[48] H. Kim, J.B. Cook, H. Lin, J.S. Ko, S.H. Tolbert, V. Ozolins, B. Dunn, charge storage properties of MoO_{3-x}, Nat. Mater. 16 (2017). https://doi.org/10.1038/NMAT4810.

[49] S.Z. Noby, A. Fakharuddin, S. Schupp, M. Sultan, M. Krumova, M. Drescher, M. Azarkh, K. Boldt, L. Schmidt-Mende, Oxygen vacancies in oxidized and reduced vertically aligned α-MoO_3 nanoblades, Mater. Adv. (2022) 3571-3581. https://doi.org/10.1039/d1ma00678a.

[50] H. Ding, K.G. Ray, V. Ozolins, M. Asta, Structural and vibrational properties of α-MoO_3 from van der Waals corrected density functional theory calculations, Phys. Rev. B - Condens. Matter Mater. Phys. 85 (2012). https://doi.org/10.1103/PhysRevB.85.012104.

[51] S. Adams, CDW Superstructures in Hydrogen Molybdenum Bronzes H_xMoO_3, J. Solid State Chem. 87 (2000) 75-87.

[52] B. Braı, S. Adams, E. Canadell, M. Curie, A. Kristallographie, V. Uni, Concerning the Structure of Hydrogen Molybdenum Bronze Phase III . A Combined Theoretical - Experimental Study, Chem. Mater. (2005) 5957-5969.

[53] K.N. Amba Sankar, L. Kesavan, B. Saha, M.K. Jyolsnaraj, S. Mohan, P. Nandakumar, K. Mohanta, C. Kvarnström, Renewable synthesis of MoO_3 nanosheets via low temperature phase transition for supercapacitor application, Sci. Rep. 14 (2024) 1-20. https://doi.org/10.1038/s41598-024-

69765.

[54] N.A. Chernova, M. Roppolo, C. Dillon, M.S. Whittingham, Layered vanadium and molybdenum oxides : batteries and electrochromics †, J. Mater. Chem. (2009). https://doi.org/10.1039/b819629.

[55] L. Studnicka, L. Krisztina, Hydrothermal Synthesis and Gas Sensing of Monoclinic MoO_3 Nanosheets, Nanomaterials. 10, 891 (2020) 2-13.

[56] P. Wehrer, L. Hilaire, E. Petit, Influence of the reduction conditions of MoO_3 on its isomerizing properties, Appl. Catal. A Gen. 273 (2004) 249-258. https://doi.org/10.1016/j.apcata.2004.06.050.

[57] A. You, M. Be, I. In, High-pressure Raman scattering and x-ray diffraction of phase transitions in, J. Appl. Phys. 023513 (2009). https://doi.org/10.1063/1.3056049.

[58] S. Duwal, M. Kim, S. Kawaguchi, N. Hirao, Y. Ohishi, C. Yoo, Phase Transitions and Resistivity Anomaly of Layered MoO_3 at High Pressure, J. Phys. Chem. (2018). https://doi.org/10.1021/acs.jpcc.8b06434.

[59] K. Kim, C. Kim, S. Bak, C. Nam, J. Hyuk, Amorphous-crystalline transition-driven synthesis of Co single-atom catalysts on MoO_3 for enhanced hydrogen evolution in acidic and alkaline media, Chem. Eng. J. 488 (2024) 150976. https://doi.org/10.1016/j.cej.2024.150976.

[60] Ø.S. Fjellvåg, Ø.S. Fjellvåg, A. Ruud, H.H. Sønsteby, O. Nilsen, H. Fjellvåg, Crystallization, Phase Stability, and Electrochemical Performance of β-MoO_3 Thin Films, Cryst. Growth Des. 20 (2020) 3861-3866. https://doi.org/10.1021/acs.cgd.0c00156.

2 Dynamic surface restructuring of Ir/MoO_x steering CO_2 hydrogenation toward methanol-derived products

Ahmad Alrefaei, Charlotte Jüngen, Shota Matsuo, Atul Bansode, Atsushi Urakawa

The publication is in preparation

Summary

This study investigates iridium (Ir) supported on different reducible oxides for CO_2 hydrogenation to methanol (MeOH). Among them, Ir over molybdenum trioxide (MoO_3) demonstrated outstanding activity toward MeOH-derived products (15 mg/h.g_{cat} at 225 °C and 20 bar). The performance was found to depend strongly on the reduction temperature. A moderate reduction temperature of 200 °C led to partially reduced Mo species (mainly Mo^{4+}), whereas a higher reduction temperature of 400 °C led to more metallic Mo (Mo^0), resulting in a significant increase in MeOH-derived product selectivity. At all tested reduction temperatures, *in situ* X-ray diffraction (XRD) confirmed that the crystalline structure changed to amorphous after reduction. Additionally, *in situ* X-ray Absorption Near Edge Structure (XANES) confirmed that Ir was completely reduced before the 200 °C and that the observed high MeOH-derived products were primarily linked to changes in the Mo chemical state. *Operando* DRIFTS revealed that the reduction temperature alters the surface chemistry, influencing the formation and reactivity of formate species (a key intermediate in MeOH production). Furthermore, repeated reaction cycles led to *in situ* reduction of Mo, as confirmed by *in situ* XANES, which enhanced MeOH formation. Overall, the study demonstrates that the catalytic performance of Ir/MoO_3 is primarily governed by the Mo chemical state. Tuning the Mo chemical state can effectively direct CO_2 hydrogenation toward MeOH-derived products.

2.1 Introduction

The relentless accumulation of anthropogenic carbon dioxide (CO_2) in the atmosphere is a primary driver of global warming, making the control and reduction of CO_2 emissions a pressing global challenge. In this context, the catalytic conversion of CO_2 into value-added chemicals has emerged as a highly appealing, sustainable pathway to simultaneously address environmental concerns and meet growing energy demands [1,2]. Among potential products, methanol (MeOH) is particularly appealing as a versatile fuel and chemical feedstock to the chemical industry [3]. The industrial synthesis of MeOH via CO_2 hydrogenation employs $Cu/ZnO/Al_2O_3$ catalysts at 220-250 °C and 20-100 bar [4–6]. Adding CO to the feed also alters the chemical state of Zn, further enhancing MeOH production [7]. However, thermodynamically, lower temperatures and higher pressures are favored. Theoretical thermodynamic calculations reveal that full CO_2 conversion and MeOH selectivity can be achieved at low temperatures and high pressures, facilitated by the *in situ* separation of condensable products, which shifts the reaction equilibrium toward the forward direction [4,5]. Such low-temperature operation also reduces energy consumption and mitigates catalyst deactivation. Despite these thermodynamic advantages, several catalytic systems have shown that high CH_4 selectivity is often observed below 260 °C, even at high pressure [5,6], underscoring the need for a highly selective catalytic system for MeOH and its derived products.

Iridium (Ir) has shown high activity in the homogeneous hydrogenation of CO_2 to formate, a key intermediate in the production of MeOH [8–10]. Recent studies on the active Ir species in multinuclear catalysts indicate a crucial role for their proximity, which enables hydride transfer that directly reduces CO_2 to formate [10]. High MeOH production in gas-solid reaction under mild conditions (30-80 °C) was observed with no contamination by CO or CH_4 [10]. In heterogeneous systems, Ir's performance is primarily influenced by the support, which stabilizes nanoparticles and dictates product selectivity, resulting in unique product distributions across each catalytic system [11–15]. Therefore, the choice of support material is critical, as it significantly influences catalyst activity and performance [16,17]. Reducible supports, in particular, have demonstrated optimal performance in CO_2 hydrogenation due to their ability to enhance CO_2 activation and facilitate strong metal-support interactions (SMSI) [17–20]. Previous studies on reducible-supported Ir catalysts have primarily focused on high temperatures (up to 300 °C). For instance, the selectivity of Ir supported on ceria (CeO_2) and titania (TiO_2) can be tuned from CH_4 to CO by adjusting the pre-treatment conditions,

highlighting the pronounced influence of the Ir-support interaction, which is strongly dependent on the reduction state [11,15]. In contrast, Ir over indium oxide (In_2O_3) favors a high selectivity towards MeOH [13]. However, the reaction temperature was high, potentially activating other side reactions. Also, an additional role for In_2O_3 is anticipated in directing the reaction pathway towards MeOH via oxygen vacancies [21,22]. Ir over molybdenum trioxide (MoO_3) exhibited exclusive activity in the reverse water gas shift reaction (RWGS) [14]. The variance in these outcomes, often studied under disparate conditions, highlights the need for a unified experimental framework to decouple the effects of support from the role of Ir. Therefore, this work presents a comparative investigation of Ir supported on TiO_2, CeO_2, and MoO_3 under standardized conditions. Among these, Ir/MoO_3 emerged as the most active catalyst, prompting a detailed study of its unique properties and performance in CO_2 hydrogenation to MeOH and its derived products.

2.2 Experimental section

2.2.1 Catalyst synthesis:

The following reagents were used as received. Ir(III)chloride hydrate (CAS No. 10025-83-9) was purchased from Precious Metals Online. Cerium(IV) oxide (CAS No.1306-38-3) was purchased from DAIICHI KIGENSO KAGAKU KOGYO. LTD. Photocatalytic titanium dioxide ST-01 was purchased from Ishihara Sangyo Kaisha, LTD. (ISK), Japan. The MoO_3 (CAS No. 1313-27-5) was purchased from Alfa Aesar. The catalysts were prepared using the wet impregnation (WI) method with an aqueous solution of the respective metal salt, Ir(III) chloride hydrate. 0.071 g of the metal salt (to obtain a metal loading of 1.5 wt% Ir per support) was dissolved in 50 mL of deionized water. The amount of metal salt was calculated based on 3 g of support material. After the salt was completely dissolved in the water (0.5 h), 3 g of the support material was added to the solution. The mixed solution was then stirred at 200 rpm and 50 °C and kept overnight. Subsequently, the drying process was performed in air at 110 °C for 10 h. The obtained powder was crushed and calcined at 500 °C for 3 h, in the air.

2.2.2 Catalysts characterization:

2.2.2.1 H_2-temperature program reduction (H_2-TPR):

200 mg of catalyst was packed inside a quartz tube reactor. H_2 flow was introduced into the reactor, and a heating rate of 10 °C/min was used until reaching a final temperature of 700 °C. The catalysts were heated to 700 °C and held for 10 min. The H_2 signal was recorded online with a thermal conductivity detector (TCD).

2.2.2.2 X-ray diffraction (XRD):

The internal XRD patterns were attained using a Bruker AXS D8 Advance diffractometer. The detector used in the experiment was a Lynxeye-XE-T position-sensitive detector, which enabled efficient and accurate data collection. The recorded data in the range of 5° to 90° was evaluated using the DIFFRAC.EVA software, which provided analysis and interpretation of the diffraction patterns obtained. The diffraction obtained from the XRD at Synchrotron uses a wavelength of 0.53948 Å. Therefore, all the simulated diffraction patterns were obtained using this wavelength.

2.2.2.3 Inductively coupled plasma mass spectrometry (ICP-MS):

The ICP-MS was performed at MIKRO LAB located in Oberhausen, Germany. The exact procedure for the element digestion is considered a company secret. However, the elements Ir, Ce, Mo, Al, and Ti were measured using a Spectro Arcos ICP after microwave digestion on a CEM MARS 6.

2.2.3 Catalytic activity

The catalytic activity was evaluated in a custom-made high-pressure setup, as shown in Figure 2.1. In a typical test, a 125 mg catalyst was loaded into a 1/4-inch reactor tube (ID, 2.79 mm). Before loading, the catalysts were pelletized, crushed, and sieved to obtain particles in the 90-300 µm range. Quartz wool was used to support the catalyst in the reactor. The catalyst was reduced at 200 °C with 90% H_2/Ar (20 mL/min) for 1.5 h under atmospheric pressure. The reduction temperature was changed to 400 ^oC; however, similar duration and reducing agent were utilized. After cooling to 35 °C, the $H_2/CO_2/N_2$ mixture (70.5/23.5/6 vol%) was fed into the reactor and pressurized to 20 bar. The space velocity was maintained at 10 NL/g_{cat} h. The products were analyzed by an online gas chromatograph (Compact GC 4.0m manufactured by Global Analyzer Solutions) equipped with a flame ionization detector for the detection of CH_4, MeOH, methyl formate (MF), dimethyl ether (DME), and ethanol (EtOH), and two thermal conductivity detectors, one for the detection of H_2, N_2, CH_4, and CO. This TCD uses Ar as the mobile phase.

The second TCD was used to detect CO_2, and He is the mobile phase. The carbon balance was monitored to be within 97-102%. The values presented were obtained by averaging the measurements only after steady-state had been reached. A single representative value was then reported for each condition.

$$CO_2 \text{ conversion} = \frac{CO_{2\,in} - CO_{2\,out}}{CO_{2\,in}} \; or \; \frac{\sum n_{C,i} \times \text{Concentration}_i}{CO_{2\,in}}$$

$$\text{Selectivity} = \frac{n_{C,i} \times \text{Concentration}_i}{\sum n_{C,i} \times \text{Concentration}_i}$$

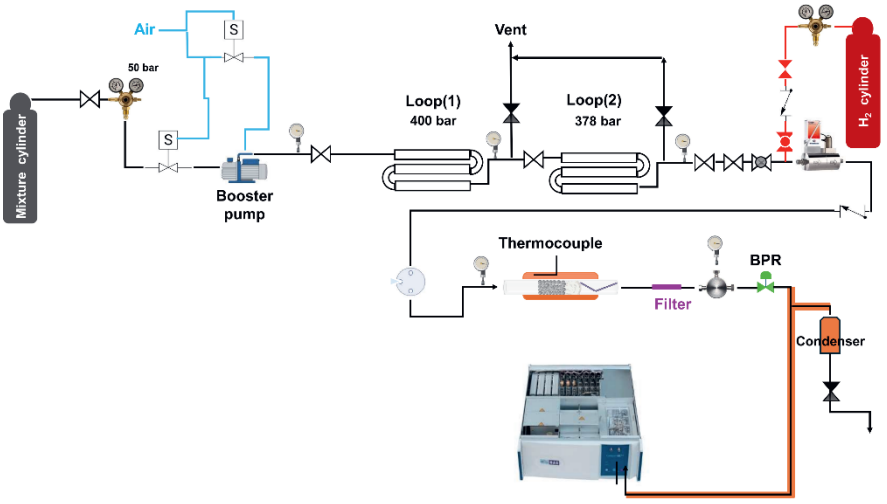


Figure 2.1 Schematic of the reaction setup used for the catalytic activity testing. The reaction mixture was introduced to the booster pump to increase pressure. The system has two loops to store the mixture under high pressure, as shown in loops (1) and (2). A high-pressure mass flow controller is utilized to feed the reactant mixture into the reactor. The system pressure is controlled by the back pressure regulator (BPR). The condenser is used to remove the liquid product. Finally, the product is analyzed in the compact GC shown here.

2.2.4 *Operando* diffuse reflectance infrared fourier transform spectroscopy - mass spectrometry (DRIFTS-MS)

The *operando* DRIFTS was performed utilizing a Thermo Scientific Nicolet 6700 FT-IR connected with a Pfeiffer OmniStar GSD 300C mass spectrometer (MS), as shown in Figure 2.2. The spectrometer is equipped with a liquid-nitrogen-cooled mercury-cadmium-telluride (MCT) detector to

collect the spectra while the MS analyzes the outlet gas stream. Gas flow control in the setup was facilitated by six Bronkhorst mass flow controllers, which regulated the flow rates of H_2, CO_2, and He. Switching between the two reactant gas streams was achieved using a 4-way valve. Back pressure regulators (Bronkhorst) were employed to control the pressure of the reaction cell and the vent side, maintaining the desired pressures within the system. A 40-50 mg of catalyst powder was placed inside a cylindrical cavity, having a diameter of 3 mm and a vertical length of 3 mm, located in a Harrick Praying Mantis DRIFTS accessory. The cell has an inlet on the left side, through the catalyst, and an outlet on the right side. The thermocouple is connected to the cell and located inside the quartz wool below the catalyst to ensure accurate temperature measurement. Before the measurements, the catalyst was reduced at the desired temperature using a mixture of H_2 and He gases (90/10) for 1.5 hours. Subsequently, the sample was cooled to the reaction temperature of 75°C and pressurized to 10 bar under a He stream. The reaction cell was exposed to a CO_2:H_2 feed with a 1:3 ratio (total flow rate of 15 mL/min). The spectra were acquired at a resolution of 4 cm^{-1}. 10 spectra were averaged and collected after 13.3 s.

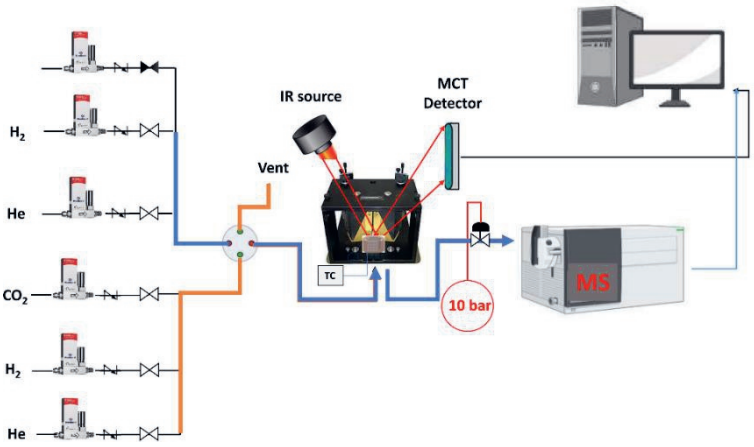


Figure 2.2 Schematic of the DRIFTS setup used for the DRIFTS experiment. The reaction mixture was introduced after pressurizing the reaction cell to the desired pressure using He via the blue line, while the reaction mixture is shown in orange. The reaction mixture was analyzed using MS.

2.2.5 Synchrotron experiments

The experiments were performed at the ALBA BL16-NOTOS beamline. Prior to the experiment, the catalyst was diluted in boron nitrate (BN) at a 1:10 ratio. Then, A 10 cm-long capillary with an inner diameter of 1 mm and a wall thickness of 10 μm was used to load the diluted catalyst. The central 0.5 cm of the capillary was loaded with the diluted catalyst sample. To facilitate gas heating, the sample was fixed with 1 cm of silicon carbide (SiC) at the outlet and 2 cm at the inlet. Quartz wool was used at both ends to fixate the bed. The capillary was mounted in a U-shaped cell that allowed either direct gas flow through the capillary or in bypass mode. Subsequently, the bed was heated with a hot blower, of which the position was calibrated to the middle of the bed, with roughly 5 cm spacing in between the blower and the bed to ensure the blower and catalyst temperature are linearly related up to 600 ^{o}C. XANES spectra were taken sequentially at the Ir L_3-edge (11215 eV) and Mo K-edge (20000 eV). Spectral acquisition times were approximately 3 minutes for XANES and 2 minutes for Synchrotron X-ray Diffraction (XRD) measurements. Both edges were measured in fluorescence mode using a 13-element Si detector. In the first experiment, an Ir/MoO_3 catalyst was reduced *in situ* under a 5 mL/min H_2 flow with a ramp rate of 10 ^{o}C/min, after which the temperature remained constant at the desired temperature for 90 minutes. This was followed by a ramp down to 40 ^{o}C to obtain a high-resolution XAS spectrum of the reduced state of Ir and Mo. After collecting these spectra, the reaction mixture was switched to a 1:3 CO_2:H_2 mixture (10 mL/min), and the capillary was pressurized to 20 bar. Then, the temperature was increased to 75, 225, and 75 ^{o}C. XANES spectra were collected during the temperature ramping, and X-ray diffractions were collected after each step.

2.3.1 The catalytic activity of CO_2 hydrogenation

The catalytic performance of Ir supported on various metal oxides (CeO_2, TiO_2, and MoO_3) was evaluated for CO_2 hydrogenation at 150, 175, 200, and 225 °C under 20 bar. The reduction protocol for these catalysts is as follows: heating to 200 °C using H_2/Ar (90/10) feed for 90 min. After reduction, the reactor was cooled to 35 °C, then pressurized to 20 bar with feed H_2/CO_2 = 3. The MeOH production rates as a function of reaction temperature for the three tested catalysts are shown in Figure 2.3. At 150 and 175 °C, MeOH was observed only over Ir/MoO_3. When the reaction temperature increased further to 200 and 225 °C, MeOH was observed over all three catalysts, i.e., Ir/TiO_2, Ir/CeO_2, and Ir/MoO_3. Although MoO_3, as a support, has a similar reducible

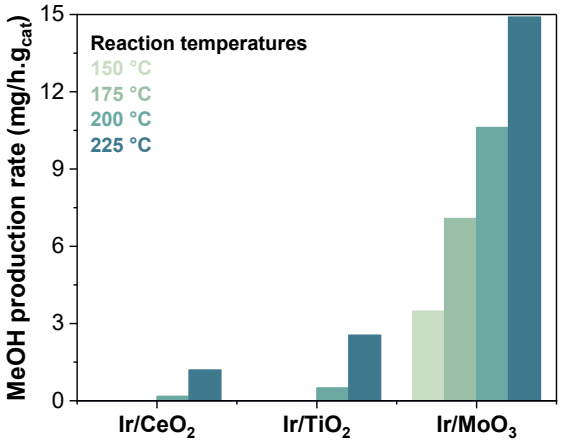


Figure 2.3 The Methanol (MeOH) production rate in mg/h.g_{cat} during the CO_2 hydrogenation of the following catalysts: Ir/CeO_2, Ir/TiO_2, and Ir/MoO_3, evaluated at 150, 175, 200, and 225 °C, and at 20 bar, and H_2/CO_2 = 3. The results show the remarkable activity of Ir/MoO_3 towards high MeOH production among other catalysts at all reported temperatures, indicating the catalyst's high performance

nature to TiO_2 and CeO_2, the Ir/MoO_3 exhibits a remarkably five times higher production rate of MeOH as compared to Ir/CeO_2 and Ir/TiO_2. This substantial difference in MeOH production rate indicates that Mo plays a crucial role in directing the reaction toward MeOH. Furthermore, Toyao *et al.* investigated the Mo effect in the Pt/MoO_3 system, which was found to boost activity towards high MeOH conversion, suggesting a synergistic effect between Pt and Mo [23]. Notably, this effect is also expected to be observed between Ir and Mo, resulting in this high activity towards MeOH. However, over Ir/TiO_2 and Ir/CeO_2, Ir is expected to be highly covered by the support species, as reported previously by Zhang over Ir/TiO_2 [24]. This phenomenon is expected to reduce the number of Ir active sites, resulting in catalyst inactivity at low temperatures.

In addition, the MeOH production rate in Ir/MoO_3 increases with increasing reaction temperature, as shown in Figure 2.3, but the MeOH selectivity decreases, as shown in the Figure 2.3-S (Appendix). The significant increase in MeOH production rate with increasing reaction temperature is primarily attributed to the enhanced CO_2 conversion.

The catalytic activity performance of Ir/MoO_3 was also investigated at 300 bar, and the results are shown in Figure 2.6-S (Appendix). The Ir/MoO_3 shows no significant difference in product distribution. The absence of a significant difference in product distribution between Ir/MoO_3 at 20 and 300 bar demonstrates that the catalyst operates along the same pathway at both pressures, providing a clear advantage for this system. However, the conversion increased with pressure, reaching in some cases almost 3 times higher (at 200 °C using the R200 protocol, from 4% at 20 bar to 11.5% at 300 bar). This was expected, since increasing the pressure will result in higher gas-phase concentration and surface coverage, which most likely leads to higher conversion. Hence, the outstanding activity of Ir/MoO_3, distinct from other reducible oxides, combined with its kinetic advantage, underscores its unique nature and motivates a comprehensive investigation to elucidate the origin of its high performance.

2.3.2 Effect of reduction temperature on CO_2 conversion and MeOH selectivity over Ir/MoO_3

The catalytic performance of Ir/MoO_3 was found to be critically dependent on the reduction temperature [25]. The reduction protocol was initially set at 200 °C for 90 min (R200) based on the H_2-TPR data (Figures 2.11-S and 2.12-S, Appendix). A different reduction temperature, 400 °C (R400), was also examined to investigate the effect of reduction temperature on catalytic performance and the productivity of MeOH-derived products across different reaction temperatures, as shown in Figure 2.4. Increasing the reduction temperature to 400 °C significantly increases the rate of production of MeOH-derived products. The higher reduction temperature steers the formation of a specific, highly reduced Mo species that boosts MeOH formation [25]. Therefore, the reduction temperature critically governs the catalytic performance of Ir/MoO_3: higher temperatures promote selective MeOH production likely via the formation of a specific reduced Mo species.

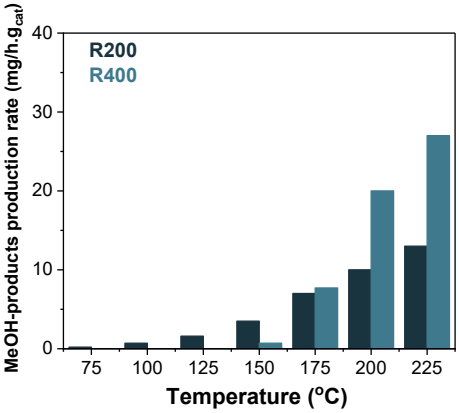


Figure 2.4 The MeOH-derived product (MeOH, methylformate, and dimethyl ether) production rate in mg/h.g_{cat} during the CO_2 hydrogenation of Ir/MoO_3 evaluated after applying the two reduction protocols, R200 and R400. The production rate was obtained at different reaction temperatures, at 20 bar, and H_2/CO_2 = 3. The results indicate a significant increase in the production rate of MeOH-derived products when the R400 reduction protocol is applied compared with the R200 reduction protocol.

2.3.3 Effect of reduction temperature on the chemical state of Ir/MoO_3

To elucidate the origin of the changes in catalytic activity with reduction temperature, the chemical states of Ir and Mo were investigated during and after the reduction. *In situ* XANES was performed during H_2-TPR to monitor the evolution of the chemical states of Ir and Mo at each reduction temperature. Two experiments were conducted; in each, fresh Ir/MoO_3 was reduced with hydrogen under conditions similar to those used for the pre-treatment during catalytic activity testing. Two reduction temperatures were tested: 200 °C (R200) and 400 °C (R400). The Ir L_3-edge and Mo K-edge were measured during the reduction, and both are shown in Figure 2.5 at all reduction temperatures. The Ir L_3-edge shown in Figure 2.5 (a) shows a significant change in the Ir chemical state between the fresh catalyst and the reduced one, evidenced by the substantial change in the white line intensity. However, between R200 and R400, no discernible difference was observed, suggesting that Ir is entirely reduced to its metallic state by 200 °C. Consequently, the differences in catalytic performance between the R200 and R400 reduction protocols are unlikely to be due to changes in the chemical state of Ir. For the Mo K-edge, the analysis of the fresh catalyst shown in Figure 2.5 (b) reveals that its spectrum is comparable to that of the pristine

MoO_3 support. The identical spectral shape and edge energy confirm that the Mo retains a +6 oxidation state and a similar local structure. This indicates that Ir impregnation does not significantly impact the chemical state or structure of the MoO_3 support. In contrast, the Mo K-edge of the catalyst at R200 and R400 showed a pronounced change between the two conditions. Through the linear combination fitting (LCF), R200 revealed a Mo^{4+} content of ~77%, as observed by the MoO_2 fitting (Figure 2.5 (c)), alongside other possible oxidation states. The analysis of the progressive change in the Mo K-edge during temperature ramping, as shown in Figure 2.13-S (Appendix), indicates a significant change in the pre-edge feature at ~170 °C, suggesting a potential change in the Mo coordination environment at this temperature. Increasing the reduction temperature to 400 °C (R400) resulted in a more deeply reduced catalyst, as evidenced by decreases in Mo^{4+} and increases in Mo^0, as shown in Figure 2.5 (d). Similar to the R200, the progressive change in Mo K-edge during the temperature ramping of the R400 occurred at exactly the same temperature, ~170 °C. In summary, Ir was found to be fully reduced at 200 °C, and the possible decisive factor in the change in catalytic performance is the redox state of MoO_3. A deeper reduction to more reduced Mo species at 400 °C shifts the selectivity toward MeOH-derived products.

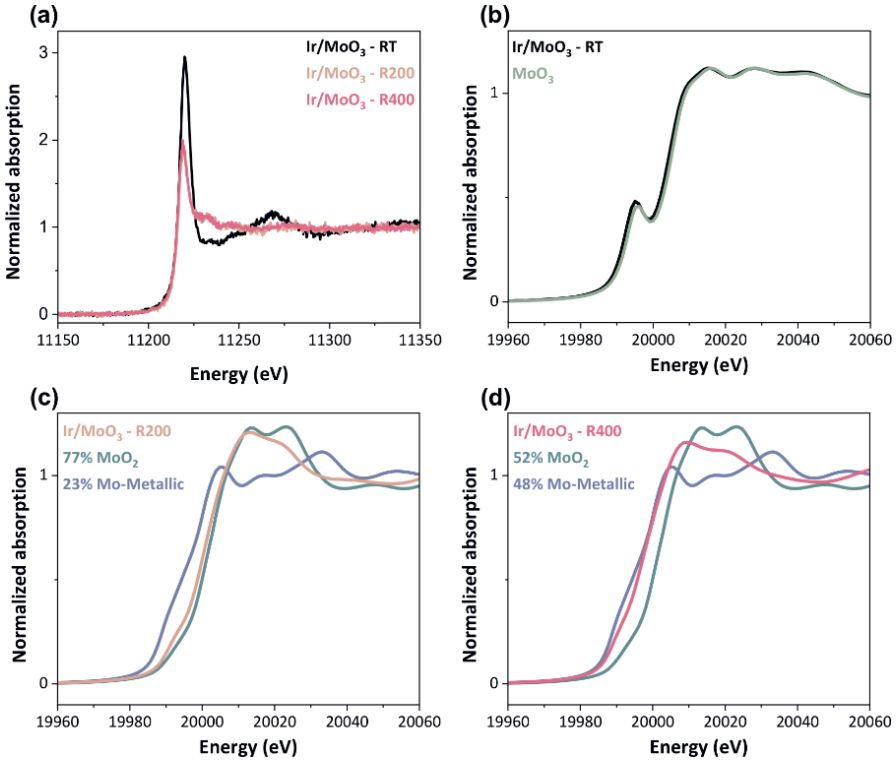


Figure 2.5 *In situ* XANES spectra collected during H_2 reduction of the Ir/MoO_3 catalyst at 200 °C (R200) and 400 °C (R400). **(a)** Ir L_3-edge, which indicates no change in the chemical state of Ir between R200 and R400. The Mo K-edge for Ir/MoO_3 **(b)** at room temperature (RT), fresh catalyst **(c)** after R200 protocol, linear combination fitting (LCF) analysis reveals the catalyst is composed of 77% MoO_2 and 23% Mo^0 **(d)** after R400 protocol, LCF analysis reveals the catalyst is composed of 52% MoO_2 and 48% metallic Mo. This result strongly suggests that the alteration in the catalytic performance is due to the change in the Mo chemical state

2.3.4 Effect of reduction temperature on the structural evolution of Ir/MoO_3

To further corroborate the shift in the Mo chemical state observed in the *in situ* XANES, *in situ* XRD was performed on the support MoO_3, the fresh state of the catalyst Ir/MoO_3 at room temperature (RT), and R200 and R400 reduced catalysts. (Figure 2.6). The XRD graph of MoO_3 indicates a fully crystalline structure comprising orthorhombic (α-MoO_3) phases [26–29]. Quantitative analysis revealed that the predominant phase is the α-MoO_3 phase with a crystallite size estimated at ~51 nm. The hexagonal (h-MoO_3) phase is expected, but due to peak overlapping, it is challenging to detect. The MoO_3 can form multiple distinct crystal structures (polymorphs), and the geometry of the MoO_6 octahedra is different in each. The coexistence of these two polymorphs is frequently observed in MoO_3 samples synthesized via low-temperature routes, such as precipitation or hydrothermal methods [30,31]. The metastable hexagonal phase is kinetically favored under these conditions and can persist alongside the stable orthorhombic phase. The presence of both phases in the support suggests a synthesis pathway that allowed the partial formation of h-MoO_3, with incomplete thermal conversion to the α-phase.

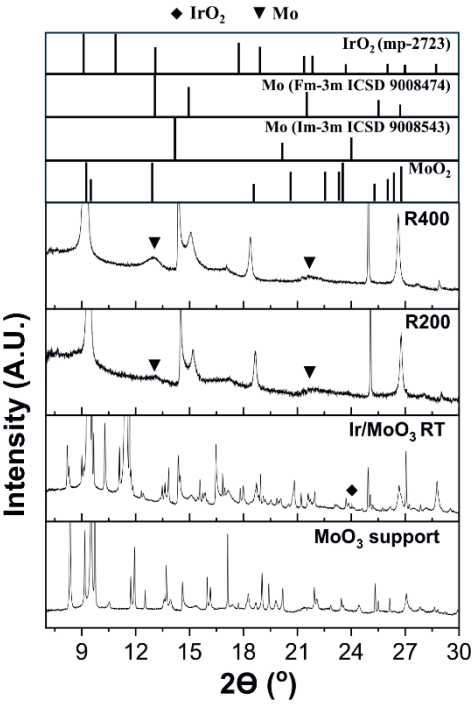


Figure 2.6 X-ray diffraction (XRD) of the MoO_3 support and the as-synthesized Ir/MoO_3 catalyst. At room temperature (RT), after reduction at 200 °C for 90 min (R200), and after reduction at 400 °C for 90 min (R400). Other references (computed Mo metallic, MoO_2, and computed IrO_2) are shown above the diffractions. The result illustrates no significant alteration of the MoO_3 support upon deposition of Ir. Additionally, after reduction using the two reduction protocols, R200 and R400, a complete transformation of the structure from fully crystalline to amorphous was observed. All unidentified diffractions in R200 and R400 correspond to Boron nitrate (BN). Check Figure 2.9-S for more details. Mo metallic FCC and BCC (simulated diffraction developed using Mercury).

Following Ir impregnation, the diffraction pattern shows no significant change; only a small reflection corresponding to IrO_2 was detected at 22.1° (Figure 2.6), confirming the formation of a small Ir oxide crystallite phase. To further assess the influence of Ir doping, the XRD patterns of MoO_3 and Ir/MoO_3 (RT) were compared. The analysis of the unit cell parameters indicates a small expansion in the a-lattice parameter (from 0.392 nm to 0.396 nm), while the c-parameter exhibits a slight decrease. This change in the a- and c-axes leads to an overall cell volume increase that occurs predominantly along the a-axis [32]. The minor increase in cell volume and the absence of change in diffraction are consistent with the *in situ* XANES data shown in Figure 2.5 (b), which indicate identical spectral shapes and edge energies for the MoO_3 support and Ir/MoO_3. Thus, the XRD analysis corroborates the XANES results, confirming that the MoO_3 support's structure remains largely intact after Ir incorporation. The absence of the HMB phase suggests that higher reduction temperatures and the higher heating rate used during the experiment lead to its dehydration [25]. It is highly expected that this extent of reduction is due to Ir, which underscores Ir's high activity in dissociating H_2, as confirmed by the high hydrogen consumption in H_2-TPR results shown in Figures 2.11-S and 2.12-S (Appendix) [25,33]. To investigate the reason behind the catalyst amorphization after reduction, *in situ* DRIFTS was employed during the reduction step. Loss of terminal oxygen (Mo=O) was observed in real time during the reduction process, as shown in Figure **2.**2.7-S (Supporting information). This loss was identified by the distinct negative peak developed in the 950 - 1000 cm^{-1} region at a temperature of ~177 °C. This spectral region is characteristic of the stretching vibration of Mo=O bonds [34]. The terminal oxygen (Mo=O) bonds, oriented perpendicular to the van der Waals (vdW) gap, and are essential for maintaining structural integrity between bilayers, as illustrated in the green plane in Figure **2.**2.8-S (Supporting information). Their loss is expected to trigger a collapse of the crystallite framework, ultimately resulting in the disappearance of long-range order. Additionally, at this temperature, the pre-edge feature of the Mo K-edge experiences a change, as shown in the *in situ* XANES result (Figure 2.13-S, Supporting information). The depletion of the Mo=O terminal oxygen and the alteration of the pre-edge feature in the Mo white line provide strong evidence that the observed amorphization arises from the disruption or removal of Mo=O bonds, thereby destabilizing the crystalline framework. To further investigate the amorphous structure after applying the R200, the XRD pattern was analyzed. Two broad reflections centered at 13.5° and 21.8° (Figure 2.4) are observed, attributed to the formation of metallic Mo and consistent with the reference patterns [35–38]. According to the XANES results obtained

under the R200 protocol, the fraction of MoO_2 is higher than that of metallic Mo. However, it is highly expected that the MoO_2 phase is amorphous, making its detection in the XRD challenging. In the sample reduced at R400, diffraction peaks appear at identical positions (13.5° and 21.8°) and exhibit significantly higher intensities, indicating a higher Mo-metallic content. This result agrees with the XAS analysis, which indicates a higher Mo-metallic content when R400 is applied. Thus, the progressive reduction of the Ir/MoO_3, transitioning from a crystalline to a disordered amorphous phase due to the loss of the Mo=O terminal oxygen, containing a lower Mo-metallic content at R200, and finally to a higher Mo-metallic content at R400.

Following reduction using R200 protocols, the crystalline structure of both IrO_2 and MoO_3 disappeared, yielding an amorphous material featuring two broad peaks at approximately 13° and 21.8°. While previous studies have proposed the formation of a hydrogen molybdenum bronze (HMB) phase during reduction at low temperature [39–41]No diffraction evidence for this phase was confirmed in the present case for either R200 or R400 Figure 2.10-S (Appendix).

2.3.5 Summary of the effect of reduction protocol on Mo chemical state, amorphization, and selectivity toward MeOH-derived products

The catalytic performance of the reduced Ir/MoO_3 catalyst is profoundly influenced by two main factors: the average chemical state of Mo and the amorphization of the catalyst after each reduction temperature. Applying the R200 led to the formation of less reduced Mo species (average Mo^0 of 23%) compared with the R400, where the average Mo^0 is 48%, as measured by in situ XANES (Figure 2.5 (d)). In addition, the structure of the R200 sample after reduction becomes amorphous, with less intense peaks related to Mo^0 (Figure 2.6). However, applying the R400 protocol also led to an amorphous structure, with higher Mo^0 peak intensities. These two findings suggest that the existence of a higher content of Mo-reduced species results in the higher formation of MeOH-derived products, as observed in the catalytic activity testing (Figure 2.4). Therefore, the harsher reduction condition maximizes catalytic activity toward MeOH-derived products, consistent with previous reports on MoO_3 systems [25,42,43].

Additionally, the difference in the average Mo chemical state observed between R200 and R400 (Figure 2.5) influences the catalyst surface chemistry [44–46], thereby leading to changes in the adsorption of surface species under relevant operating conditions. O*perando* DRIFTS

measurements were performed under a CO_2/H_2 feed at 75 °C and 10 bar, after the catalyst was independently pretreated using the R200 and R400 protocols. The results of the C-O vibration region (1100-1800 cm^{-1}) for both experiments (R200 and R400) are shown in Figure 2.7. Two peaks attributed to bicarbonate (HCO_3^-) at 1431 cm^{-1} and 1646 cm^{-1} were observed for R200 with a difference between the symmetrical and asymmetrical vibration (Δv) of 215 cm^{-1}. However, for R400, this difference in the vibrational modes of HCO_3^- resulted in a Δv of 222 cm^{-1}. This change in Δv suggests a different bonding environment for the surface species, R200 and R400 [47]. This change in surface chemistry accounts for the observed difference in activity toward MeOH-derived products.

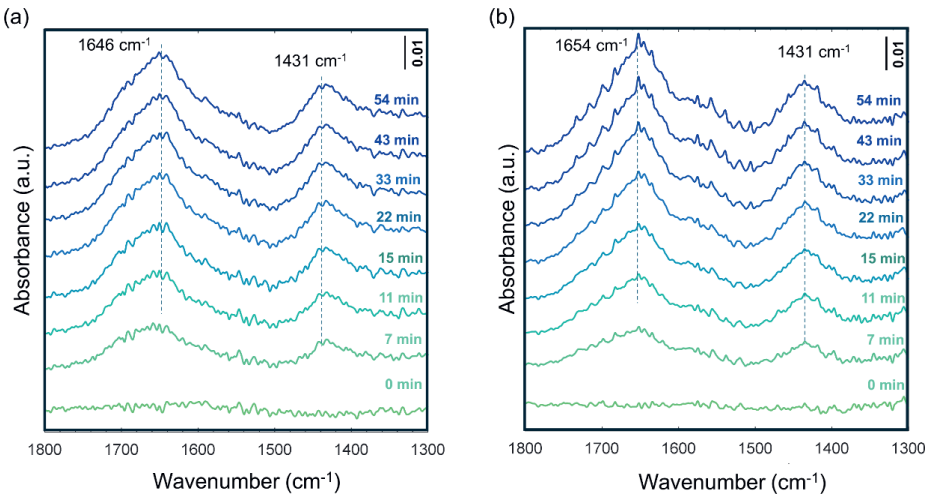


Figure 2.7 *Operando* DRIFTS spectra of the Ir/MoO_3 catalyst under CO_2/H_2 (10 bar, 75 °C) in the C-O stretching region (1300-1800 cm^{-1}). **(a)** The result when the catalyst is reduced using the R200 reduction protocol shows bands at 1646 and 1431 cm^{-1}, characteristic of bicarbonate species. **(b)** For the R400 reduction protocol, the shifted bands at 1654 and 1431 cm^{-1} indicate the formation of bicarbonate species with a different coordination environment, revealing that the change in reduction temperature results in a change in surface chemistry, leading to a different CO_2 adsorption geometry.

2.3.6 The effect of two consecutive temperature sequences on the catalytic performance of Ir/MoO_3

During catalytic testing at 20 bar, a standard experimental procedure was followed in which the reaction temperature was sequentially increased from 75 °C to 200 °C (named as First temperature sequence), as described in the Experimental Section. To ensure reproducibility, the procedure included cooling the reaction back to 100 °C and comparing the catalytic performance at 100 °C during the initial temperature sequence with that obtained after cooling. A significant change in MeOH selectivity was observed between the first and second measurements (named as Second temperature sequence) at 100 °C, as shown in Figure 2.3-S (Appendix), indicating a potential change in the catalyst state between the two conditions. To investigate this and to confirm the change in the catalyst state, the catalyst was tested at 20 bar using the R200 reduction protocol and a temperature sequence from 75 to 225 °C, as shown in Figure 2.8. The R200 was selected because of the high CO_2 conversion observed with this reduction protocol. After the first sequence, the catalyst was subjected to a second identical temperature sequence. The first sequence exhibited unstable behavior, characterized by varying selectivity for CO and CH_4. In contrast, the second sequence exhibited high MeOH selectivity at lower temperatures, which decreased as the reaction temperature increased, while methanation became dominant. The CO_2 conversion decreased from 8% in the first sequence to almost 5% in the second sequence at the highest operating temperature. This marked decrease indicates that a clear catalyst deactivation occurred during exposure to elevated reaction temperatures. Such pronounced deactivation is likely due to Ir sintering. To elucidate the origin of this change, *operando* XANES was performed. After a reduction in H_2 at 200 °C, a CO_2/H_2 feed was introduced at 75 °C, then heated to 225 °C, and finally cooled back to 75 °C. Both Ir L_3-edge and Mo K-edge were monitored during the reaction. The Ir L_3-edge showed no change, indicating that the Ir chemical state remained metallic throughout, as shown in Figure 2.21-S. However, the Mo K-edge experienced a slight shift toward a more reduced state, as shown in Figure 2.20-S. Linear combination fitting (LCF) analysis of the Mo K-edge revealed that the Mo^{4+} content decreased from ~80% (first temperature sequence) to ~72% (second temperature sequence), as shown in Figure 2.17-S (Appendix). This indicates that under the reaction condition (CO_2/H_2), the catalyst undergoes *in situ* reduction, leading to more reduced Mo species. Interestingly, the presence of more reduced Mo species is also believed to

modify the surface chemistry, consistent with previous observations during the reduction temperature study, and appears to favor MeOH formation.

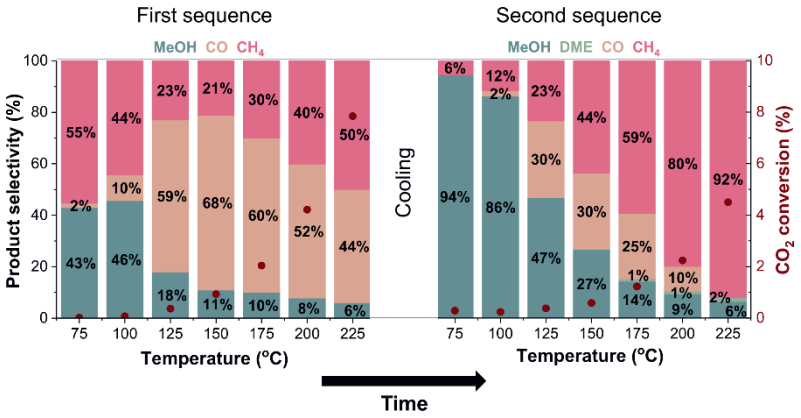


Figure 2.8 Catalytic performance of the Ir/MoO_3 catalyst reduced at 200 °C (R200) in CO_2 hydrogenation, evaluated at 20 bar, H_2/CO_2 = 3, different reaction temperatures, and two temperature sequences named as First sequence and Second sequence. The catalyst exhibits low CO_2 conversion at 75-125 °C, ranging from 0.2-0.5%. Increasing the reaction temperature significantly increased conversion. Also, a notable shift in the second sequence is observed, as indicated by the high MeOH selectivity and low CO_2 conversion at low temperatures (75-125 °C), which differs from the first sequence.

To confirm this change in surface chemistry, *operando* DRIFTS was performed using the same experimental procedure applied during the *operando* XANES. At the first 75 °C, bands at 1649 and 1431 cm^{-1} were observed and assigned to a bicarbonate species, as shown in Figure 2.9 (a) [48,49]. Upon heating to 225 °C, these bands shifted to 1590 and 1381 cm^{-1}. Upon cooling to the second 75 °C, this shift persisted. This significant shift in the wavenumber indicates a change in the environment of the adsorbed species, confirming the modification of surface chemistry. Three hypotheses were considered to explain this modification: (1) the same bicarbonate species experiencing a weakened bonding environment due to higher electron donation from the more reduced Mo species, shifting the wavenumber to a lower value, (2) the formation of a new species, or (3) the hydrogenation of bicarbonate to a new species, most likely formate. The shift in the wavenumber exceeds 60 cm^{-1}, making it unrealistic to consider the first hypothesis. Therefore, analysis of the C-H region (2500-3100 cm^{-1}) was performed, and the result revealed the emergence of a broad peak at ~ 2880 cm^{-1} during the second 75 °C step, which is characteristic of the C-H stretching of a formate species, as shown in Figure 2.9 (b) [45,50,51]. Therefore, the new bands at 1590 and 1381 cm^{-1} are conclusively assigned to formate, indicating a fundamental change in the reaction mechanism

favoring MeOH production [52–54]. Moreover, the difference between the symmetrical and asymmetrical vibration of formate ($\Delta\nu$) is 209 cm^{-1}, suggesting the formation of a bidentate type [55]. However, formate species can originate from the hydrogenation of bicarbonate over Mo or from other sources. To confirm this point, multivariate curve resolution-alternative least squares (MCR-ALS) was performed on the collected spectra. The result shown in Figure 2.9 (c) indicates that at the start of the reaction, when the temperature is 75 °C, the bicarbonate species increase, while no formate is observed. Upon heating the reaction to 225 °C, the formate signal increases in line with the bicarbonate signal. After cooling down the reaction to 75 °C, the formate signal increases while the bicarbonate signal decreases. This finding strongly suggests that the increase in the formate signal is primarily due to the consumption of bicarbonate. The corresponding wavenumbers for each species are shown in Figure 2.17-S (b). In summary, the catalyst undergoes an *in-situ* reduction under reaction conditions, resulting in more reduced Mo species and modifying the surface chemistry. This transformation facilitates the hydrogenation of bicarbonate to formate, a key intermediate in MeOH production. Consequently, the reaction pathway shifts to favor MeOH production, explaining the change in selectivity between the first and second temperature sequences.

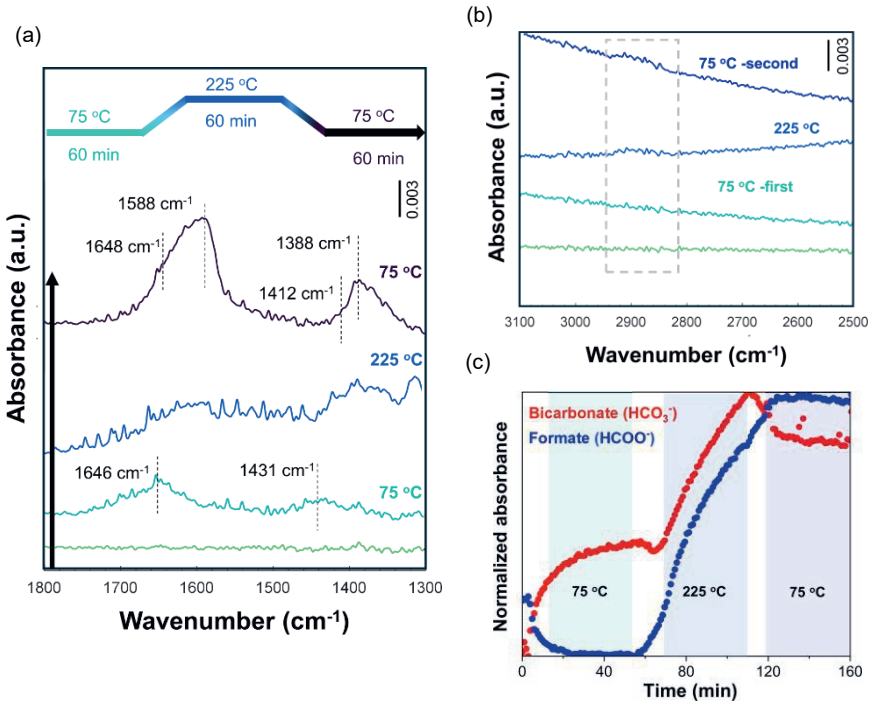


Figure 2.9 The DRIFTS result of the Ir/MoO_3 system (R200) evaluated at 10 bar and temperatures of 75, 225, followed by cooling to 75 °C **(a)** The C-O stretching region (1100-1800 cm^{-1}) shows the shift in the wavenumber when the reaction temperature reaches 225 °C, indicating the evolution of the formate species from bicarbonate and **(b)** the C-H region (2500-3100 cm^{-1}), confirming the appearance of a new stretching at 2900 cm^{-1} corresponding to C-H vibration of formate species when the reaction temperature reaches 225 °C. **(c)** The multivariate curve resolution-alternative least squares (MCR-ALS) method, applied to the *operando* DRIFTS data (collected at 10 bar and temperatures of 75 °C, 225 °C, and subsequent cooling to 75 °C), confirms the evolution of formate species by showing the distinct temporal evolution behaviors of each species.

2.4 Conclusion

Ir-supported on a series of reducible metal oxides revealed that the interaction of Ir with the support dictates the rate of formation of MeOH-derived product. Ir/MoO_3 exhibited remarkably high activity, an order of magnitude greater than that of other supported catalysts, which motivated a comprehensive investigation into the origin of its exceptional performance. The subsequent investigation demonstrated that the catalytic performance is dynamically controlled by the chemical and structural state of the MoO_x support, which can be precisely tuned via the reduction protocol. A moderate reduction at 200 °C generates fewer reduced Mo species, resulting in a low

MeOH-derived product production rate. In contrast, reduction at 400 °C drives the Mo species toward a more reduced state, which modifies the surface chemistry to enhance selectivity toward MeOH-derived products. The key discovery of this work is that by performing an identical second temperature sequence, the catalyst undergoes *in situ* reduction, leading to more reduced Mo species. This reduced Mo species alters the reaction mechanism by forming a formate intermediate at the expense of the bicarbonate species, resulting in a higher MeOH selectivity in the second temperature sequence.

References

[1] L. Cozzi, A. Martinos, T. Spencer, Global Energy Review (2025) 43.

[2] International Energy Agency, World Energy Outlook (2023).

[3] S. Roy, A. Cherevotan, S.C. Peter, Thermochemical CO_2 Hydrogenation to Single Carbon Products: Scientific and Technological Challenges, ACS Energy Lett. 3 (2018) 1938–1966.

[4] R. Gaikwad, H. Reymond, N. Phongprueksathat, P. Rudolf Von Rohr, A. Urakawa, From CO or CO_2?: Space-resolved insights into high-pressure CO_2 hydrogenation to methanol over $Cu/ZnO/Al_2O_3$, Catal. Sci. Technol. 10 (2020) 2763–2768.

[5] N. Phongprueksathat, K.W. Ting, S. Mine, Y. Jing, R. Toyoshima, H. Kondoh, K.I. Shimizu, T. Toyao, A. Urakawa, Bifunctionality of Re Supported on TiO_2 in Driving Methanol Formation in Low-Temperature CO_2 Hydrogenation, ACS Catal. 13 (2023) 10734–10750.

[6] A. Álvarez, A. Bansode, A. Urakawa, A. V. Bavykina, T.A. Wezendonk, M. Makkee, J. Gascon, F. Kapteijn, Challenges in the Greener Production of Formates/Formic Acid, Methanol, and DME by Heterogeneously Catalyzed CO_2 Hydrogenation Processes, Chem. Rev. 117 (2017) 9804–9838.

[7] P. Amann, B. Klötzer, D. Degerman, N. Köpfle, T. Götsch, P. Lömker, C. Rameshan, K. Ploner, D. Bikaljevic, H.Y. Wang, M. Soldemo, M. Shipilin, C.M. Goodwin, J. Gladh, J.H. Stenlid, M. Börner, C. Schlueter, A. Nilsson, The state of zinc in methanol synthesis over a Zn/ZnO/Cu(211) model catalyst, Science (1979). 376 (2022) 603–608.

[8] S.V.C. Vummaleti, G. Talarico, S.P. Nolan, L. Cavallo, A. Poater, How easy is CO_2 fixation by M-C bond containing complexes (M = Cu, Ni, Co, Rh, Ir)?, Organic Chemistry Frontiers 3 (2016) 19–23.

[9] H.K. Lo, I. Thiel, C. Copéret, Efficient CO_2 Hydrogenation to Formate with Immobilized Ir-Catalysts Based on Mesoporous Silica Beads, Chemistry - A European Journal 25 (2019) 9443–9446.

[10] R. Kanega, N. Onishi, S. Tanaka, H. Kishimoto, Y. Himeda, Catalytic Hydrogenation of CO_2 to Methanol Using Multinuclear Iridium Complexes in a Gas-Solid Phase Reaction, J. Am. Chem. Soc. 143 (2021) 1570–1576.

[11] S. Li, Y. Xu, Y. Chen, W. Li, L. Lin, M. Li, Y. Deng, X. Wang, B. Ge, C. Yang, S. Yao, J. Xie, Y. Li, X. Liu, D. Ma, Tuning the Selectivity of Catalytic

Carbon Dioxide Hydrogenation over Iridium/Cerium Oxide Catalysts with a Strong Metal-Support Interaction, Angew. Chem. Int. Ed. 129 (2017) 10901–10905.

[12] J.J. Corral-Pérez, A. Billings, D. Stoian, A. Urakawa, Continuous Hydrogenation of Carbon Dioxide to Formic Acid and Methyl Formate by a Molecular Iridium Complex Stably Heterogenized on a Covalent Triazine Framework, ChemCatChem 11 (2019) 4725–4730.

[13] C. Shen, K. Sun, Z. Zhang, N. Rui, X. Jia, D. Mei, C.J. Liu, Highly Active Ir/In_2O_3 Catalysts for Selective Hydrogenation of CO_2 to Methanol: Experimental and Theoretical Studies, ACS Catal. 11 (2021) 4036–4046.

[14] X. Sun, J. Yu, H. Zada, Y. Han, L. Zhang, H. Chen, W. Yin, J. Sun, Reaction-induced unsaturated Mo oxycarbides afford highly active CO_2 conversion catalysts, Nat. Chem. (2024).

[15] Y. Zhang, Z. Zhang, X. Yang, R. Wang, H. Duan, Z. Shen, L. Li, Y. Su, R. Yang, Y. Zhang, X. Su, Y. Huang, T. Zhang, Tuning selectivity of CO_2 hydrogenation by modulating the strong metal-support interaction over Ir/TiO_2 catalysts, Green Chemistry 22 (2020) 6855–6861.

[16] W. Gac, W. Zawadzki, M. Rotko, M. Greluk, G. Słowik, G. Kolb, Effects of support composition on the performance of nickel catalysts in CO_2 methanation reaction, Catal. Today 357 (2020) 468–482.

[17] L. Shen, J. Xu, M. Zhu, Y.F. Han, Essential role of the support for nickel-based CO_2 methanation catalysts, ACS Catal. 10 (2020) 14581–14591.

[18] A. Beck, X. Huang, L. Artiglia, M. Zabilskiy, X. Wang, P. Rzepka, D. Palagin, M.G. Willinger, J.A. van Bokhoven, The dynamics of overlayer formation on catalyst nanoparticles and strong metal-support interaction, Nat. Commun. 11 (2020) 1–8.

[19] X. Li, Z. He, C. Li, D. Kang, J. Chen, Y. Wang, F. Wang, S. Huang, Z. Zhang, Study on the reducible metal oxide carriers to regulate the catalytic reaction performance of CO_2 with ethane, Int. J. Hydrogen Energy 79 (2024) 45–59.

[20] S.J. Tauster, S.C. Fung, R.L. Garten, Strong Metal-Support Interactions. Group 8 Noble Metals Supported on TiO_2, Journal of the American Chemical Society (1978).

[21] H.S. Mahdi, A. Parveen, M.M. Ali, A. Azam, Microstructural and optical properties of indium oxide nanoparticles, Mater. Today Proc. 18 (2019) 704–709.

[22] T.P. Araújo, J. Morales-Vidal, G. Giannakakis, C. Mondelli, H. Eliasson, R. Erni, J.A. Stewart, S. Mitchell, N. López, J. Pérez-Ramírez, Reaction-Induced Metal-Metal Oxide Interactions in Pd-In_2O_3/ZrO_2 Catalysts Drive Selective and Stable CO_2 Hydrogenation to Methanol, Angew. Chem. Int. Ed. 62 (2023).

[23] T. Toyao, S. Kayamori, Z. Maeno, S.M.A.H. Siddiki, K.I. Shimizu, Heterogeneous Pt and MoO_x Co-Loaded TiO_2 Catalysts for Lower-temperature CO_2 Hydrogenation to Form CH_3OH, ACS Catal. 9 (2019) 8187–8196.

[24] Y. Zhang, Z. Zhang, X. Yang, R. Wang, H. Duan, Z. Shen, L. Li, Y. Su, R. Yang, Y. Zhang, X. Su, Y. Huang, T. Zhang, Tuning selectivity of CO_2 hydrogenation by modulating the strong metal-support interaction over Ir/TiO_2 catalysts, Green Chemistry 22 (2020) 6855–6861.

[25] Y. Kuwahara, T. Mihogi, K. Hamahara, K. Kusu, H. Kobayashi, H. Yamashita, A quasi-stable molybdenum sub-oxide with abundant oxygen vacancies that promotes CO_2 hydrogenation to methanol, Chem. Sci. 12 (2021) 9902–9915.

[26] N.A. Chernova, M. Roppolo, C. Dillon, M.S. Whittingham, Layered vanadium and molybdenum oxides : batteries and electrochromics †, J. Mater. Chem. (2009).

[27] L. Studnicka, L. Krisztina, Hydrothermal Synthesis and Gas Sensing of Monoclinic MoO_3 Nanosheets, Nanomaterials 10, 891 (2020) 2–13.

[28] K. Kim, C. Kim, S. Bak, C. Nam, J. Hyuk, Amorphous-crystalline transition-driven synthesis of Co single-atom catalysts on MoO 3 for enhanced hydrogen evolution in acidic and alkaline media, Chemical Engineering Journal 488 (2024) 150976.

[29] H. Ding, K.G. Ray, V. Ozolins, M. Asta, Structural and vibrational properties of α-MoO_3 from van der Waals corrected density functional theory calculations, Phys. Rev. B Condens. Matter Mater. Phys. 85 (2012).

[30] G.S. Medeiros Leão, M.D. Silva Ribeiro, R.L. de F. Filho, L.B. Saraiva, R.R. Peña-Garcia, A.P. de C. Teixeira, R.M. Lago, F.A. Freitas, S. de Sá Barros, S.D. Junior, Y.L. Ruiz, F.X. Nobre, The Synergic Effect of h-MoO_3, α-MoO_3, and β-MoO_3 Phase Mixture as a Solid Catalyst to Obtain Methyl Oleate, ACS Appl. Mater. Interfaces 16 (2024) 60103–60121.

[31] W. Qian, Y. Wang, L. Liu, Y. Yang, G. Zhang, S. Huang, J. Yi, Heterophase hexagonal/orthorhombic molybdenum trioxide nanorods for photocatalytic hydrogen production, Int. J. Hydrogen Energy 89 (2024) 656–663.

[32] X. Zhang, Y. Xu, D. Li, Y. Zhang, The effect of metal ions doping on the electrochemical performance of molybdenum trioxide, Electrochim. Acta (2018).

[33] T. Ressler, J. Wienold, R.E. Jentoft, Formation of bronzes during temperature-programmed reduction of MoO with hydrogen-an in situ XRD and XAFS study, Solid State Ionics 141–142 (2001) 243–251.

[34] S. Adams, CDW Superstructures in Hydrogen Molybdenum Bronzes H_xMoO_3, J. Solid State Chem. 87 (2000) 75–87.

[35] B. Braı, S. Adams, E. Canadell, M. Curie, A. Kristallographie, V. Uni, Concerning the Structure of Hydrogen Molybdenum Bronze Phase III. A Combined Theoretical - Experimental Study, Chemical Materials (2005) 5957–5969.

[36] J. Wang, W. Li, C. Yu, Y. Chen, Y. Zhang, of Mo species in Pt/MoO_3 and $PtMo/Al_2O_3$ Catalysis (1997).

[37] F.C. Nart, S. Kelling, C.M. Friend, Oxygen Lability on Thin Oxide Films on Mo(110), Journal of Physical Chemistry B 104 (2000) 3212–3218.

[38] K.N. Amba Sankar, L. Kesavan, B. Saha, M.K. Jyolsnaraj, S. Mohan, P. Nandakumar, K. Mohanta, C. Kvarnström, Renewable synthesis of MoO_3 nanosheets via low temperature phase transition for supercapacitor application, Sci. Rep. 14 (2024) 1–20.

[39] P. Wehrer, L. Hilaire, E. Petit, Influence of the reduction conditions of MoO_3 on its isomerizing properties, Appl. Catal. A Gen. 273 (2004) 249–258.

[40] Ø.S. Fjellvåg, Ø.S. Fjellvåg, A. Ruud, H.H. Sønsteby, O. Nilsen, H. Fjellvåg, Crystallization, Phase Stability, and Electrochemical Performance of β-MoO_3 Thin Films, Cryst. Growth Des. 20 (2020) 3861–3866.

[41] H. Kim, J.B. Cook, H. Lin, J.S. Ko, S.H. Tolbert, V. Ozolins, B. Dunn, charge storage properties of MoO_{3-x}, Nat. Mater. 16 (2017).

[42] S. Sun, P. Gao, Y. Shen, T. Wu, Q. An, Enhanced Water Dissociation Promotes Photocatalytic CO_2 Hydrogenation to Methane: A Case Study of Pt-Loaded MoO_3 Catalyst, ACS Sustain. Chem. Eng. 12 (2024) 14760–14770.

[43] J.S. Chung, R. Miranda, C.O. Bennett, Mechanism of partial oxidation of methanol over MoO_3, J. Catal. 114 (1988) 398–410.

[44] D. Lorito, A. Paredes-Nunez, C. Mirodatos, Y. Schuurman, F.C. Meunier, Determination of formate decomposition rates and relation to product formation during CO hydrogenation over supported cobalt, Catal. Today 259 (2016) 192–196.

[45] N. Ishito, K. Hara, K. Nakajima, A. Fukuoka, Selective synthesis of carbon monoxide via formates in reverse water – gas shift reaction over alumina-supported gold catalyst, Journal of Energy Chemistry 25 (2016) 306–310.

[46] N. Schumacher, K.J. Andersson, J. Nerlov, I. Chorkendorff, Surface Science Formate stability and carbonate hydrogenation on strained Cu overlayers, Surf. Sci. 602 (2008) 2783–2788.

[47] J. Kim, B.B. Sarma, E. Andrés, N. Pfänder, P. Concepción, G. Prieto, Surface Lewis Acidity of Periphery Oxide Species as a General Kinetic Descriptor for CO_2 Hydrogenation to Methanol on Supported Copper Nanoparticles, ACS Catal. 9 (2019) 10409–10417.

[48] S. Sun, P. Gao, Y. Shen, T. Wu, Q. An, Enhanced Water Dissociation Promotes Photocatalytic CO_2 Hydrogenation to Methane: A Case Study of Pt-Loaded MoO_3 Catalyst, ACS Sustain. Chem. Eng. 12 (2024) 14760–14770.

[49] J.S. Chung, R. Miranda, C.O. Bennett, Mechanism of partial oxidation of methanol over MoO_3, J. Catal. 114 (1988) 398–410.

[50] D. Lorito, A. Paredes-Nunez, C. Mirodatos, Y. Schuurman, F.C. Meunier, Determination of formate decomposition rates and relation to product formation during CO hydrogenation over supported cobalt, Catal. Today 259 (2016) 192–196.

[51] N. Schumacher, K.J. Andersson, J. Nerlov, I. Chorkendorff, Surface Science Formate stability and carbonate hydrogenation on strained Cu overlayers, Surf. Sci. 602 (2008).

[52] F. Jin, X. Yang, J. Yang, Y. Lei, W. Xu, W. Jiang, Z. Ma, G. Liang, H. Ben, X. Li, Unraveling the influence of oxygen vacancies in MoO_x catalysts on CO_2 hydrogenation, Chemical Engineering Journal 495 (2024) 153333.

[53] D. Heyl, U. Rodemerck, U. Bentrup, Mechanistic Study of Low-Temperature CO_2 Hydrogenation over Modified Rh/Al_2O_3 Catalysts, ACS Catal. 6 (2016) 6275–6284.

[54] G. Busca, V. Lorenzelly, Infrared spectroscopic identification of species arising from reactive adsorption of carbon oxides on metal oxide surfaces, Materials Chemistry 89–126 (1982).

[55] I. Wachs, M. Banares Springer Handbook of Advanced Catalyst Characterization, (2023).

Appendix

Chapter 2

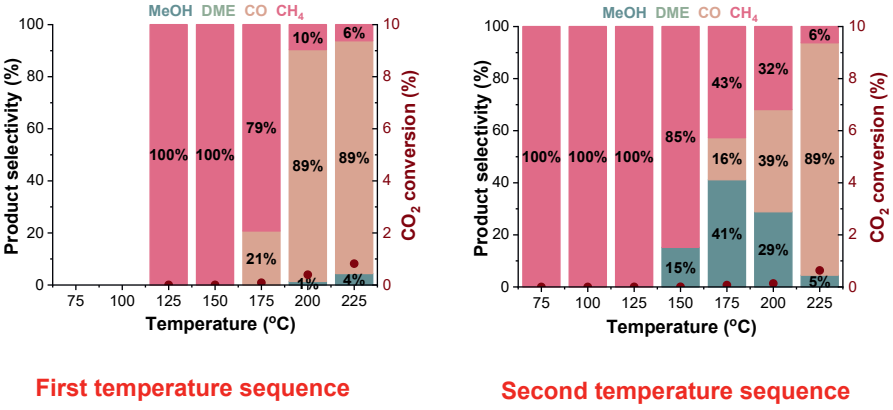


Figure 2.1-S Catalytic activity performance of Ir/CeO_2 at 20 bar, H_2/CO_2 = 3, using R200 reduction protocol and at different reaction temperatures. The result indicates no activity for this catalytic system at low temperature in the first temperature sequence and very low activity toward the methanation reaction in the second temperature sequence. As the reaction temperature increases, the RWGS reaction becomes dominant.

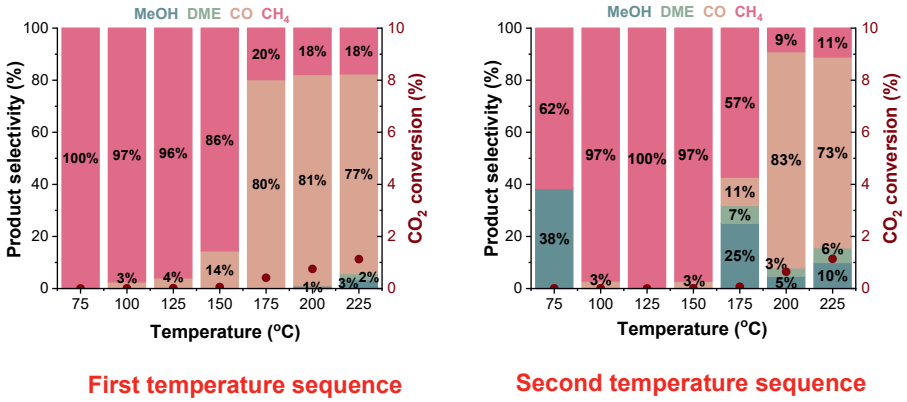


Figure 2.2-S Catalytic activity performance of Ir/TiO_2 at 20 bar, H_2/CO_2 = 3, using R200 reduction protocol and at different reaction temperatures. The result indicates activity toward the methanation reaction at low reaction temperature, which is shifted towards the RWGS reaction as the reaction temperature increases. No significant difference was observed in the second temperature sequence.

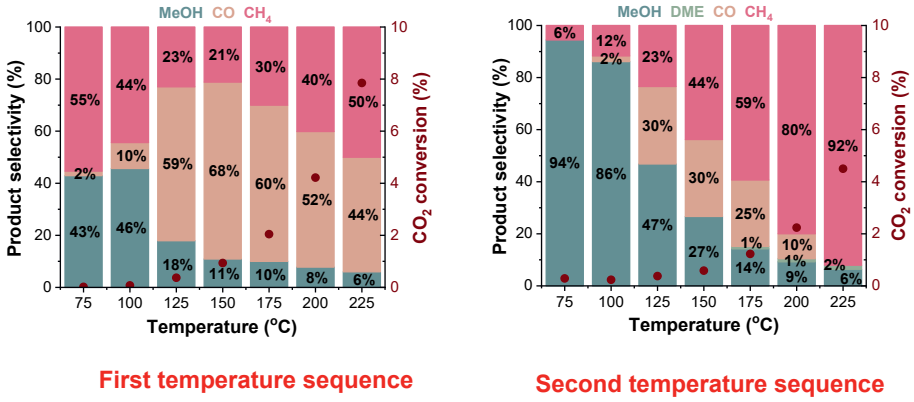


Figure 2.3-S Catalytic activity performance of Ir/MoO_3 at 20 bar, H_2/CO_2 = 3, using R200 reduction protocol and at different reaction temperatures. The result indicates high activity of the catalyst in both temperature sequences. In the first sequence, MeOH was observed at low temperatures. As the reaction temperature increases, the selectivity of CO and CH_4 becomes dominant. In the second temperature sequence, the catalyst shows high activity toward MeOH at low temperatures with almost full selectivity towards MeOH. As the reaction temperature increases, the methanation becomes dominant.

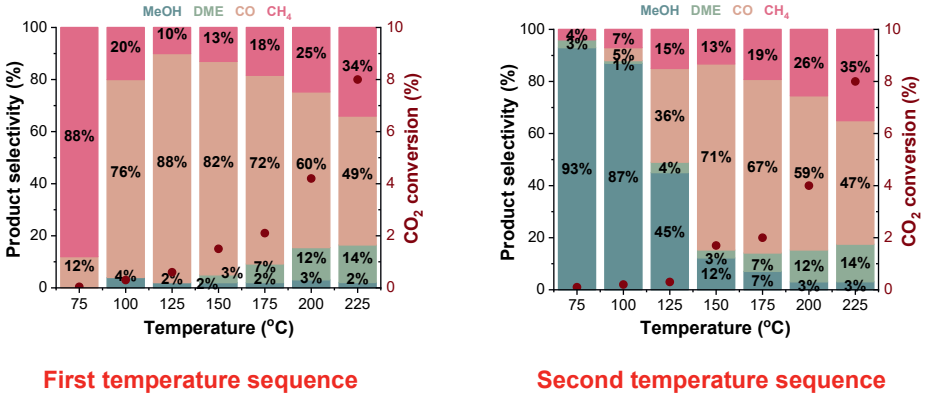


Figure 2.4-S Catalytic activity performance of Ir/MoO_3 at 20 bar, H_2/CO_2 = 3, using R300 reduction protocol and at different reaction temperatures. The result in the first temperature sequence indicates high activity towards the RWGS reaction, which was observed to be dominant at all reaction temperatures, except at 75 °C, where methanation was observed. In the second temperature sequence, the catalysts show high activity towards MeOH at low temperatures, as observed when R200 was applied. As the reaction temperature increased, the RWGS reaction was dominant and the performance became similar to the first temperature sequence.

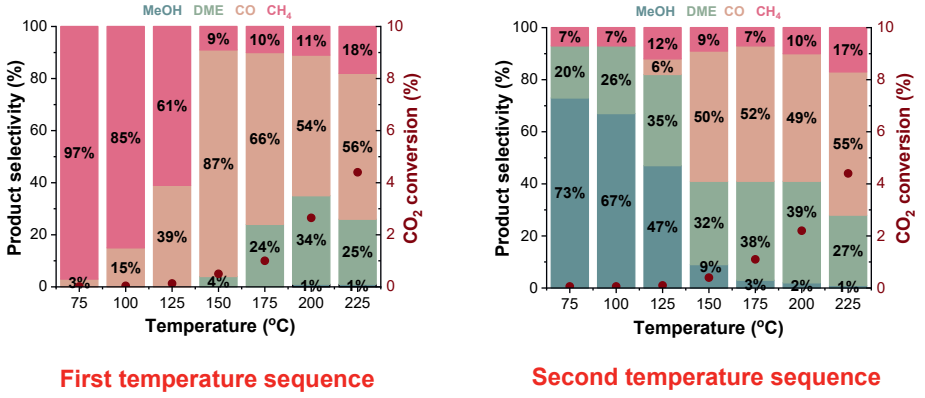


Figure 2.5-S Catalytic activity performance of Ir/MoO_3 at 20 bar, H_2/CO_2 = 3, using R400 reduction protocol and at different reaction temperatures. The result in the first temperature sequence indicates high methanation activity at low temperatures, as the reaction temperature increases, the catalyst performance shifted towards forming CO and DME. In the second temperature sequence, the catalysts shows high activity towards MeOH. As the reaction temperature increases, similar performance to the first temperature sequence is observed.

Table 2.1-S The ICP-MS results obtained for all tested catalysts (MIKROLAB, 14/03/2023)

Catalyst	Ir (%)	Ce (%)	Mo (%)	Ti (%)
Ir/CeO_2	1.4	77.4		
Ir/TiO_2	1			59.2
Ir/MoO_3	1.2		65.4	

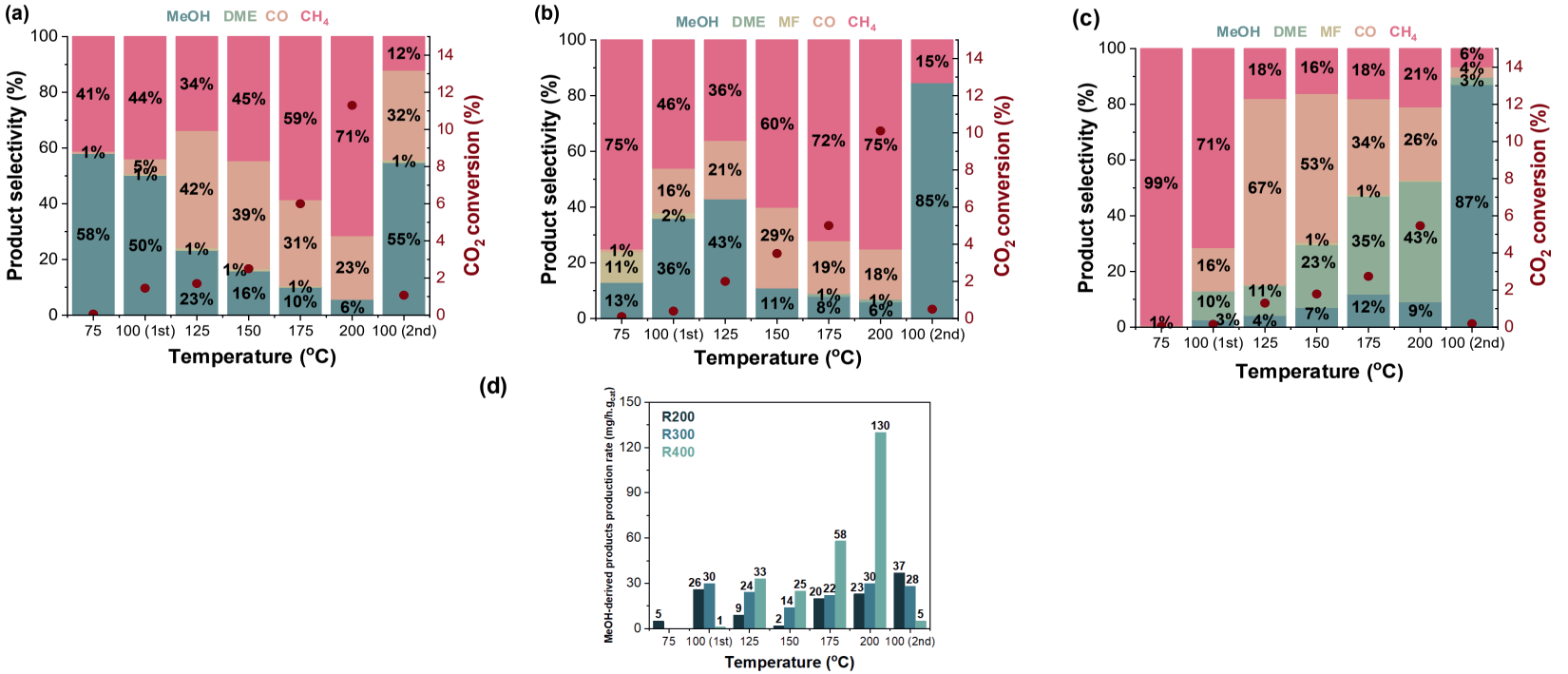


Figure 2.6-S Catalytic activity performance of Ir/MoO_3 at 300 bar, H_2/CO_2 = 3, using different reduction protocols and at different reaction temperatures. **(a)** The catalytic activity using the R200 protocol shows a similar product distribution to the activity performed at 20 bar. **(b)** The R300 protocol shows an increase in MeOH selectivity when the reaction increases until 125 °C. As the reaction temperature increases further, the methanation becomes dominant. **(c)** The catalytic activity performance when R400 is applied indicates a dominant methanation reaction. As the reaction temperature increases, the DME was observed to be dominant. **(d)** The MeOH-derived product production rate at different temperatures using the three reduction protocols, R200, R300, and R400. The result indicates the superior activity towards high MeOH-derived product production rate when R400 is applied.

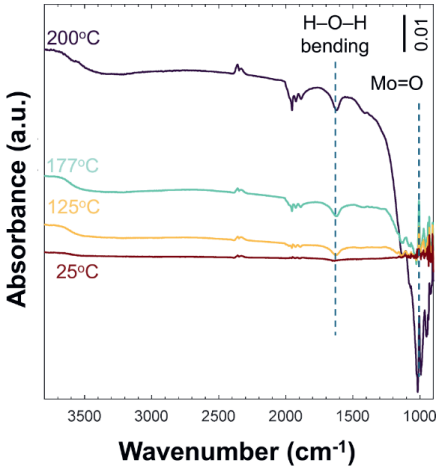


Figure 2.7-S Operando DRIFTS experiment performed over Ir/MoO_3 when the temperature ramping started during the reduction protocol R200. The result shows no change in the spectra until reaching 177 °C, where a negative peak appeared between 900 - 1000 cm^{-1}, which is a characteristic region for the vibration of Mo=O terminal oxygen. This result indicates the depletion of this bond or structure when the reduction temperature reached 177 °C. The H-O-H bonding (scissoring) indicates the removal of water due to the reaction of hydrogen with terminal oxygen, confirming that this negative peak appears between 900 - 1000 cm^{-1}, corresponding to the loss of the Mo=O bond.

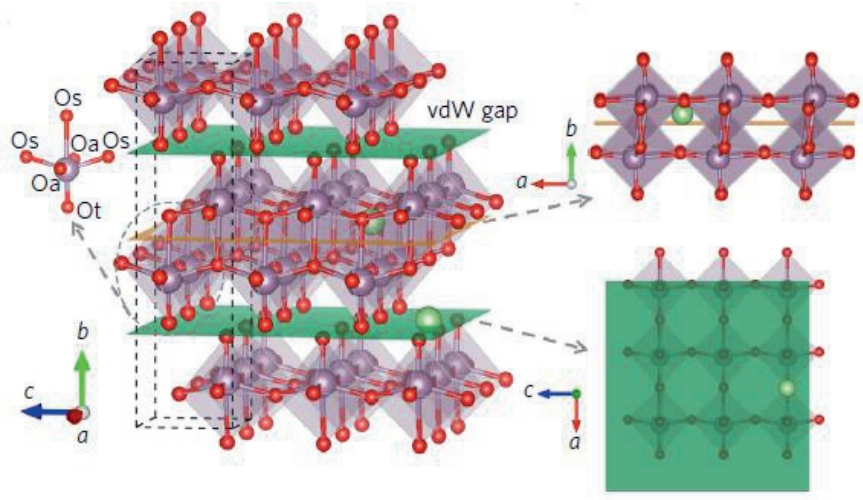


Figure 2.8-S Crystal structure of MoO_3. The structural framework consists of a layer network of edge-sharing MoO_6 octahedra (shown in grey). The layer are stacked along the b direction and bonded to adjacent layers by van der Waals (vdW) forces. The 'terminal oxygen' (O_t) results in a Mo-O_t bond that points perpendicular to the vdW gap (shown in green), which is believed to be the one responsible for ensuring the structural integrity [1]

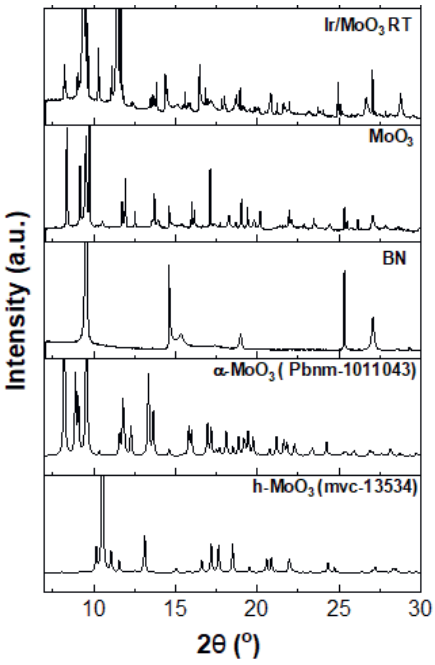


Figure 2.9-S XRD result of computed hexagonal MoO_3 phase (h-MoO_3), computed orthorhombic MoO_3 phase (α-MoO_3), Boron nitride (BN), MoO_3 support used for the catalysts preparation, and the as-prepared catalyst, Ir/MoO_3 (RT), under room temperature conditions. The result shows the dominance of the α-MoO_3 before and after Ir impregnation

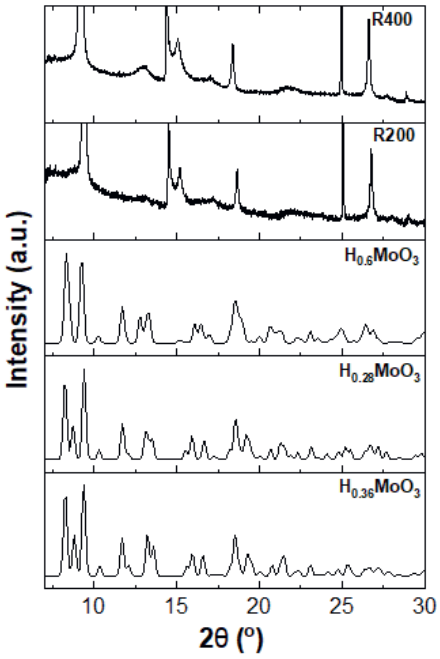


Figure 2.10-S XRD for the computed hydrogen molybdenum bronze (HMB), different phases with the XRD of the reduced Ir/MoO_3 at R200 and R400, which indicate the absence of those phases in the catalyst after reduction

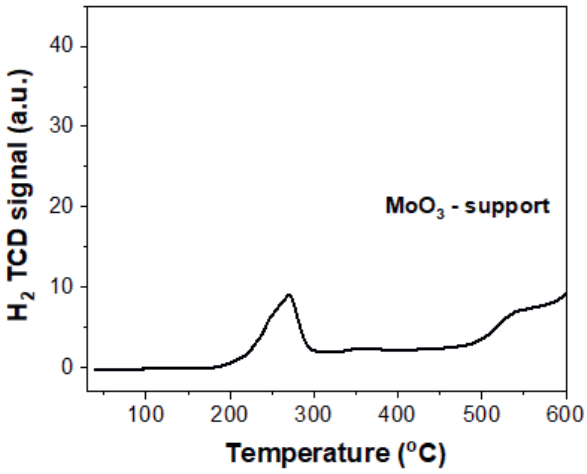


Figure 2.11-S The H_2-TPR profile of MoO_3, which indicates the existence of two peaks. One at 250 °C, and the second one starts at 500 and continues to appear at high temperatures.

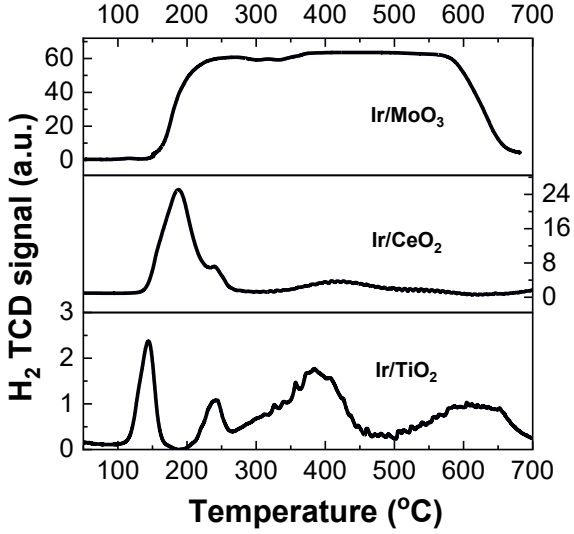


Figure 2.12-S The H_2-TPR profile of Ir/MoO_3, Ir/CeO_2 and Ir/TiO_2. The result shows the remarkable hydrogen consumption of Ir/MoO_3 in comparison with other catalysts

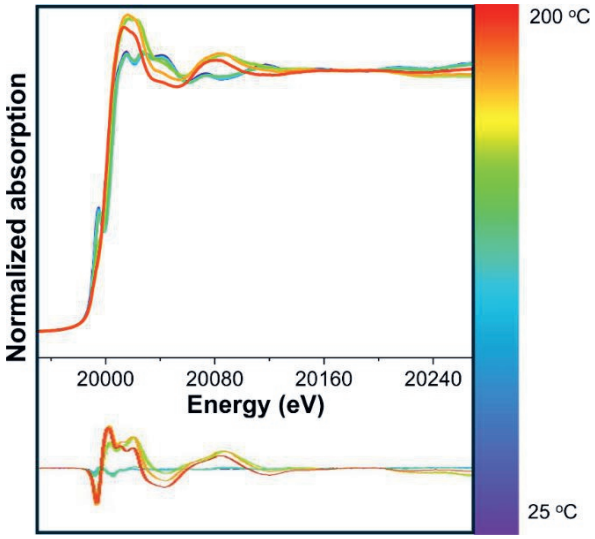


Figure 2.13-S In situ XANES results obtained during the reduction of the Ir/MoO_3 system showing the progressive change in Mo K-edge. The reduction protocol used is the R200. The result indicates that the pre-edge feature started to disappear at 170 °C

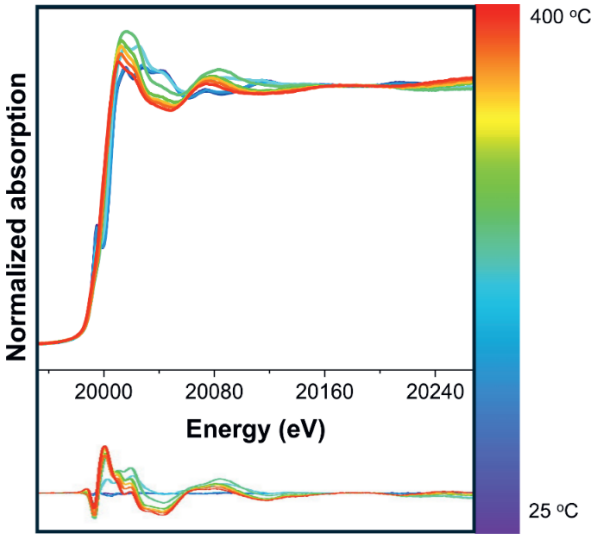


Figure 2.14-S In situ XANES results obtained during the reduction of the Ir/MoO_3 system showing the progressive change in Mo K-edge. The reduction protocol used is the R400. The result indicates that the pre-edge feature started to disappear at 170 °C, similar to the condition when the R200 protocol was applied

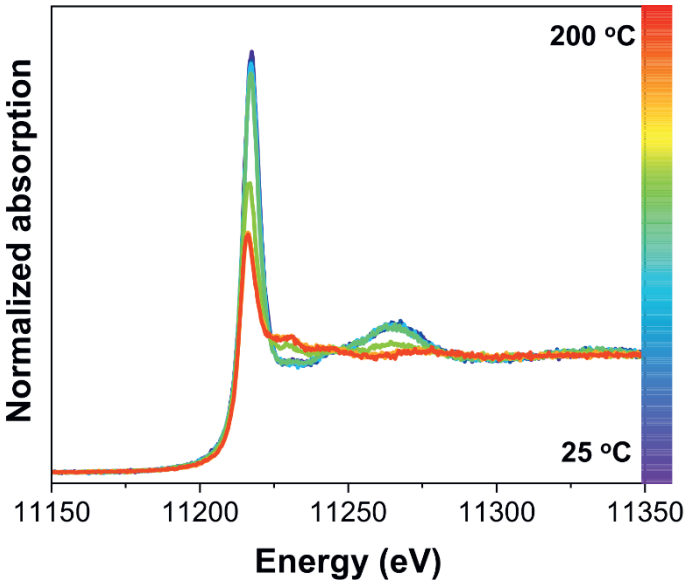


Figure 2.15-S In situ XANES results obtained during the reduction of the Ir/MoO_3 system showing the progressive change in Ir L_3-edge. The reduction protocol used is the R200. The result indicates that the white line intensity started to decrease at ~159 °C.

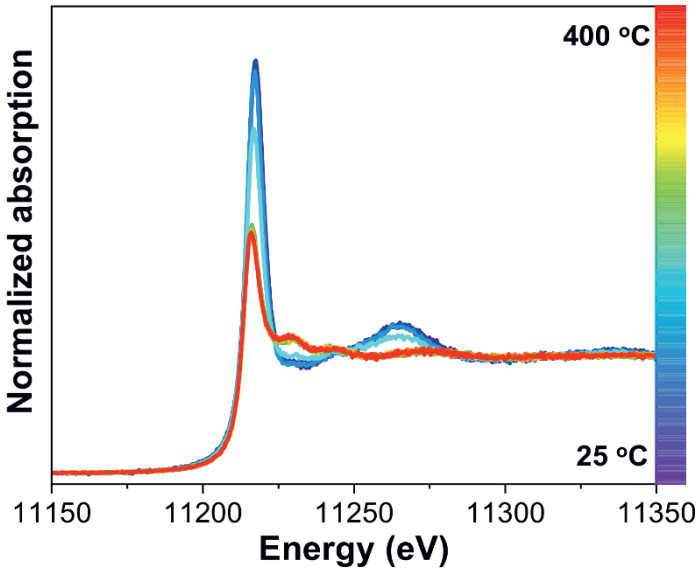


Figure 2.16-S In situ XANES results obtained during the reduction of the Ir/MoO_3 system showing the progressive change in Ir L_3-edge. The reduction protocol used is the R400. The result indicates that the white line intensity started to decrease at ~157 °C.

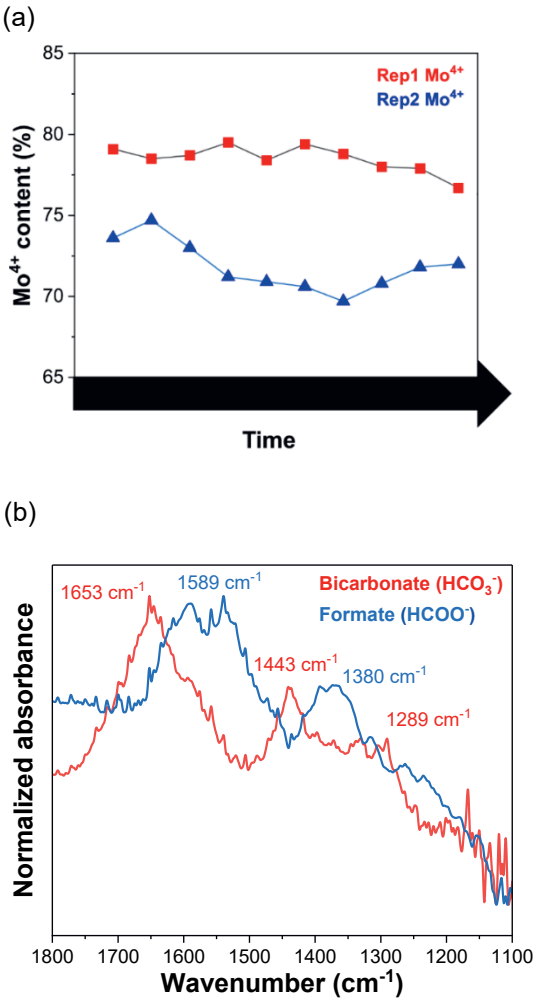


Figure 2.17-S (a) The Mo^{4+} content obtained from the in situ XANES of Ir/MoO_3 (reduced using the R200 reduction protocol), using the linear combination fitting (LCF), after holding the temperature at 75 °C, under reaction conditions. In the first temperature sequence, the Mo^{4+} content is shown in red, while the Mo^{4+} content obtained from the second temperature sequence is shown in blue. The result shows the decrease in Mo^{4+} content in the second temperature sequence, indicating in situ reduction of the catalyst under reaction conditions. **(b)** The multivariate curve resolution-alternative least squares (MCR-ALS) method, applied to the *operando* DRIFTS data (collected at 10 bar and temperatures of 75 °C, 225 °C, and subsequent cooling to 75 °C). The result shows the corresponding wavenumber of each observed species.

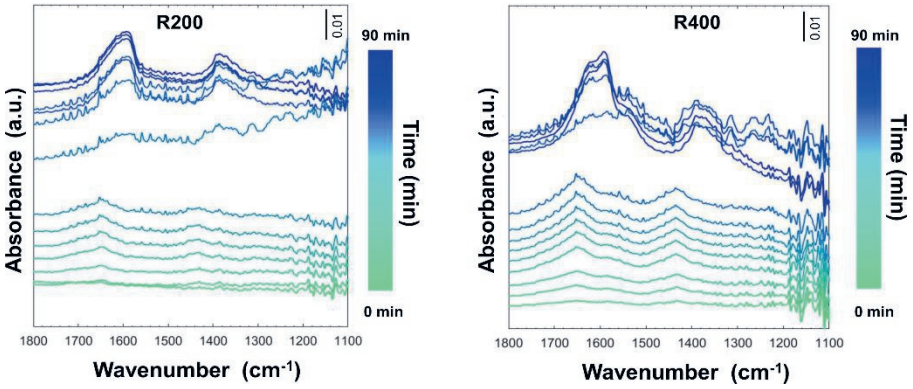


Figure 2.18-S *Operando* DRIFTS result in the C-O region (1100 - 1800 cm^{-1}) for Ir/MoO_3 at two different reduction protocols, R200 and R400, during CO_2 hydrogenation at 75 °C, 225 °C, and cooling to 75 °C and 10 bar

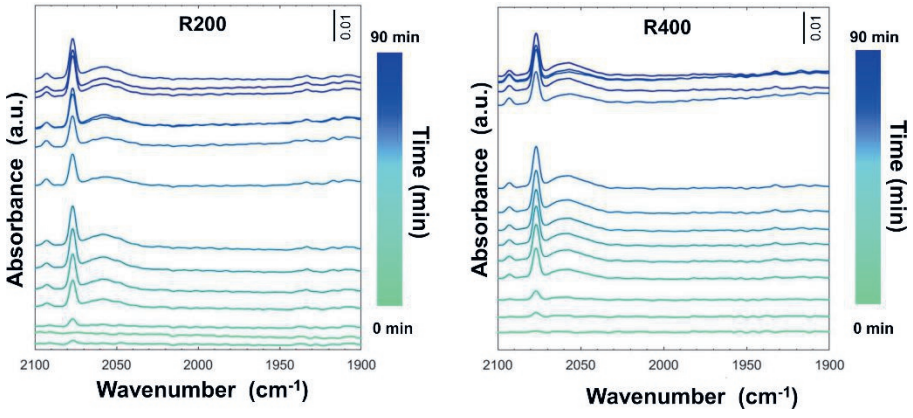


Figure 2.19-S Operando DRIFTS result in the carbonyl region (1900 - 2100 cm^{-1}) for Ir/MoO_3 at two different reduction protocols, R200 and R400, during CO_2 hydrogenation at 75 °C, 225 °C, and cooling to 75 °C and 10 bar

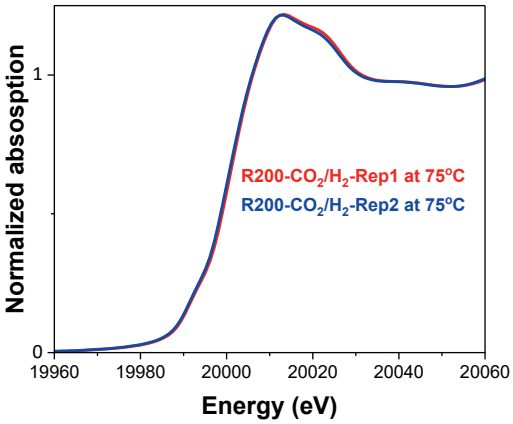


Figure 2.20-S *In situ* XANES of Mo K-edge in the Ir/MoO_3 (reduced using the R200 reduction protocol), after holding the temperature at 75 °C in the first (red) and second (blue) temperature sequence

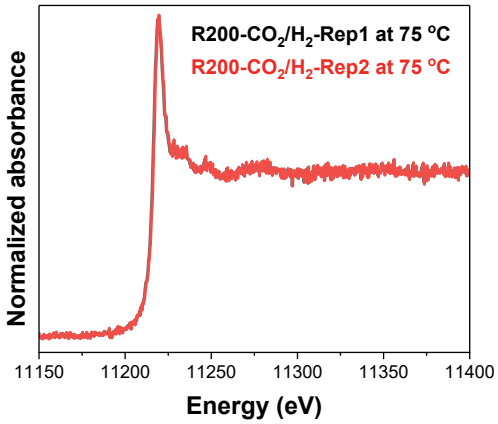


Figure 2.21-S *In situ* XANES of Ir L_3-edge in the Ir/MoO_3 (reduced using the R200 reduction protocol), after holding the temperature at 75 °C in the first (red) and second (blue) temperature sequence

References

[1] H. Kim, J.B. Cook, H. Lin, J.S. Ko, S.H. Tolbert, V. Ozolins, B. Dunn, charge storage properties of MoO_{3-x}, Nat. Mater. 16 (2017).

[2] A. Samsuri, F. Salleh, T. Shafazila, T. Saharuddin, R. Othaman, Study on the Reduction Behaviour of Nickel Doped Molybdenum Trioxide by Study on the Reduction Behaviour of Nickel Doped Molybdenum Trioxide by Using Carbon Monoxide as Reductant, (2016).

[3] P. Sun, F. Teng, Z. Yang, X. Yang, S. Zhai, S. Liang, W. Gu, W. Hao, S. Shi, activity of MoO_3 and potential application for, (2020) 2475-2482

3 Investigating the influence of molybdenum loading on the performance of Ir/*x*Mo/Al_2O_3 catalysts in CO_2 hydrogenation to methanol

Ahmad Alrefaei, Atul Bansode, Atsushi Urakawa

The publication is in preparation

Summary

This work investigates the influence of molybdenum (Mo) loading on the structural and catalytic behavior of (1.5)Ir/*x*Mo/Al_2O_3 catalysts for CO_2 hydrogenation. Catalysts with 19, 32, and 48 weight percent (wt%) of Mo on γ-Al_2O_3 were synthesized to evaluate how Mo dispersion and crystallinity evolve with loading. XRD analysis showed that low Mo loading (19 wt%) leads to highly dispersed amorphous Mo species, whereas higher loadings (32 wt% and 48 wt% promote the formation of crystalline Mo phases, including MoO_3. Upon iridium (Ir) impregnation, large iridium oxide (IrO_2) crystallites were observed at low Mo loading, whereas higher Mo loading resulted in IrO_2 undetectable by XRD, suggesting stronger Ir-Mo interactions. Catalytic testing at 300 bar revealed that low Mo loading leads to higher methanol (MeOH)-derived product selectivity (59%) at 150 °C. Increasing Mo loading suppressed MeOH selectivity. *Operando* DRIFTS revealed that higher Mo loading suppresses Lewis acid (LA)-associated formate species (types I and II), while monodentate formate remains unchanged. This suppression of LA-associated intermediates correlates directly with a decrease in MeOH-derived product selectivity. Overall, Mo loading is shown to be a key parameter governing surface structure, intermediate evolution, and catalytic function in CO_2 hydrogenation.

3.1 Introduction

Energy production from sustainable sources has become a crucial focus in addressing the global challenge of climate change [1–3]. Utilizing CO_2 as an abundant carbon source for energy production offers a promising solution. This approach not only enables the generation of energy from sustainable sources but also significantly reduces CO_2 emissions, which are a major contributor to global warming. Various technologies have been explored for converting CO_2 into chemical energy carriers, with the hydrogenation of CO_2 to methanol (MeOH) and MeOH-derived products being the most extensively studied [4–8], since MeOH is considered the most versatile chemical as an energy carrier and an alternative C1 feedstock for the petrochemical industry. The hydrogenation of CO_2 to MeOH is a catalytic process that is favored at high pressure and low temperature [9,10]. Equilibrium calculations indicate that the hydrogenation of CO_2 to MeOH could achieve 100% conversion and 100% selectivity to MeOH if the system is operated at low temperatures and high pressures [11,12]. However, due to the high stability of CO_2 molecules, an active catalyst is required at these temperatures [13]. Copper-zinc (Cu-Zn) catalysts are known for their high activity in CO_2 hydrogenation, and numerous studies have investigated this catalytic system [9,14]. However, this catalytic system is known to operate at higher temperatures (220-275 °C) and pressures (50 -100 bar) [9,10,15]. As per the equilibrium calculations mentioned previously (Figure 1.2(a)), operating at a lower temperature and higher pressure is thermodynamically more favorable for achieving higher CO_2 conversion and MeOH selectivity. This occurs because the condensation of the products (MeOH and H_2O) under these conditions separates them from the reactant gases, thereby driving the reaction equilibrium forward [16,17].

A wide range of noble metals has been explored for CO_2 hydrogenation, largely because of their ability to activate hydrogen even at low temperatures [9,13]. Among these, rhenium (Re) systems have shown particularly promising behavior. When compared with Cu-Zn catalysts under similar conditions, Re-based catalysts demonstrated superior overall performance [10]. These studies further revealed that the coexistence of different Re species working together is essential for enhancing MeOH formation. Iridium (Ir) has also attracted attention. Mechanistic studies of low-temperature CO_2 hydrogenation using an Ir complex in a gas-solid setup demonstrated remarkably high MeOH selectivity [18]. The findings emphasized that two distinct Ir sites must operate cooperatively and that the distance between them plays a key role in promoting MeOH production [18]. In addition, Chapter 2 investigated Ir supported on various reducible oxides, where the Ir/MoO_3

system exhibited a notably high production rate of MeOH-derived products compared to the other catalysts. This enhanced performance was attributed to the dynamic behavior of molybdenum (Mo) species during the reduction step and under reaction conditions. Such structural and electronic changes in Mo were found to strongly influence product selectivity, favoring MeOH-derived products. This insight motivated a deeper investigation into how Mo loading affects catalytic behavior.

Mo was impregnated onto γ-Al_2O_3 at different loadings. Alumina was chosen as the support because Mo/Al_2O_3 systems have been widely studied in various reactions, including hydrodeoxygenation, hydrodesulfurization, and other hydrotreating processes [19–23]. After preparing the Mo-modified supports, Ir was impregnated onto each. The catalytic activity of the resulting catalysts was evaluated at 300 bar across several reaction temperatures, and a range of characterization techniques was employed to elucidate the role of Mo in shaping the catalytic performance.

3.2 Experimental section

3.2.1 Catalyst synthesis:

The following reagents were used as received. Ir(III) chloride hydrate (CAS No. 10025-83-9) was purchased from Precious Metals Online. Ammonium molybdate tetrahydrate (CAS No. 12054-85-2) was purchased from Merck Sigma. γ-Al_2O_3 99.9% (CAS No. 1344-28-1) was purchased from BASF Nederland. The catalysts were prepared using the sequential Wet Impregnation (WI) method with an aqueous solution of the respective metal salt. First, the Mo precursor solution was dissolved in demineralized water. After the Mo precursor was fully dissolved, γ-Al_2O_3 was added to the solution, and the mixture was stirred at 200 rpm overnight at 50 °C. followed by drying at 110 °C for 12 h, and calcination under air at 500 °C for 3 h. The Mo loading was calculated based on the elemental ratios Al/Mo = 8 ((19)Mo/Al_2O_3), 4 ((32)Mo/Al_2O_3), and 2 ((48)Mo/Al_2O_3). To obtain these elemental ratios, 1.3, 2.6, and 5.2 g of the desired Mo precursor were calculated, as shown in the appendix.

Ir(III) chloride hydrate (0.071 g to obtain a metal loading of 1.5 wt% Ir per support) was dissolved in 50 mL of deionized water. The amount of metal salt was calculated based on 3 g of support material. After the salt was completely dissolved in the water (0.5-0.6 h), 3 g of the support material was added to

the solution. The mixed solution was then stirred at 200 rpm and 50 °C overnight. Subsequently, the drying process was performed in air at 110 °C for 12 h. The obtained powder was crushed and calcined in air at 500 °C for 3 h.

3.2.2 Catalysts characterization:

3.2.2.1 H_2-temperature program reduction (H_2-TPR):

200 mg of catalyst was packed inside a quartz tube reactor. H_2 flow was introduced into the reactor, and a heating rate of 10 °C/min was used until reaching a final temperature of 700 °C. The catalysts were held at 700 °C for 10 min. The H_2 signal was recorded online with a thermal conductivity detector (TCD).

3.2.2.2 X-ray diffraction (XRD):

The XRD patterns were attained using a Bruker AXS D8 Advance diffractometer. The detector used in the experiment was a Lynxeye-XE-T position-sensitive detector, which enabled efficient and accurate data collection. The recorded data in the range of 5° to 90° was evaluated using the DIFFRAC.EVA software, which provided analysis and interpretation of the obtained diffraction patterns.

3.2.3 Catalytic activity

The catalytic activity was evaluated in a custom-made high-pressure setup, as shown in Figure 2.1. In a typical test, a 125 mg catalyst was packed into a 1/4-inch stainless steel reactor tube (ID, 2.79 mm). Before loading, the catalysts were pelletized, crushed, and sieved to obtain a particle size range of 90-300 µm. Quartz wool was used to support the catalyst in the reactor. The catalyst was reduced at 400 °C with 90% H_2/Ar (20 mL/min) for 1.5 h under atmospheric pressure. After cooling to 35 °C, the $H_2/CO_2/N_2$ mixture (70.5/23.5/6 vol%) was fed into the reactor and pressurized to 300 bar. The space velocity was maintained at 10 NL/g_{cat} h. The products were analyzed by an online gas chromatograph (Compact GC 4.0 manufactured by Global Analyzer Solutions) equipped with a flame ionization detector for the detection of CH_4, MeOH, methyl formate (MF), dimethyl ether (DME), and ethanol (EtOH), and two thermal conductivity detectors, one for the detection of H_2, N_2, CH_4, and CO. This TCD uses Ar as the mobile phase. The second TCD was used to detect CO_2, and He is the mobile phase. The carbon balance was monitored to be within 97 - 102%. The values presented were obtained by averaging the measurements only after steady-state had been reached. A single representative value was then reported for each condition

$$\mathrm{CO_2\ conversion} = \frac{\mathrm{CO_{2\ in}} - \mathrm{CO_{2\ out}}}{\mathrm{CO_{2\ in}}}\ or\ \frac{\sum \mathrm{n}_{C,i} \times \mathrm{Concentration}_i}{\mathrm{CO_{2\ in}}}$$

$$\mathrm{Selectivity} = \frac{\mathrm{n}_{C,i} \times \mathrm{Concentration}_i}{\sum \mathrm{n}_{C,i} \times \mathrm{Concentration}_i}$$

3.2.4 *Operando* diffuse reflectance infrared fourier transform spectroscopy - mass spectrometry (DRIFTS-MS)

The *operando* DRIFTS was performed utilizing a Thermo Scientific Nicolet 6700 FT-IR and a Pfeiffer OmniStar GSD 300C mass spectrometer (MS) as shown in Figure 2.2. The spectrometer is equipped with a liquid-nitrogen-cooled mercury-cadmium-telluride (MCT) detector to collect the spectra while the MS analyzes the outlet gas stream. Gas flow control in the setup was facilitated by six Bronkhorst mass flow controllers, which regulated the flow rates of H_2, CO_2, and He. Switching between the two reactant gas streams was achieved using a 4-way valve. Back pressure regulators (Bronkhorst) were employed to control the pressure of the reaction cell and the vent side, maintaining the desired pressures within the system. A 40-50 mg of catalyst powder was placed inside a cylindrical cavity, having a diameter of 3 mm and a vertical length of 3 mm, located in a Harrick Praying Mantis DRIFTS accessory. Before the measurements, the catalyst was reduced at the desired temperature using a mixture of H_2 and He gases (90/10) for 1.5 hours. Subsequently, the sample was cooled to the reaction temperature of 75 °C and pressurized to 10 bar under a He stream. The reaction cell was exposed to a CO_2:H_2 feed with a 1:3 ratio (total flow rate of 15 mL/min). The spectra were acquired at a resolution of 4 cm^{-1}. 10 spectra were averaged and collected after 13.3 s.

3.3 Results and discussion

3.3.1 The structural evolution of the *x*Mo/Al_2O_3 catalysts with varying Mo loading

The structural properties of the Mo-impregnated on Al_2O_3 were investigated by XRD to identify the phases formed at different Mo loadings. Figure 3.1 shows the XRD patterns of different Mo loading impregnated on Al_2O_3 supports along with the diffraction pattern of the pristine γ-Al_2O_3. The γ-

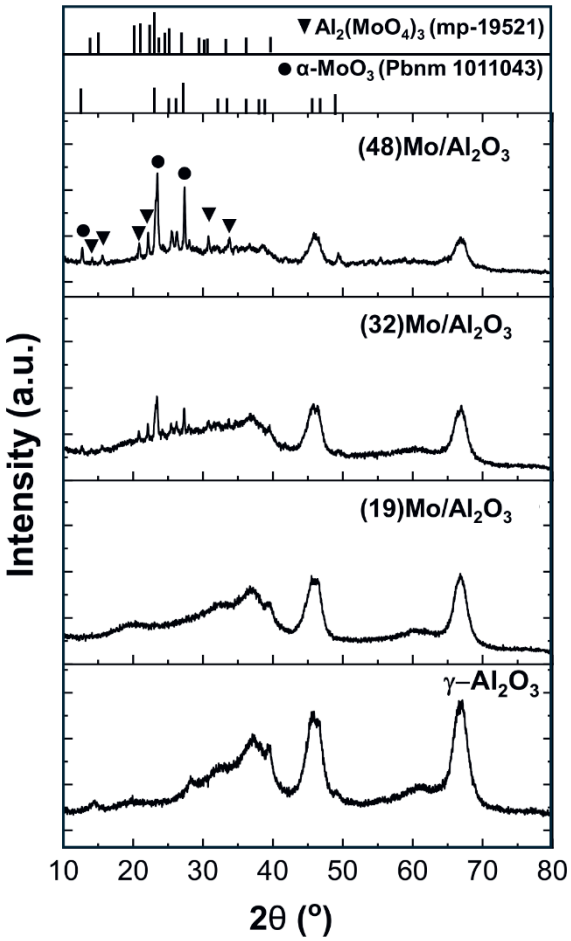


Figure 3.1 The X-ray diffraction patterns for γ-Al_2O_3 before impregnation with Mo loadings, alongside the three different Mo loadings 19,32, and 48 wt% over Al_2O_3. The computed diffraction patterns of the references, alumina molybdate, and the orthorhombic phase MoO_3, can be found at the top of the figure. The result indicates the evolution of crystallite structure corresponding to α-MoO_3 and alumina molybdate, as the Mo loading increases

Al_2O_3 exhibits broad and weak diffraction peaks at 2θ ≈ 37°, 47°, and 66°, which are characteristic of a microcrystalline structure with a small crystallite size (~5 nm), indicating its low crystallinity and amorphous character [24–26]. The γ-Al_2O_3 diffraction remains unchanged even after thermal treatment at 500 °C during the calcination step, excluding potential structural changes associated with high temperature. When different amounts of Mo were loaded onto Al_2O_3, the overall diffraction pattern varied with Mo loading. For the catalyst with the lowest Mo loading (19)Mo/Al_2O_3, the diffraction pattern

shows no significant Mo peaks. At this low loading, Mo anchors on the partially dehydrated alumina surface, forming well-dispersed, amorphous oligomeric species [27,28]. Furthermore, its local concentration is too low to nucleate and grow into a long-range ordered crystalline phase, leading to the absence of reflections attributable to crystalline Mo phases and indicating a high dispersion of Mo species at this low loading.

At a higher Mo loading ((32)Mo/Al_2O_3), the diffraction shows pronounced reflections, indicative of the development of different crystalline Mo phases. Comparison with reference diffraction patterns of aluminum molybdate ($Al_2(MoO_4)_3$) (20.7°, 15.3°, 22.3°, and 30.8°), and orthorhombic MoO_3 (α-MoO_3) (12.6°, 23.2°, and 27.5°) confirms the coexistence of the two phases, as shown in Figure 3.1 [21,29–31]. The formation of $Al_2(MoO_4)_3$ is attributed to a solid-state reaction during calcination, where isolated molybdate monomers (MoO_4^{2-}) react with aluminum cations on the alumina lattice to form $Al_2(MoO_4)_3$ [27,32]. The thermodynamically stable α-MoO_3 is the phase formed upon calcining the polymolybdate at 500 °C [32]. Its presence, evidenced by the 23.2° and 27.5° peaks, suggests that the polymolybdate has achieved a long-range order for crystallite formation during the calcination step [27,33]. The highest Mo loading ((48)Mo/Al_2O_3) leads to a high concentration of Mo species that promotes the nucleation of all Mo-related phases, resulting in larger crystallites. This is evident in the sharper diffraction peaks, the increased intensity of $Al_2(MoO_4)_3$ and α-MoO_3 peaks, and the concurrent decrease in the γ-Al_2O_3 reflections in the (48)Mo/Al_2O_3 diffraction pattern [33,34]. In conclusion, the structural evolution of *x*Mo/Al_2O_3 catalysts strongly depends on the Mo loading. At low Mo loading, the material primarily consists of highly dispersed amorphous Mo species. In contrast, higher loadings lead to the crystallization of distinct phases, such as aluminum molybdate and the thermodynamically stable α-MoO_3.

3.3.2 The effect of Ir impregnation on *x*Mo/Al_2O_3 structure

The 1.5 wt% Ir was impregnated onto the *x*Mo/Al_2O_3 supports with varying Mo loadings, and the corresponding diffractograms of the catalysts: (1.5)Ir/(19)Mo/Al_2O_3, (1.5)Ir/(32)Mo/Al_2O_3, and (1.5)Ir/(48)Mo/Al_2O_3 are shown in Figure 3.2 (a). The diffraction pattern of (1.5)Ir/(19)Mo/Al_2O_3 confirms the presence of IrO_2, evidenced by the characteristic reflections at 28°, 34°, and 40°. As the Mo loading increases in the support (1.5)Ir/(32)Mo/Al_2O_3, the intensity of IrO_2 peaks reduces, as shown in Figure 3.2 (a). Interestingly, the diffraction peaks corresponding to α-MoO_3 and aluminum molybdate (Figure

3.2 (a)) disappear after Ir impregnation, indicating a change in the Mo structure from larger crystalline to smaller crystallite or amorphous phase after Ir impregnation. When the Mo loading increases further, as shown in the (1.5)Ir/(48)Mo/Al_2O_3 diffraction (Figure 3.2 (a)), the IrO_2 reflections were suppressed entirely, while the intensity of α-MoO_3 and aluminum molybdate peaks was reduced. This result suggests that the Ir impregnation is expected to be mainly on the Mo species, which, in turn, distorts their crystalline structure.

To investigate the interaction between Ir and Mo, H_2-TPR was performed on all three catalysts. The reduction for all the catalysts as a function of temperature is shown in Figure 3.2 (b). The TPR profile of (1.5)Ir/(19)Mo/Al_2O_3 shows two separate peaks at 250 and 350 °C; the first peak corresponds mainly to the reduction of IrO_2 [35]. The second peak, observed at 350 °C, corresponds to the reduction of Mo species, which occurred at a lower temperature due to hydrogen spillover from Ir sites [35–37]. As the Mo species loading increases (1.5)Ir/(32)Mo/Al_2O_3 and (1.5)Ir/(48)Mo/Al_2O_3, the two peaks appeared to move closer until the two peaks overlapped as observed in the TPR profile of (1.5)Ir/(48)Mo/Al_2O_3. This result suggests that the Ir species, which is typically reduced at ~150 °C or even lower temperature (Figure 3.2-S, Appendix), interacts strongly with the Mo species. The strong interaction between Ir and Mo shifts the IrO_x reduction peak to higher temperatures [38,39].

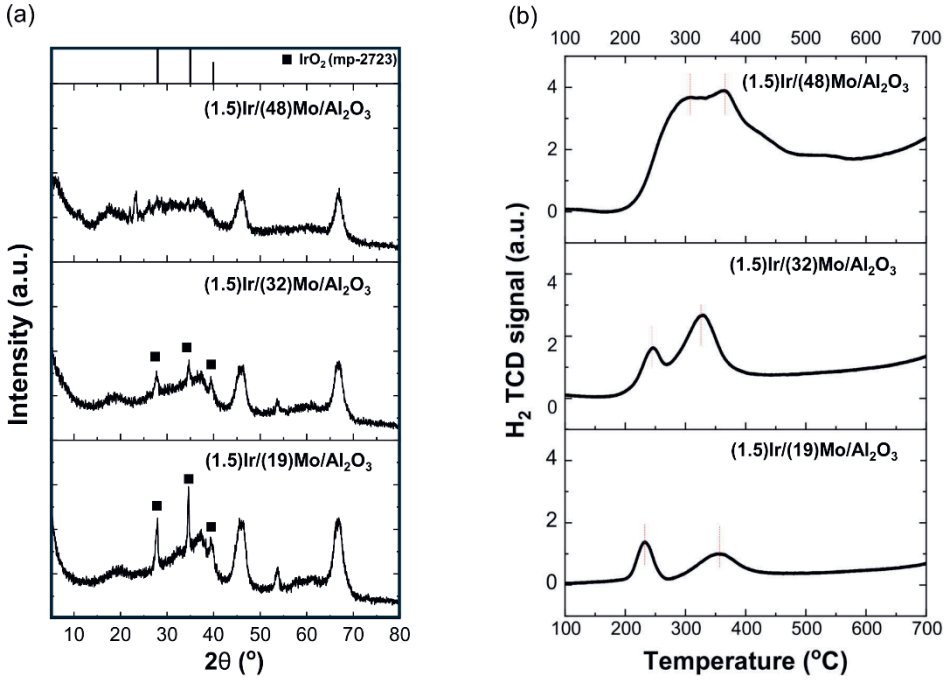


Figure 3.2 (a) The XRD pattern of (1.5)Ir/(19)Mo/Al_2O_3, (1.5)Ir/(32)Mo/Al_2O_3, and (1.5)Ir/(48)Mo/Al_2O_3 alongside the computed diffraction of IrO_2. The result shows an increase in the IrO_2 crystallite size as the Mo loading decreases and the disappearance of Mo-related peaks after Ir impregnation, suggesting a distortion in the crystalline structure. **(b)** The H_2-TPR profile of (1.5)Ir/(19)Mo/Al_2O_3, (1.5)Ir/(32)Mo/Al_2O_3, and (1.5)Ir/(48)Mo/Al_2O_3, which was performed under hydrogen from room temperature to 700 °C. The result indicates that the gap between the two peaks narrows, eventually reaching a high Mo loading ((1.5)Ir/(48)Mo/Al_2O_3) at which the two peaks overlap. This result indicates strong interaction between Ir and Mo, consistent with the XRD, where no IrO_2 was observed at higher Mo loading

3.3.3 The catalytic activity performance of (1.5)Ir/*x*Mo/Al_2O_3

The catalytic performance of the three catalysts: (1.5)Ir/(19)Mo/Al_2O_3, (1.5)Ir/(32)Mo/Al_2O_3, and (1.5)Ir/(48)Mo/Al_2O_3 was evaluated for CO_2 hydrogenation at 300 bar and three reaction temperatures: 150 °C, 175 °C, and 225 °C. After completing this temperature sequence, the system was cooled back to 150 °C to assess any change in the catalyst performance that might occur if another temperature sequence were implemented. Prior to the reaction, all catalysts were reduced under a H_2/Ar (9:1) atmosphere at 400 °C for 1.5 h to ensure the reduction of all active species Ir and Mo, as indicated by the H_2-TPR profile (Figure 3.2 (b)). The CO_2 conversion and product selectivity for each catalyst are shown in Figure 3.3.

A comparison of MeOH-derived product selectivity across all catalysts reveals a clear dependence on Mo loading. During the first run at 150 °C, the catalyst with the lowest Mo loading, (1.5)Ir/(19)Mo/Al_2O_3 (Figure 3.3 (a)), exhibited the highest MeOH-derived product selectivity (59%), followed by (1.5)Ir/(32)Mo/Al_2O_3 (30%) and (1.5)Ir/(48)Mo/Al_2O_3 (15%). As the temperature increased to 175 °C and 225 °C, MeOH selectivity decreased for (1.5)Ir/(19)Mo/Al_2O_3 while CO selectivity increased, indicating the increased activity for the RWGS reaction at elevated temperatures. In contrast, (1.5)Ir/(32)Mo/Al_2O_3 showed nearly constant MeOH selectivity with increasing temperature, whereas (1.5)Ir/(48)Mo/Al_2O_3 exhibited a different trend, with MeOH selectivity increasing as temperature increased. Upon cooling back to 150 °C (second run), all catalysts showed significant improvements in MeOH selectivity. The selectivity increased from 59% to 73% for (1.5)Ir/(19)Mo/Al_2O_3, from 30% to 65% for (1.5)Ir/(32)Mo/Al_2O_3, and most dramatically from 15% to 70% for (1.5)Ir/(48)Mo/Al_2O_3. Since the Ir loading was kept constant, this behavior confirms that the observed enhancement in MeOH selectivity is primarily associated with the increase in Mo species. The increase in Mo species resulted in a higher possibility of an *in situ* reduction of those Mo species and modification of their chemical state, as discussed in Chapter 2.

Regarding CO_2 conversion, all catalysts showed increasing conversion with increasing temperature, as the kinetics of the CO_2 hydrogenation reaction are favored at higher temperatures. The (1.5)Ir/(32)Mo/Al_2O_3 achieved the highest conversion at 225 °C (4.5%), outperforming the other catalysts at this temperature. In contrast, (1.5)Ir/(48)Mo/Al_2O_3 showed no significant improvement in conversion compared to (1.5)Ir/(32)Mo/Al_2O_3, despite its higher Mo loading. These results suggest the existence of an optimal Mo loading for maximizing CO_2 conversion, as increasing or decreasing the Mo loading does not further enhance catalytic performance and may even reduce it.

To further understand the role of Mo in the catalytic performance, an additional catalyst containing the same Ir loading (1.5 wt%) but supported only on γ-Al_2O_3 ((1.5)Ir/Al_2O_3) was prepared and tested under identical reaction conditions and reduction protocol as shown in Figure 3.1-S (b) (Appendix). The catalytic activity tests showed no measurable activity at 150 °C and 175 °C. However, at 225 °C, a MeOH-derived product selectivity of 18% was observed, significantly lower than the 32% achieved with the catalyst containing the lowest Mo loading ((1.5)Ir/(19)Mo/Al_2O_3) under the

same reaction conditions (Figure 3.3 (a)). Similarly, the CO_2 conversion over (1.5)Ir/Al_2O_3 at 225 °C was approximately 0.6%, compared to 3.3% over Ir/(19)MoO_3/Al_2O_3. These results demonstrate the pronounced promotional effect of Mo incorporation on the CO_2 hydrogenation activity. Even at low Mo loadings, the presence of Mo substantially enhances both CO_2 conversion and MeOH selectivity compared to the (1.5)Ir/Al_2O_3 catalyst, highlighting its critical role in facilitating active site formation for MeOH and in modifying surface properties, which leads to an improvement in catalytic activity.

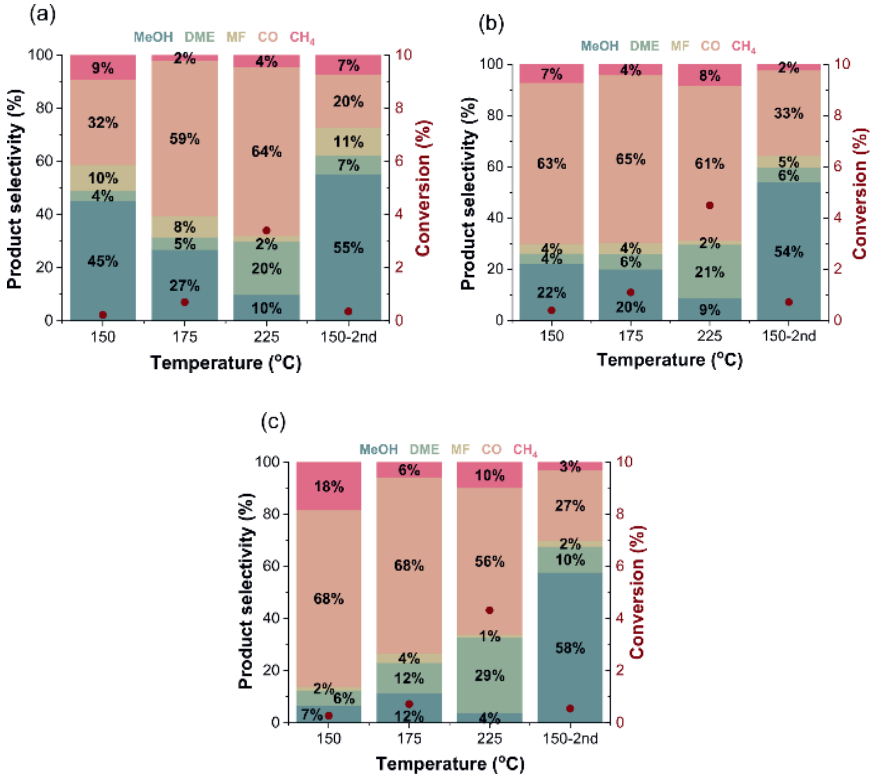


Figure 3.3 The catalytic activity performance of CO_2 hydrogenation at 300 bar, using R400 reduction protocol and different reaction temperatures for **(a)** (1.5)Ir/(19)Mo/Al_2O_3, **(b)** (1.5)Ir/(32)Mo/Al_2O_3, **(c)** (1.5)Ir/(48)Mo/Al_2O_3. The results show the product selectivity on the left y-axis and the conversion on the right. The result indicates the increase in MeOH selectivity as the Mo loading decreases (150 °C). However, the enhancement in MeOH selectivity in the second 150 °C increase, as Mo loading increases

3.3.4 The effect of Mo loading on the product selectivity over (1.5)Ir/*x*Mo/Al_2O_3

To assess the influence of Mo loading on product selectivity, the catalytic performance of the three catalysts with varying Mo loadings was compared. As shown in Figure 3.3, the (1.5)Ir/(19)Mo/Al_2O_3 catalyst exhibits higher MeOH-derived product selectivity at lower reaction temperatures, primarily due to increased MeOH formation (Figure 3.3 (a)). Under these conditions, CO_2 hydrogenation likely proceeds via formate intermediates, favoring the formation of MeOH at lower temperatures [40]. As temperature increases, formate intermediates decompose, promoting CO formation via RWGS [41]. When the Mo loading is increased, the MeOH-derived product selectivity increases with temperature, as observed for (1.5)Ir/(48)Mo/Al_2O_3 in Figure 3.3 (c). The distinct behavior between these two systems, (1.5)Ir/(19)Mo/Al_2O_3 and (1.5)Ir/(48)Mo/Al_2O_3, can be attributed mainly to the change in the surface chemistry resulting from higher Mo impregnation. The Mo impregnation was found to affect the Lewis acid sites on Al_2O_3, leading to the formation of Bronsted acid sites [42]. The presence of Bronsted acid sites and the increase in reaction temperature enhance the MeOH dehydration reaction, leading to the formation of MeOH-derived products, such as DME as observed in Figure 3.3 (c) [43,44]. The shift in product selectivity with increasing Mo loading is attributed to Mo-induced changes in surface properties, as reflected by the loss of MeOH selectivity at low Mo loading with increasing temperature and the enhanced DME formation at higher Mo loading with increasing temperature.

In addition, at low Mo loading, the Mo species are highly dispersed on the Al_2O_3 surface, as confirmed by the XRD data in Figure 3.2 (a). These Mo species interact strongly with the support, forming less reducible Mo species [45]. At higher Mo loading, however, the surface contains a larger amount of Mo species, mainly, MoO_3 crystallites, which are more easily reducible [45]. The reduction of these Mo species increases the number of potential active sites on the surface, which is expected to strongly impact catalytic activity, as observed by the increase in the CO_2 conversion from 2.3% in (1.5)Ir/(19)Mo/Al_2O_3 to 4.5% in (1.5)Ir/(32)Mo/Al_2O_3, (Figure 3.3 (a) and (b)).

Another notable observation is made on comparing the product selectivity at 150 °C between the first and second runs. At low Mo loading (1.5)Ir/(19)Mo/Al_2O_3, the catalyst shows almost only a 14% increase in the

product selectivity between the two runs, as illustrated in Figure 3.3 (a). However, as the Mo loading increases ((1.5)Ir/(32)Mo/Al_2O_3 and (1.5)Ir/(48)Mo/Al_2O_3), the difference in product selectivity between the first and second 150 °C runs becomes significant, with remarkably higher MeOH selectivity in the second run. This behavior aligns with the findings presented in Chapter 2, where a significant increase in MeOH-derived product selectivity was observed during the second temperature sequence for the Ir/MoO_3 catalyst (Figure 2.6). The Mo species undergo *in situ* reduction during the reaction, producing more reduced Mo species in the second temperature sequence, an effect also confirmed by the *in situ* XANES (Figure 2.3). The formation of these reduced Mo species promotes selectivity for MeOH-derived products during the second run. Therefore, at higher Mo loadings ((1.5)Ir/(48)Mo/Al_2O_3), where the Mo species have a higher potential for reduction, more Mo species will undergo *in situ* reduction, leading to an enhanced MeOH-derived product selectivity during the second 150 °C run. In contrast, at lower Mo loadings ((1.5)Ir/(19)Mo/Al_2O_3), where the Mo species are more dispersed and less reducible, the chemical state of Mo remains largely unchanged between the two runs, leading to minimal variation in product selectivity.

3.3.5 State of Ir on the catalyst surface

The XRD data shown in Figure 3.2 (a) reveal that at low Mo loading, Ir impregnation leads to the formation of distinct IrO_2 crystallites. As the Mo loading increases, these IrO_2 crystallites become smaller, and at the highest Mo loading (1.5)Ir/(48)Mo/Al_2O_3, no Ir-related reflections were observed, suggesting the absence of crystalline Ir species. However, the state of Ir under reaction conditions can differ significantly. To investigate the Ir environment under reaction conditions, *operando* DRIFTS measurements were performed. During the experiment, each catalyst was reduced at 400 °C under a H_2/He (9:1) mixture for 1.5 h, the same reduction protocol used in the catalytic activity tests. After the reduction step, the temperature was lowered to 150 °C, and the DRIFTS cell was pressurized to 10 bar using He. Once both temperature and pressure stabilized, the reactant feed (CO_2/H_2 = 1:3) was introduced. Spectra were collected throughout the reaction to monitor the evolution of surface species. The carbonyl stretching region (1900-2100 cm^{-1}) was analyzed for each catalyst to probe the Ir surface state under reaction conditions. The collected spectra during the *operando* DRIFTS for the carbonyl region is shown in Figure 3.4. For (1.5)Ir/(19)Mo/Al_2O_3, four distinct

bands were observed at 2009, 2060, 2077, and 2094 cm^{-1} (Figure 3.4 (a)), indicating the presence of multiple surface carbonyl complexes. The band at 2009 cm^{-1} corresponds to Ir-bridged carbonyl species [46,47], while those at 2060 and 2094 cm^{-1} are attributed to di-carbonyl complexes [46–48]. The broad feature at 2060 cm^{-1} may suggest overlapping contributions from several carbonyl species; tricarbonyl might exist in this case. The sharp band at 2077 cm^{-1} reflects a well-defined vibrational mode characteristic of linear carbonyl species on metallic Ir. The bands at 2060, 2077, and 2094 cm^{-1} were observed during the DRIFTS study of Ir/MoO_3 (Figure 3.3-S (b), Appendix), indicating that the Ir species were largely impregnated over the Mo species. However, the band at 2009 cm^{-1} is expected to correspond to a bridged Ir-carbonyl over Al_2O_3. Similar bands at lower wavenumbers were observed during the DRIFTS study of (1.5)Ir/Al_2O_3 (Figure 3.3-S(a), Appendix).

(1.5)Ir/(32)Mo/Al_2O_3 also exhibits bands at 2009, 2060, 2077, and 2094 cm^{-1}, as shown in Figure 3.4 (b). However, the peak-to-peak ratios and band shapes differ between the two catalysts, (1.5)Ir/(32)Mo/Al_2O_3 and (1.5)Ir/(48)Mo/Al_2O_3. The ratio of the 2077 cm^{-1} to 2060 cm^{-1} bands varies between the two catalysts, as indicated by the decrease in the 2060 cm^{-1} band and the increase in the 2077 cm^{-1} band, with increasing Mo loading. This suggests that the Ir dispersion between the two systems differs, confirming the distinct Ir environment in each catalyst, as the carbonyl types provide strong evidence of the metal environment. The Ir-bridged carbonyl was also observed over (1.5)Ir/(32)Mo/Al_2O_3, suggesting the presence of Ir species over Al_2O_3.

(1.5)Ir/(48)Mo/Al_2O_3 exhibited three bands at 2060, 2077, and 2094 cm^{-1}. However, the band at 2009 cm^{-1}, which is observed in (1.5)Ir/(19)Mo/Al_2O_3 and (1.5)Ir/(32)Mo/Al_2O_3, is absent in (1.5)Ir/(48)Mo/Al_2O_3. This result suggests that all Ir species were impregnated over Mo species, and no observable Ir-carbonyl over Al_2O_3, when Mo loading is high. This result is highly expected, as the 48% Mo loading is high and could lead to coverage of the alumina surface. In summary, the analysis of the carbonyl region obtained during the DRIFTS study under CO_2 hydrogenation conditions reveals variations in band intensity and profile, suggesting distinct Ir environments and bonding interactions on each catalyst surface.

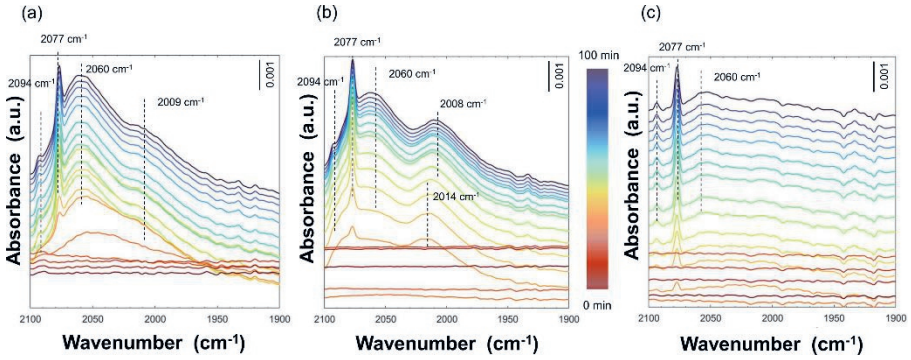


Figure 3.4 Temporal evolution of the surface species obtained from *operando* DRIFTS during CO_2 hydrogenation at 150 °C and 10 bar over **(a)** (1.5)Ir/(19)Mo/Al_2O_3, **(b)** (1.5)Ir/(32)Mo/Al_2O_3, and **(c)** (1.5)Ir/(48)Mo/Al_2O_3 using R400 reduction protocol and at 10 bar and 150 °C. The result shows the carbonyl vibration region (1900 - 2100 cm^{-1}). The results show a change in the peak-to-peak ratio among the three catalysts, suggesting a different Ir environment on their surfaces.

3.3.6 The temporal evolution of the surface species

The *operando* DRIFTS measurements were also used to investigate how Mo loading influences catalytic activity. The analysis focused on two spectral regions: the C-O stretching region (1100-1800 cm^{-1}) and the C-H region (2500-3200 cm^{-1}). The results for the C-O and C-H regions are presented in Figure 3.5 and Figure 3.6, respectively.

In the (1.5)Ir/(19)Mo/Al_2O_3 catalyst, where the Mo species are highly dispersed, the C-O region, shown in Figure 3.5 (a), displays six main bands (1325, 1393, 1450, 1592, 1615, and 1641 cm^{-1}) along with a shoulder at 1369 cm^{-1}. The presence of multiple bands indicates the formation of a complex mixture of surface species on Al_2O_3, which is further influenced by Mo. The majority of these band groups can be attributed to the coexistence of three distinct formate species: monodentate formate and bidentate formate types I and II, as reported by Ishito et al [49]. Their formation is linked to the presence of three types of Lewis acid (LA) sites on the Al_2O_3 surface: weak, medium, and strong [49,50]. These different LA sites stabilize different types of formate, depending on the adsorption geometry and proximity to the LA centers, as illustrated in Figure 3.7. The band at 1325 cm^{-1} is assigned to the monodentate formate, which typically appears together with accompanying bands at 1647 and 2892 cm^{-1} [49]. The presence of monodentate formate was hinted by observing its C-H stretching at 2892 cm^{-1}, as shown in Figure 3.6 (a) (Shoulder in green). In addition, the bands at 1393, 1592 (Figure 3.5

(a)), along with the band 2904 cm^{-1} (Figure 3.6 (a)), correspond to bidentate formate species over two LA sites (type I) [40,49]. The bands at 1615, 2845, and the shoulder at 1369 cm^{-1} are assigned to formate species interacting with nearby LA sites (Type II) [49]. Finally, the band at 1450 cm^{-1} corresponds to the symmetrical vibration of bicarbonate over Al_2O_3 [40]. Its asymmetric vibration at 1653 cm^{-1} occurs at nearly the same frequency as the Type II formate species, contributing to the overlapping features [40]. Over (1.5)Ir/(32)Mo/Al_2O_3 and (1.5)Ir/(48)Mo/Al_2O_3, bands at nearly identical wavenumbers were observed; however, their intensities and peak-to-peak ratios differ. This indicates variations in the relative surface coverage of each species, as shown in Figures 3.5 (b) and (c) and 3.6 (b) and (c). Four main surface species were identified in the C-O region of the DRIFTS data: monodentate formate, formate type I, formate type II, and bicarbonate over Al_2O_3.

To better understand the effect of Mo loading, the correlation between these species and Mo loading was investigated. The monodentate formate shows stretching vibrations at 1325, 1647, and 2892 cm^{-1}. The bands at 1325 and 2892 cm^{-1} do not exhibit any notable change as the Mo loading increases. This is supported by the shoulder next to the 2904 cm^{-1} band (Figure 3.6 (a), (b), and (c)), which is present in all catalysts, regardless of Mo loading. The bands at 1325 and 1641 cm^{-1} were not further analyzed due to overlap with neighboring bands (Figure 3.5). Overall, these observations suggest that varying the Mo loading has a minimal or negligible impact on the formation of monodentate formate. In contrast, the formate species type II, which exhibits stretching vibrations at 1615 and 2845 cm^{-1}, with a shoulder at 1369 cm^{-1}, shows a strong dependence on Mo loading. This difference is evident through the bands at 2845 cm^{-1} (Figure 3.6), which diminish and eventually disappear as the Mo loading increases, suggesting that the bidentate formate type II decreases with increasing Mo loading. This trend is suggested, as formate type II forms adjacent to LA sites. These LA sites become inaccessible upon the increase in Mo loading [42]. As Mo loading increases, it progressively blocks these LA sites, which eventually leads to a decrease in the density of these LA sites on the surface, reducing the surface's ability to stabilize formate type II. A similar trend is observed for formate type I, which has characteristic vibrations at 1393, 1592 (Figure 3.5), and 2904 cm^{-1} (Figure 3.6). A clear decrease in the 2904 cm^{-1} band is observed with increasing Mo loading, ultimately leading to its disappearance. Since formate type I is stabilized by two strong LA sites [49], the blockage in LA sites caused by higher Mo loading certainly results in a corresponding decrease in type I

formate formation. Overall, these observations demonstrate that increasing Mo loading primarily affects formate species associated with LA sites (type I and II), while monodentate formate remains largely unaffected. This change in the formate associated with LA sites primarily affects the formation of MeOH-derived products at 150 °C, particularly as the Mo loading increases, as observed in the catalytic activity results (Figure 3.3). Finally, the bicarbonate species over Al_2O_3, indicated by the band at 1450 cm^{-1}, showed no observable change as Mo loading increased, suggesting no obvious effect on this species with Mo loading. This is expected since the bicarbonate is adsorbed over Al_2O_3.

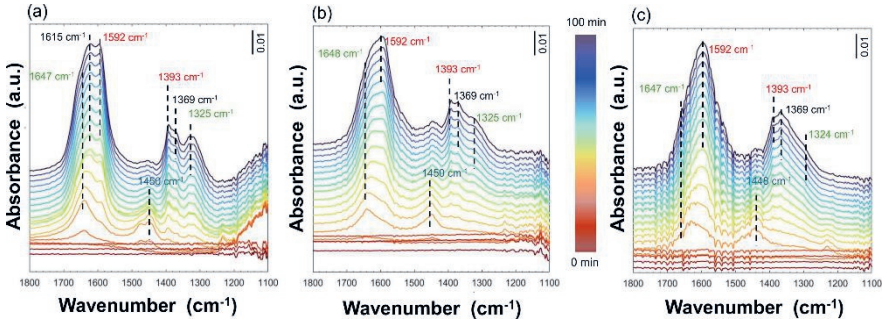


Figure 3.5 Temporal evolution of the surface species in the C-O stretching region during the CO_2 hydrogenation at 150 °C and 10 bar, which was reduced using the R400 reduction protocol. The results shown were obtained for the three different prepared catalysts: **(a)** (1.5)Ir/(19)Mo/Al_2O_3, **(b)** (1.5)Ir/(32)Mo/Al_2O_3, and **(c)** (1.5)Ir/(48)Mo/Al_2O_3. The monodentate formate stretching vibration is highlighted in green, the formate type I stretching vibration is highlighted in red, and the formate type II stretching vibration is highlighted in black.

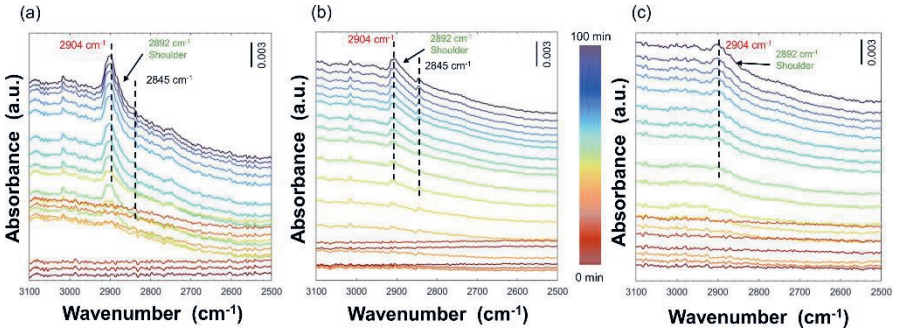


Figure 3.6 Temporal evolution of the surface species in the C-H stretching region during the CO_2 hydrogenation at 150 °C and 10 bar, which was reduced using the R400 reduction protocol. The results shown were obtained for the three different prepared catalysts: **(a)** (1.5)Ir/(19)Mo/Al_2O_3, **(b)** (1.5)Ir/(32)Mo/Al_2O_3, and **(c)** (1.5)Ir/(48)Mo/Al_2O_3. The monodentate formate stretching vibration is highlighted in green (Shoulder), the formate type I stretching vibration is highlighted in red, and the formate type II stretching vibration is highlighted in black

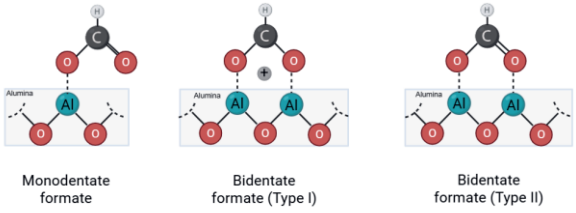


Figure 3.7 Proposed structure of the three types of formate species over Al_2O_3. These three formate types have an adsorption geometry depending on their proximity to LA sites over Al_2O_3 surface [49].

3.4 Conclusion

The effect of Mo loading was investigated by preparing catalysts with different Al/Mo elemental ratios: 8 ((19)Mo/Al_2O_3), 4 ((32)Mo/Al_2O_3), and 2 ((48)Mo/Al_2O_3). The structural analysis of the supports after Mo impregnation revealed that low Mo loading ((19)Mo/Al_2O_3) leads to well-dispersed Mo species, while higher Mo loadings ((32)Mo/Al_2O_3) and ((48)Mo/Al_2O_3) result in the formation of crystalline Mo phases. To further assess catalytic performance, 1.5 wt% Ir was impregnated onto each support. The structural characterization showed that large IrO_2 crystallites form at low Mo loading, and these crystallites and become progressively smaller as the Mo loading

increases. The catalytic activity was evaluated for CO_2 hydrogenation at 300 bar and at three reaction temperatures: 150 °C, 175 °C, and 225 °C. After completing this temperature sequence, the system was cooled back to 150 °C to assess the catalyst's performance during a second temperature cycle. The results show that the highest MeOH-derived product selectivity at 150 °C is achieved with a low Mo loading (19 wt% Mo). As the Mo loading increases, the MeOH-derived selectivity decreases (32 wt% and 48 wt% of Mo). Additionally, the difference in product selectivity between the first and second 150 °C runs becomes more pronounced at higher Mo loadings (48 wt% Mo), where the largest increase in MeOH-derived products (during 150 °C in the second run) is observed. This difference becomes smaller as the Mo loading decreases. This shift is expected due to the *in situ* reduction of Mo species that occurred at the high reaction temperature (First temperature sequence at 225 °C), as explained in Chapter 2. Furthermore, the surface environment of Ir was investigated using *operando* DRIFTS. Despite having the same Ir loading, the catalysts showed clear differences in Ir dispersion and in the types and surface coverage of carbonyl species formed. Finally, the DRIFTS analysis of the surface intermediates revealed that increasing the Mo loading selectively suppresses formate species associated with LA sites (types I and II), indicating that these LA sites are blocked by the increased Mo loading, leading to a decrease in formate species of types I and II. In contrast, monodentate formate species remain largely unaffected, as they are not dependent on Lewis acidity. The decrease in formate types I and II is expected to be directly reflected in the catalytic behavior, contributing to the lower MeOH-derived product selectivity observed at 150 °C as the Mo loading increases.

Reference

[1] I.J. Godfrey, A.J. Dent, I.P. Parkin, S. Maenosono, G. Sankar, Structure of gold-silver nanoparticles, Journal of Physical Chemistry C 121 (2017) 1957–1963.

[2] B. Palmer, Do We Exhale Carbon?, Natural Resources Defense Council (2015).

[3] R. Dębek, Novel catalysts for chemical CO_2 utilization, Paris, (2016).

[4] E. Shaftel, H. & Dlugokencky, Carbon Dioxide Measurement, NASA (2022).

[5] Joëlle Mascetti, Carbon Dioxide Coordination Chemistry and Reactivity of Coordinated CO_2, (2010).

[6] K. Larmier, W.C. Liao, S. Tada, E. Lam, R. Verel, A. Bansode, A. Urakawa, A. Comas-Vives, C. Copéret, CO_2-to-Methanol Hydrogenation on Zirconia-Supported Copper Nanoparticles: Reaction Intermediates and the Role of the Metal–Support Interface, Angewandte Chemie - International Edition 56 (2017) 2318–2323.

[7] T. Savaete, Catalytic CO_2 conversion: a techno-economic analysis and theoretical study, (2015).

[8] P. Tian, Y. Wei, M. Ye, Z. Liu, Methanol to olefins (MTO): From fundamentals to commercialization, ACS Catalysis 5 (2015) 1922–1938.

[9] A. Álvarez, A. Bansode, A. Urakawa, A. V. Bavykina, T.A. Wezendonk, M. Makkee, J. Gascon, F. Kapteijn, Challenges in the Greener Production of Formates/Formic Acid, Methanol, and DME by Heterogeneously Catalyzed CO_2 Hydrogenation Processes, Chemical Reviews 117 (2017) 9804–9838.

[10] N. Phongprueksathat, K.W. Ting, S. Mine, Y. Jing, R. Toyoshima, H. Kondoh, K.I. Shimizu, T. Toyao, A. Urakawa, Bifunctionality of Re Supported on TiO_2 in Driving Methanol Formation in Low-Temperature CO_2 Hydrogenation, ACS Catalysis 13 (2023) 10734–10750.

[11] A. Bansode, A. Urakawa, Towards full one-pass conversion of carbon dioxide to methanol and methanol-derived products, Journal of Catalysis 309 (2014) 66–70.

[12] R. Gaikwad, H. Reymond, N. Phongprueksathat, P. Rudolf Von Rohr, A. Urakawa, From CO or CO_2?: Space-resolved insights into high-pressure CO_2 hydrogenation to methanol over $Cu/ZnO/Al_2O_3$, Catalysis Science and Technology 10 (2020) 2763–2768.

[13] A. Álvarez, M. Borges, J.J. Corral-Pérez, J.G. Olcina, L. Hu, D. Cornu, R. Huang, D. Stoian, A. Urakawa, CO_2 Activation over Catalytic Surfaces, ChemPhysChem 18 (2017) 3135–3141.

[14] A. Urakawa, Mind the gaps in CO_2-to-methanol, Nature Catalysis 4 (2021) 447–448.

[15] S. Kar, A. Goeppert, G.K. Surya Prakash, Catalytic Hydrogenation of CO_2 to Methanol: A Review, Catalysts (2021) 89–112.

[16] J.G. van Bennekom, R.H. Venderbosch, J.G.M. Winkelman, E. Wilbers, D. Assink, K.P.J. Lemmens, H.J. Heeres, Methanol synthesis beyond chemical equilibrium, Chemical Engineering Science 87 (2013) 204–208.

[17] J.G. Van Bennekom, J.G.M. Winkelman, R.H. Venderbosch, B. Nieland, H.J. Heeres, Modeling and experimental studies on phase and chemical equilibria in high-pressure methanol synthesis, Industrial and Engineering Chemistry Research 51 (2012) 12233–12243.

[18] R. Kanega, N. Onishi, S. Tanaka, H. Kishimoto, Y. Himeda, Catalytic Hydrogenation of CO_2 to Methanol Using Multinuclear Iridium Complexes in a Gas-Solid Phase Reaction, Journal of the American Chemical Society 143 (2021) 1570–1576.

[19] R. Della Pergola, L. Garlaschelli, F. Demartin, M. Manassero, N. Masciocchi, Chemistry of iridium carbonyl cluster complexes. Synthesis, chemical characterization and solid state structure of the mixed-metal carbonyl cluster $[PPh_4][Ir_6(\mu\text{-}CO)_3(CO)_{12}\{\mu 3\text{-}Cu(NCMe)\}] \cdot CH_2Cl_2$ and its conversion to the dianion $[Ir_{12}(CO)_{26}]^{2-}$, Journal of Organometallic Chemistry 436 (1992) 241–253.

[20] M. Mihaylov, E. Ivanova, F. Thibault-Starzyk, M. Daturi, L. Dimitrov, K. Hadjiivanov, New types of nonclassical iridium carbonyls formed in Ir-ZSM-5: A fourier transform infrared spectroscopy investigation, Journal of Physical Chemistry B 110 (2006) 10383–10389.

[21] H. Weigold, Behavior of $Co\text{-}Mo\text{-}Al_2O_3$ catalysts in the hydrodeoxygenation of phenols*, Fuel (1982).

[22] A. Marafi, A. Hauser, A. Stanislaus, Deactivation patterns of Mo/Al_2O_3, $Ni-Mo/Al_2O_3$ and $Ni-MoP/Al_2O_3$ catalysts in atmospheric residue hydrodesulphurization, Catalysis Today 125 (2007) 192–202.

[23] R. López Cordero, A. López Agudo, Effect of water extraction on the surface properties of Mo/Al_2O_3 and $NiMo/Al_2O_3$ hydrotreating catalysts, Applied Catalysis A: General 202 (2000).

[24] C. Jiménez-González, Z. Boucha, B. De Rivas, J. Delgado, M. Cauqui, J. González-Velasco, J. Gutierrez-Ortiz, R. Lopez-Fonseca, Structural characterization of Ni/alumina reforming catalysts activated at high temperatures, Applied Catalysis A: General (2013).

[25] Y. Rozita, R. Brydson, T.P. Comyn, A.J. Scott, C. Hammond, A. Brown, S. Chauruka, A. Hassanpour, N.P. Young, A.I. Kirkland, H. Sawada, R.I. Smith, A Study of commercial nanoparticulate γ-Al_2O_3 catalyst supports, ChemCatChem 5 (2013) 2695–2706.

[26] F. Klose, T. Wolff, H. Lorenz, A. Seidel-Morgenstern, Y. Suchorski, M. Piórkowska, H. Weiss, Active species on γ-alumina-supported vanadia catalysts: Nature and reducibility, Journal of Catalysis 247 (2007) 176–193.

[27] H. Weigold, The Nature of Molybdenum Oxide Species Mounted on Alumina: An Oligomer Model, (1983).

[28] E. V. Romanova, A. V. Nam, T.S. Kharlamova, Peculiarities of the Active Component Formation in Alumina-Supported Copper Molybdate Catalysts for Soot Combustion, Kinetics and Catalysis 62 (2021) 675–687.

[29] M. Henker, K.P. Wendlandt, J. Valyon, P. Bornmann, Structure of MoO_3/Al_2O_3-SiO_2 catalysts, Applied Catalysis 69 (1991) 205–220.

[30] K. Murugappan, E.M. Anderson, D. Teschner, T.E. Jones, K. Skorupska, Y. Román-Leshkov, Operando NAP-XPS unveils differences in MoO_3 and Mo_2C during hydrodeoxygenation, Nature Catalysis 1 (2018) 960–967.

[31] Y. Zhu, Y. Yao, Z. Luo, C. Pan, J. Yang, Y. Fang, H. Deng, C. Liu, Q. Tan, F. Liu, Y. Guo, Nanostructured MoO3 for efficient energy and environmental catalysis, Molecules 25 (2020) 1–26.

[32] K. Chen, S. Xie, A. Bell, Structure and Properties of Oxidative Dehydrogenation Catalysts Based on MoO_3/Al_2O_3, Journal of Catalysis 198, 232-242 (2001).

[33] Y. Song, Y. Zhao, Z. Huang, J. Zhao, Aqueous synthesis of molybdenum trioxide (h-MoO_3, α-$MoO_3 \cdot H_2O$ and h-/α-MoO_3 composites) and their photochromic properties study, Journal of Alloys and Compounds 693 (2017) 1290–1296.

[34] J. Wu, Z. Chen, X. Xu, P. Wei, G. Xie, X. Zhang, The Growth Process and Photocatalytic Properties of h-MoO_3 and α-MoO_3 under Different Conditions, Crystals 13 (2023).

[35] T. Marzialetti, J.L.G. Fierro, P. Reyes, Effect of the nature of the support on the enantioselective hydrogenation of 1-phenyl-1,2-propanedione over supported iridium catalysts, Journal of the Chilean Chemical Society 50 (2005) 391–399.

[36] A. Samsuri, F. Salleh, T. Shafazila, T. Saharuddin, R. Othaman, Study on the Reduction Behaviour of Nickel Doped Molybdenum Trioxide by Study on the Reduction Behaviour of Nickel Doped Molybdenum Trioxide by Using Carbon Monoxide as Reductant, International Journal of Chemical Engineering and Application (2016).

[37] P. Sun, F. Teng, Z. Yang, X. Yang, S. Zhai, S. Liang, W. Gu, W. Hao, S. Shi, Effect of the phase structure on the catalytic activity of MoO_3 and potential application for indoor clearance, Journal of Materials Chemistry C (2020) 2475–2482.

[38] S. Said, A.A. Abdelrahman, Atomic layer deposition of MoO_3 on mesoporous γ-Al_2O_3 prepared by sol–gel method as efficient catalyst for oxidative desulfurization of refractory dibenzothiophene compound, Journal of Sol-Gel Science and Technology 95 (2020) 308–320.

[39] P. Del Gallo, R. Meunier, C. Pham-Huu, C. Crouzet, M.J. Ledoux, Selective n-Butane Isomerization over High Specific Surface Area MoO_3-Carbon-Modified Catalyst, Industrial and Engineering Chemistry Research (1997).

[40] A. Bansode, B. Tidona, P.R. Von Rohr, A. Urakawa, Impact of K and Ba promoters on CO_2 hydrogenation over Cu/Al_2O_3 catalysts at high pressure, Catalysis Science and Technology 3 (2013) 767–778.

[41] S. Mine, T. Yamaguchi, K.W. Ting, Z. Maeno, S.M.A.H. Siddiki, K. Oshima, S. Satokawa, K.I. Shimizu, T. Toyao, Reverse water-gas shift reaction over $Pt/MoO_x/TiO_2$: reverse Mars-van Krevelen mechanism via redox of supported MoO_x, Catalysis Science and Technology 11 (2021) 4172–4180.

[42] T. Kitano, S. Okazaki, T. Shishido, K. Teramura, T. Tanaka, Journal of Molecular Catalysis A : Chemical Brønsted acid generation of alumina-supported molybdenum oxide calcined at high temperatures : Characterization by acid-catalyzed reactions and spectroscopic methods, “Journal of Molecular Catalysis. A, Chemical” 371 (2013) 21–28.

[43] D. Kubas, J.M. Beck, E. Kasisari, T. Schätzler, A. Becherer, A. Fischer, I. Krossing, From CO_2 to DME: Enhancement through Heteropoly Acids from a Catalyst Screening and Stability Study, ACS Omega 8 (2023) 15203–15216.

[44] A. Akhoondi, A.I. Osman, A. Alizadeh, Direct catalytic production of dimethyl ether from CO and CO_2 : A review Direct catalytic production of dimethyl ether from CO and CO_2 : A review, Synthesis and Sintering 105–120 (2021).

[45] M. Montesa, C. Penneman De Bosscheyde, B.K. Hodnett, F. Delannay, P. Grange, B. Delmon, Influence of Metal-Support Interactions on the Dispersion, Distribution, Reducibility, and Catalytic Activity of Ni/SiO_2 Catalysis, Applied Catalysis (1984).

[46] Russell Howe, An infrared study of a supported Iridium cluster carbonyl complex, Journal of Catalysis (1977).

[47] F. Solymosi, £ Novák, A. Molnár, Infrared Spectroscopic Study on CO-Induced Structural Changes of Iridium on an Alumina Support, (1990).

[48] J. Lu, C. Aydin, N.D. Browning, B.C. Gates, Oxide- and zeolite-supported isostructural $Ir(C_2H_4)_2$ complexes: Molecular-level observations of electronic effects of supports as ligands, Langmuir 28 (2012) 12806–12815.

[49] N. Ishito, K. Hara, K. Nakajima, A. Fukuoka, Selective synthesis of carbon monoxide via formates in reverse water – gas shift reaction over alumina-supported gold catalyst, Journal of Energy Chemistry 25 (2016) 306–310.

[50] X. Liu, R.E. Truitt, DRFT-IR Studies of the Surface of γ -Alumina, American Chemical Society 7863 (1997) 9856–9860.

Appendix

Chapter 3

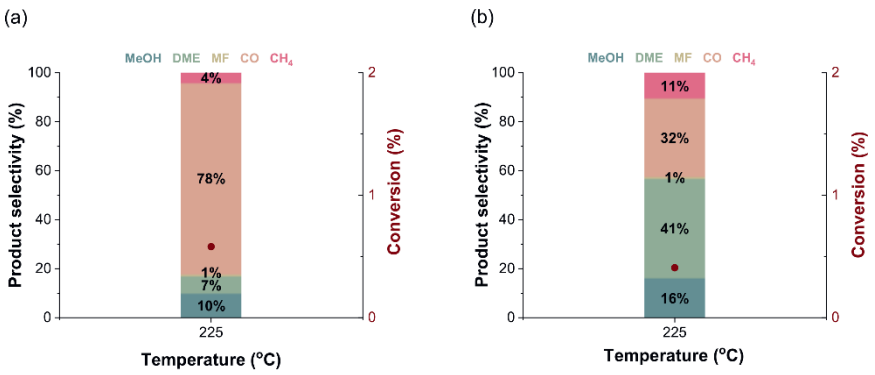


Figure 3.1-S The (1.5)Ir/Al_2O_3 catalytic activity result for CO_2 hydrogenation at 300 bar and 225 °C **(a)** R200 **(b)** R400. The results show the product's selectivity on the left y-axis and the conversion on the right y-axis. The catalyst at 150 and 200 °C shows no activity.

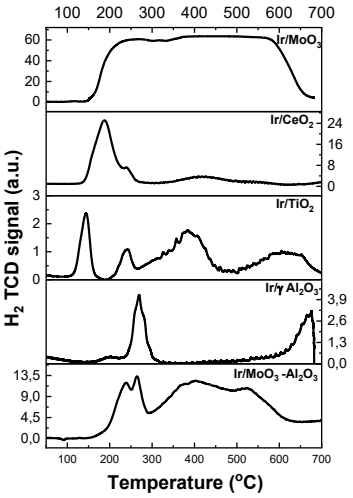


Figure 3.2-S H_2-TPR result for Ir over different supports, the experiments were performed under hydrogen feed, and the temperature was increased from room temperature to 700 °C. The results indicate that Ir species reduction can be started at even below 150 °C, depending on their interaction with the support

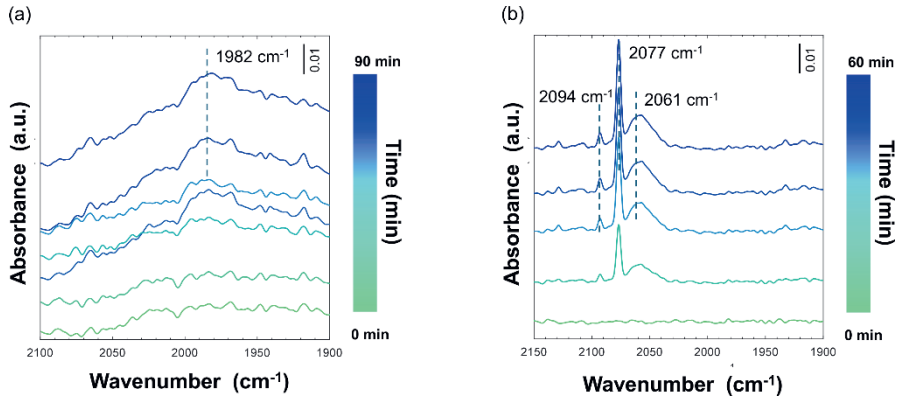


Figure 3.3-S Surface species evolution that was obtained during the *operando* DRIFTS experiment at 150 °C and 10 bar under CO_2 hydrogenation using the R400 reduction protocol. The results shown correspond to the carbonyl region (1900 - 2100 cm^{-1}) of **(a)** (1.5)Ir/Al_2O_3 and **(b)** (1.5)Ir/MoO_3

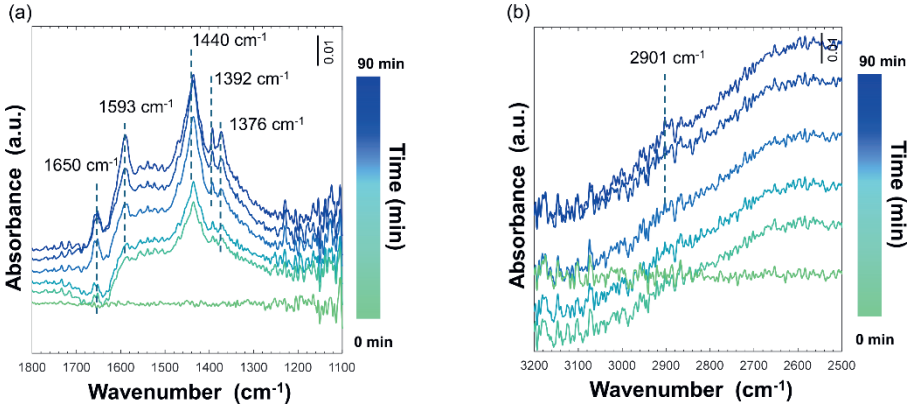


Figure 3.4-S Surface species evolution that was obtained during the *operando* DRIFTS experiment at 150 °C and 10 bar under CO_2 hydrogenation using the R400 reduction protocol. The results shown correspond to the CO_2 hydrogenation over (1.5)Ir/Al_2O_3. **(a)** the C-O region (1100 - 1800 cm^{-1}) of **(b)** the C-H region (2500 - 3200 cm^{-1})

Molybdenum loading calculation:

The calculations below were used to calculate the required quantity of Mo precursor to obtain the desired Al/Mo ratio. These obtained quantities were used during the catalyst synthesis.

Precursor: $(NH_4)_6 Mo_7O_{24}\cdot 4H_2O$

MW = 1235.86 g/mol

Each mole contains 7 Mo atoms.

Mo MW = 95.95 g Mo/mol

So 1 mole produces → 7 mole*95.95 g Mo/mole = 671.65 g Mo

Therefore: 671.65/1235.86 = 0.543

Case 1: Al/Mo = 8

Precursor = 1.30 g

1.30 g of precursor * 0.543 = 0.71 g Mo

Total catalyst mass: 3 (Alumina) + 0.71 (Mo) = 4.06 g

Al/Mo=8, the Mo wt% = (1.06/4.06) *100 = **19%**

Case 2: Al/Mo = 4

Precursor = 2.6 g

2.6 g of precursor * 0.543 = 1.4118 g Mo

Total catalyst mass: 3 (Alumina) + 1.4118 (Mo) = 4.4118 g

Al/Mo=4, the Mo wt% = **32%**

Case 3: Al/Mo = 2

Precursor = 5.2 g

5.2 g of precursor * 0.543 = g Mo

Total catalyst mass: 3 (Alumina) + 2.8236 (Mo) = 5.8236 g

Al/Mo=2, the Mo wt% = **48%**

4 Role of Molybdenum dispersion in enhancing the catalytic performance of Ir/γ-Al_2O_3 for CO_2 hydrogenation to methanol

Ahmad Alrefaei, Atul Bansode, Atsushi Urakawa

The publication is in preparation

Summary

Chapter 3 discussed the effect of molybdenum (Mo) loading on the catalytic activity of iridium/molybdenum/alumina (Ir/*x*Mo/Al_2O_3) catalysts. This study investigates the effect of Mo dispersion on the catalytic performance of Ir/*x*Mo/Al_2O_3 catalysts in CO_2 hydrogenation to methanol (MeOH)-derived products. Two catalysts with identical Mo loading, 32 wt% of Mo, but different Mo dispersions: high (H) and low (L), were synthesized to distinguish the effects of dispersion from composition. Comprehensive characterization using XRD, *operando* DRIFTS, and *in situ* XANES was conducted to correlate structure, chemical state, and activity. The results demonstrate that highly dispersed Mo species significantly modify the surface, leading to a substantial enhancement in MeOH selectivity. Under the high-temperature reduction protocol (R400), (1.5)Ir/(32)Mo/Al_2O_3-H achieved 97% MeOH-derived product selectivity, while (1.5)Ir/(32)Mo/Al_2O_3-L primarily produced CO. *Operando* DRIFTS identified formate type I and monodentate formate species as the key intermediates for MeOH formation. O*perando* XANES revealed that an increase in Mo^{4+} content during the second temperature sequence correlates with a reduction in MeOH selectivity, emphasizing the role of Mo redox behavior in catalytic performance. Overall, this study establishes that Mo dispersion and reduction conditions are critical parameters governing active site formation and product selectivity in CO_2 hydrogenation over Ir/Mo/Al_2O_3 catalysts.

4.1 Introduction

In the previous chapter, the influence of molybdenum (Mo) loading on the catalytic activity of the (1.5)iridium/molybdenum/alumina ((1.5)Ir/*x*Mo/Al_2O_3) in CO_2 hydrogenation was examined. It was observed that the catalyst with the lowest Mo loading, Mo = 19 wt%, exhibited the highest selectivity toward methanol (MeOH)-derived products at 150 °C during the first reaction cycle (Figure 3.3). Additionally, the structural characterization of the supports with varying Mo loading (Figure 3.1) revealed that a low Mo loading (19% of Mo) resulted in highly dispersed Mo species, whereas increasing the Mo loading led to the formation of larger Mo-containing crystallites, as observed with Mo loadings of 32% and 48% (Figure 3.1). This observation raised an important question: Is the higher MeOH-derived product selectivity primarily a result of the low Mo loading or the higher dispersion of Mo species? To address this, two supports with identical Mo loading (32%), but different Mo dispersions were prepared: one with high dispersion (32)Mo/Al_2O_3-H and the other with low dispersion (32)Mo/Al_2O_3-L. The 1.5 wt% of Ir was then impregnated onto both supports using a wet impregnation method.

The catalytic performance of both catalysts was subsequently evaluated in high-pressure CO_2 hydrogenation reactions. Furthermore, as reported in Chapters 2 and 3, the reduction temperature protocol has a significant effect on catalyst performance, specifically the MeOH selectivity. Various reduction protocols were applied to investigate their impact on catalytic activity. A combination of advanced characterization techniques, including *operando* DRIFTS (to monitor the evolution of surface species) and XANES (to analyze the chemical states of Ir and Mo), was employed to gain a deeper understanding of the structure-activity relationship of these catalysts.

4.2 Experimental section

4.2.1 Catalyst synthesis:

The following reagents were used as received. Iridium(III) chloride hydrate (CAS No. 10025-83-9) was purchased from Precious Metals Online. Ammonium molybdate tetrahydrate (CAS No. 12054-85-2) was purchased from Merck Sigma. Finally, the γ-Al_2O_3 (CAS No. 1344-28-1) was purchased from BASF Nederland. The catalysts were prepared using the sequential Wet Impregnation (WI) method with an aqueous solution of the respective metal salt. First, the Mo solution was dissolved in demineralized water. After the Mo

precursor was completely dissolved, γ-Al_2O_3 was added to the solution, and the mixture was stirred at 200 rpm overnight at 50 °C. Consequently, the obtained wet catalyst was dried at 110 °C for 12 h, followed by calcination under air at 500 °C for 3 h. All calculated amounts correspond to (1.5)Ir/(32)Mo/Al_2O_3-L, as mentioned in the experimental section of Chapter 3. For the support Mo-Al_2O_3, which has a high Mo dispersion, the support was purchased from Akzo Nobel. Therefore, two different supports were used; the one with low Mo dispersion was prepared in-house, while the one with high dispersion was purchased.

Iridium (III) chloride hydrate (0.071 g) to obtain a metal loading of 1.5 wt% Ir over each support) was dissolved in 50 mL of deionized water. The amount of metal salt was calculated based on 3 g of support material. After the salt was completely dissolved in the water (0.5 - 0.6 hours), 3 g of the support material was added to the solution. The mixed solution was then stirred at 200 rpm and 50 °C and kept overnight. Subsequently, the drying process was performed in air at 110 °C for 12 h. The obtained powder was crushed and calcined at 500 °C for 3 h, in the air.

4.2.2 Catalysts characterization:

4.2.2.1 H_2-temperature program reduction (H_2-TPR):

200 mg of catalyst was packed inside a quartz tube reactor. H_2 flow was introduced into the reactor, and a heating rate of 10 °C/min was used until reaching a final temperature of 700 °C. The catalysts were heated to 700 °C and held for 10 min. The H_2 signal was recorded online with a thermal conductivity detector (TCD).

4.2.2.2 X-ray diffraction (XRD):

The internal XRD patterns were attained using a Bruker AXS D8 Advance diffractometer. The detector used in the experiment was a Lynxeye-XE-T position-sensitive detector, which enabled efficient and accurate data collection. The recorded data in the range of 5° to 90° was evaluated using the DIFFRAC.EVA software, which provided analysis and interpretation of the diffraction patterns obtained. The diffraction obtained from the XRD at Synchrotron uses a wavelength of 0.53948 Å. Therefore, all the simulated diffraction patterns were obtained using this wavelength. The XRD patterns were attained using a Bruker AXS D8 Advance diffractometer. The detector used in the experiment was a Lynxeye-XE-T position-sensitive detector, which enabled efficient and accurate data collection. The recorded data in the

range of 5° to 90° was evaluated using the DIFFRAC.EVA software, which provided analysis and interpretation of the obtained diffraction patterns.

4.2.3 Catalytic activity

The catalytic activity was evaluated in a custom-made high-pressure setup, as shown in Figure 2.1. In a typical test, a 125 mg catalyst was packed over quartz wool inside a 1/4-inch reactor tube (ID, 2.79 mm. Before loading, the catalysts were pelletized, crushed, and sieved to obtain a particle size range of 90-300 μm. Quartz wool was used to support the catalyst in the reactor. The reduction temperature was changed to 400 °C; however, the same duration and reducing agent were used. After cooling to 35 °C, the $H_2/CO_2/N_2$ mixture (70.5/23.5/6 vol%) was fed into the reactor and pressurized to 300 bar. The space velocity was maintained at 10 NL/(g_{cat} . h). The products were analyzed by an online gas chromatograph (Compact GC 4.0) equipped with a flame ionization detector for the detection of CH_4, MeOH, methyl formate (MF), dimethyl ether (DME), and ethanol (EtOH), and two thermal conductivity detectors, one for the detection of H_2, N_2, CH_4, and CO. This TCD uses Ar as the mobile phase. The second TCD was used to detect CO_2, and He is the mobile phase. The carbon balance was monitored to be within 97 - 102%. The values presented were obtained by averaging the measurements only after steady-state had been reached. A single representative value was then reported for each condition.

$$\mathrm{CO_2\ conversion} = \frac{\mathrm{CO_{2\,in}} - \mathrm{CO_{2\,out}}}{\mathrm{CO_{2\,in}}}\ or\ \frac{\sum \mathrm{n}_{C,i} \times \mathrm{Concentration}_i}{\mathrm{CO_{2\,in}}}$$

$$\mathrm{Selectivity} = \frac{\mathrm{n}_{C,i} \times \mathrm{Concentration}_i}{\sum \mathrm{n}_{C,i} \times \mathrm{Concentration}_i}$$

4.2.4 *Operando* diffuse reflectance infrared fourier transform spectroscopy - mass spectrometry (DRIFTS-MS)

The *operando* DRIFTS was performed utilizing a Thermo Scientific Nicolet 6700 FT-IR and a Pfeiffer OmniStar GSD 300C mass spectrometer (MS), as shown in Figure 2.2. The spectrometer is equipped with a liquid-nitrogen-cooled mercury-cadmium-telluride (MCT) detector to collect the spectra while the MS analyzes the outlet gas stream. Gas flow control in the setup was facilitated by six Bronkhorst mass flow controllers, which regulated the flow

rates of H_2, CO_2, and He. Switching between the two reactant gas streams was achieved using a 4-way valve. Back- pressure regulators (Bronkhorst) were employed to control the pressure of the reaction cell and the vent side, maintaining the desired pressures within the system. A 40-50 mg of catalyst powder was placed inside a cylindrical cavity, having a diameter of 3 mm and a vertical length of 3 mm, located in a Harrick Praying Mantis DRIFTS accessory. Before the measurements, the catalyst was reduced at the desired temperature using a mixture of H_2 and He gases (90/10) for 1.5 hours. Subsequently, the sample was cooled to the reaction temperature of 75 °C and pressurized to 10 bar under a He stream. The reaction cell was exposed to CO_2:H_2 feed with a composition of 1:3 (total flow of 15 mL/min). The spectra were acquired at a resolution of 4 cm^{-1}. 10 spectra were averaged and collected after 13.3 s.

4.2.5 Synchrotron experiments

The experiments were performed at ALBA, BL16-NOTOS beamline. Prior to the experiment, the catalyst was diluted in boron nitrate (BN) with a ratio of 1:10. A 10 cm-long capillary with an inner diameter of 1 mm and a wall thickness of 10 μm was prepared. The central 0.5 cm of the capillary was loaded with the diluted catalyst sample. To facilitate gas heating, the sample was fixed with 1 cm of silicon carbide (SiC) at the outlet and 2 cm at the inlet. Quartz wool was used at both ends to fixate the bed. The capillary was mounted in a U-shaped cell that allowed either direct gas flow through the capillary or in bypass mode. Subsequently, the bed was heated with a hot blower, whose position was calibrated to the middle of the bed, with roughly 5 cm spacing between the blower and the bed to ensure that the blower and catalyst temperatures are linearly related up to 600 °C. The XANES spectra were taken sequentially at the Ir L_3-edge (11215 eV) and Mo K-edge (20000 eV). Spectral acquisition times were approximately 3 minutes for XANES, and 2 minutes for Synchrotron X-ray Diffraction (XRD) measurements. Both edges were measured in fluorescence mode using a 13-element Si detector. In the experiment, a (1.5)Ir/(32)Mo/Al_2O_3-H catalyst was reduced *in situ* under a 5 mL/min H_2 flow with a ramp rate of 10 °C/min. Afterward, the temperature was maintained at 200 °C for 60 minutes. The XRD measurements were obtained at this temperature. After the measurement ended, the reduction temperature was gradually increased at the same ramping rate to 400°C. After collecting the required measurements, the reaction mixture was switched to a 1:3 CO_2:H_2 ratio (10 mL/min) and the capillary was pressurized to 20 bar. Then, the temperature was increased to 75, 225, and 75 ^oC. XANES

spectra were collected during the temperature ramping, while XRD was collected after each step.

4.3 Results and discussion

4.3.1 The structural investigation of (1.5)Ir/(32)Mo/Al_2O_3 with different Mo dispersion

The structures of the supports with the same Mo loading but different Mo dispersion before and after Ir impregnation were investigated by XRD to further confirm the differences in Mo dispersion. The XRD patterns of both prepared catalysts: the catalyst with low Mo dispersion (1.5)Ir/(32)Mo/Al_2O_3-L and the catalyst with high dispersion (1.5)Ir/(32)Mo/Al_2O_3-H, along with the supports, are shown in Figure 4.1: The diffraction of the support (32)Mo/Al_2O_3-L was explained in detail in Chapter 3, Section 2.1. Briefly, the diffraction patterns indicate the presence of multiple Mo species, including alumina molybdate and α-MoO_3. After Ir impregnation, the diffraction corresponding to the Mo species disappeared, while the IrO_2 diffraction evolved. This result suggests that the Ir impregnation might lead to distorting the Mo crystalline structure , resulting in the absence of Mo-related diffractions in the XRD. A similar effect was observed with different metals, indicating a significant impact of metal doping on the Mo crystalline structure [1–3]. On the other hand, the diffraction of (32)Mo/Al_2O_3-H support shows the characteristic diffraction peak of only γ-Al_2O_3, while no diffraction peak of Mo species was observed, indicating a well-dispersed Mo species or present as very small Mo-containing crystallites below the detection limit of the XRD instrument. Upon Ir impregnation, IrO_2 diffractions were detected, and no change in the support structure was observed. A comparison of the IrO_2 diffractions between the two catalysts, (1.5)Ir/(32)Mo/Al_2O_3-L and (1.5)Ir/(32)Mo/Al_2O_3-H, shows that the IrO_2 diffraction over (H) is sharper and more intense than (L), suggesting the formation of large Ir crystallites when the Mo species is well-dispersed or the Mo-containing crystallites are small. This result was also observed during the structural investigation of (1.5)Ir/(19)Mo/Al_2O_3 in Chapter 3 (Figure 3.2 (a)), where (1.5)Ir/(19)Mo/Al_2O_3 showed a high Mo dispersion and resulted in the highest intensity reflection of IrO_2 among other Mo loadings. In conclusion, the XRD results indicate that a more dispersed Mo species leads to the formation of larger IrO_2 crystallites, which is are more easily reduced, and might lead to faster reduction of Mo species.

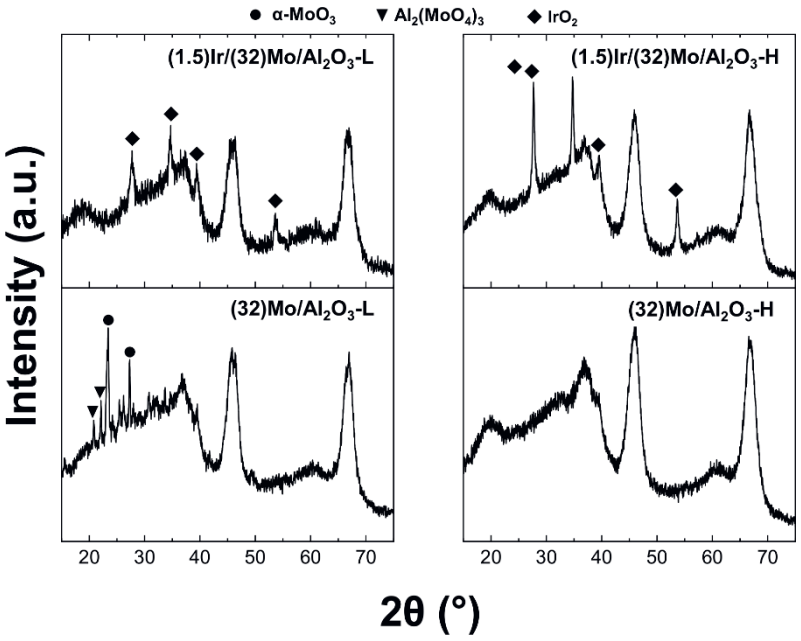


Figure 4.1 The X-ray diffraction of the bare supports before Ir impregnation, the low Mo dispersion ((32)Mo/Al_2O_3-L), and the high Mo dispersion ((32)Mo/Al_2O_3-H) are shown on the bottom side of the figure. The diffractions of the catalysts after Ir impregnation, (1.5)Ir/(32)Mo/Al_2O_3-L and (1.5)Ir/(32)Mo/Al_2O_3-H are shown on the top. The result indicates the formation of large IrO_2 crystallites when Mo is well-dispersed. This result is consistent with the previous one (Chapter 3), where (1.5)Ir/(19)Mo/Al_2O_3, with high Mo dispersion, resulted in the formation of large IrO_2 crystallites.

4.3.2 The catalytic activity performance of different Mo dispersions

The catalytic performance of (1.5)Ir/(32)Mo/Al_2O_3-L and -H catalysts was investigated at 150 °C and 300 bar to examine the effect of Mo dispersion. The conversion of CO_2 and product selectivity are compared in Figure 4.2. Initially, the reduction was conducted at 200 °C for 1.5 h (R200). At this temperature, the Mo species are not expected to be significantly reduced, allowing a comparison between the two systems without accounting for Mo reduction. The catalytic results obtained with the R200 protocol are shown in Figure 4.2(a). As observed, both catalysts exhibited 74% selectivity toward CH_4. However, the MeOH-derived product selectivity of (1.5)Ir/(32)Mo/Al_2O_3-H (24%) is twice the MeOH-derived product selectivity of (1.5)Ir/(32)Mo/Al_2O_3-

L (12%). This suggests that differences in surface properties, even before a major Mo reduction, may be attributed to different Ir environments in the two systems. To summarize, the catalytic activity under the R200 protocol resulted in high CH_4 selectivity in both systems.

Subsequently, the reduction temperature was increased to 400 °C for 1.5 h (R400), where Mo species are expected to undergo reduction, as indicated by the H_2-TPR profile of both systems (1.5)Ir/(32)Mo/Al_2O_3-H and (1.5)Ir/(32)Mo/Al_2O_3-L, as shown in Figure 4.1-S (Appendix). The catalytic performance of the two systems, along with that of (1.5)Ir/MoO_3, is shown in Figure 4.2 (b). The catalytic activity result of (1.5)Ir/MoO_3 was added for comparison and to investigate the possible effect of Mo dispersion on Al_2O_3. Upon applying the R400 protocol, the (1.5)Ir/(32)Mo/Al_2O_3-L catalyst exhibited a significant suppression of CH_4 formation (down to ~10%), accompanied by increased CO selectivity (53%), while MeOH-derived product selectivity is 39%, nearly more than double compared to when the R200 protocol was applied. This product selectivity closely resembles that of the Ir/MoO_3 system, suggesting similar active site characteristics that lead to a similar reaction pathway. This similar product selectivity suggests that, during the preparation of (1.5)Ir/(32)Mo/Al_2O_3-L, Ir was predominantly deposited over Mo species, forming a distinct Ir-Mo phase dispersed on the alumina support (most likely Ir/MoO_x). However, the CO_2 conversion of (1.5)Ir/(32)Mo/Al_2O_3-L was observed to be five times lower than Ir/MoO_3. To investigate the difference in conversion between the two systems, the H_2-TPR for both (1.5)Ir/(32)Mo/Al_2O_3-L and Ir/MoO_3 was compared, and the H_2-TPR profiles of the two systems are shown in Figure 4.2-S, Appendix. The total hydrogen consumption of Ir/MoO_3 was calculated to be 3.71 mmol. However, over (1.5)Ir/(32)Mo/Al_2O_3-L, hydrogen consumption was calculated to be 0.087 mmol. The higher hydrogen consumption of Ir/MoO_3 during H_2-TPR, compared to (1.5)Ir/(32)Mo/Al2O3-L, indicates greater hydrogenation activity of Ir/MoO_3, leading to faster CO_2 activation (higher conversion).

In contrast, the (1.5)Ir/(32)Mo/Al_2O_3-H exhibited entirely different behavior under the same conditions, with the complete suppression of CH_4 and CO formation, yielding exclusively MeOH-derived products, about 97%. This result suggests that Ir impregnation on a well-dispersed Mo/Al_2O_3 support likely facilitates the formation of selective intermediates that favor the formation of MeOH.

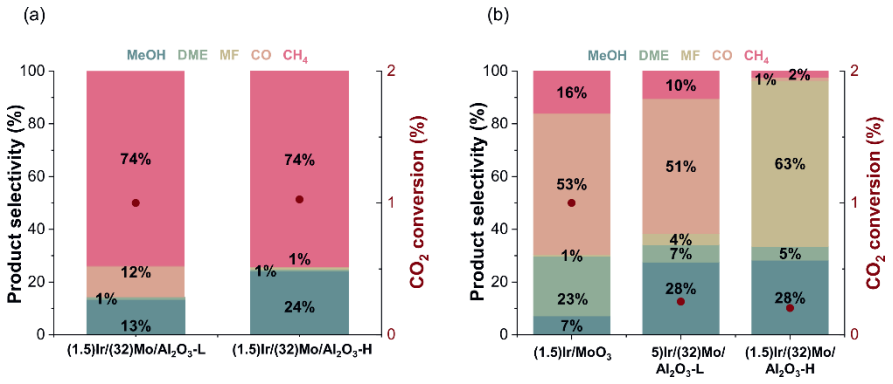


Figure 4.2 The comparison of CO_2 conversion and product selectivity of (1.5)Ir/(32)Mo/Al_2O_3-L vs (1.5)Ir/(32)Mo/Al_2O_3-H at 300 bar and 150 °C using **(a)** the R200, and **(b)** the R400 reduction protocol, with adding the activity performance of (1.5)Ir/MoO_3 (R400) for comparison. The R200 result shows similar product activity and selectivity between the two catalysts, except for MeOH, which exhibited double selectivity in (1.5)Ir/(32)Mo/Al_2O_3-H. Changing the reduction protocol to R400 led to significant differences between the two catalysts

4.3.3 Effect of a second temperature sequence on the catalytic activity

For all Mo-containing catalysts, performing a second temperature sequence resulted in a noticeable change in catalytic activity. To further investigate this behavior in Mo-dispersion catalysts, the same experimental protocol was applied to both catalysts, (1.5)Ir/(32)Mo/Al_2O_3-H and (1.5)Ir/(32)Mo/Al_2O_3-L. The procedure began with catalyst reduction using the R400 reduction protocol, followed by pressurization to 300 bar under a CO_2/H_2 (1:3) feed mixture. The reaction temperature was sequentially increased to 150 °C, 175 °C, and 225 °C, then cooled back to 150 °C. The catalytic performance of (1.5)Ir/(32)Mo/Al_2O_3-L is shown in Figure 3.3 (b), while that of (1.5)Ir/(32)Mo/Al_2O_3-H is presented in Figure 4.3 (a).

For the (1.5)Ir/(32)Mo/Al_2O_3-L catalyst, CO was the dominant product at all tested temperatures (150, 175, and 225 °C). However, upon cooling the reaction back to 150 °C, the selectivity toward the MeOH-derived product increased substantially to 65%. In contrast, (1.5)Ir/(32)Mo/Al_2O_3-H displayed a different trend, as illustrated in Figure 4.3 (a). At 150 °C, the catalyst exhibited 97% selectivity for MeOH-derived products. As the temperature increased, the RWGS reaction became dominant, resulting in higher CO selectivity. Interestingly, when the temperature was decreased back to 150 °C, the selectivity for the MeOH-derived product dropped from 97% in the first

sequence to 61% in the second sequence, suggesting a negative effect of the second temperature sequence. This behavior was not observed in any of the other catalytic systems. For the CO_2 conversion, a slight increase was observed in the second temperature sequence for both catalysts, indicating that the Mo dispersion has a negligible effect on CO_2 conversion. It is worth mentioning that over (1.5)Ir/(19)Mo/Al_2O_3, which has a well-dispersed Mo species, the increase in the selectivity of MeOH-derived product in the second temperature sequence was negligible compared to other Mo loadings. This result suggests a possible correlation between the dispersion of Mo species and the change in selectivity in the second temperature sequence. In our previous investigation (Chapter 2), the increase in MeOH-derived product selectivity in the second temperature sequence was attributed mainly to a change in the Mo chemical state, with a more reduced state in the second sequence (Figure 2.17-S). Therefore, it is highly expected that the Mo chemical state in (1.5)Ir/(32)Mo/Al_2O_3-H during the second temperature sequence would exhibit different behavior.

To further explore this negative change in the MeOH-derived product selectivity of (1.5)Ir/(32)Mo/Al_2O_3-H in the second temperature sequence, the Mo chemical state was investigated through *operando* XANES. During the experiment, the catalyst was first reduced using the R400 reduction protocol. Following the reduction, the system was pressurized to 20 bar under a helium atmosphere. The temperature was then increased to 75 °C, after which the feed was switched from helium to a CO_2/H_2 (1:3) mixture. The reaction temperature was subsequently increased to 225 °C and then cooled back down to 75 °C. Throughout these steps, the Ir L_3-edge and Mo K-edge were monitored to detect potential changes in their chemical states. The Ir L_3-edge and Mo K-edge are shown in Figures 4.7, 8, and 9-S (Appendix). For the Ir L_3-edge, no change in the chemical state of Ir was observed at all temperatures. However, a slight change in the Mo chemical state was observed. To gain more insight into that change, the Mo^{4+} content was analyzed at each reaction temperature using linear combination fitting (LCF). The Mo^{4+} content over time at all tested temperatures is shown in Figure 4.3 (b). At 75 °C, the average Mo^{4+} content was 64%. After increasing the reaction temperature to 225 °C, the average Mo^{+4} content decreased to 61%. After cooling the reaction temperature back to 75 °C, the average Mo^{4+} content increased to 68%, indicating a shift toward a higher oxidation state. Contrary to the behavior observed for Ir/MoO_3 in Chapter 2, where a more reduced Mo state during the second temperature sequence enhanced MeOH-derived product selectivity, the (1.5)Ir/(32)Mo/Al_2O_3-H catalyst showed the opposite

trend. In this case, an increase in Mo^{4+} content during the second temperature sequence was observed and accompanied by a decrease in the selectivity of the MeOH-derived product. This result suggests that the increase in Mo^{4+} content observed in the second temperature sequence is the primary reason for the negative impact on the selectivity of the MeOH-derived product during this sequence (Figure 4.3 (a)).

Additionally, to further investigate this change in the Mo chemical state, *operando* XRD was performed for (1.5)Ir/(32)Mo/Al_2O_3-H at all tested reaction temperatures. The XRD patterns are shown in Figure 4.3 (c). The peak, positioned at 12.72°, appeared after the reduction was completed. This peak was present at 75 °C. After increasing the reaction temperature to 225 °C, the peak became broad. In the second temperature sequence at 75 °C, a peak appeared with a slight increase in intensity (compared to the observation at 225 °C) and a slight shift to a higher angle of 12.8° (compared to the first 75 °C). To explore this shift in the peak position, MoO_2 and Mo^0 were used as references for further verification. The peak at 12.72° indicates the formation of the Mo^0 phase (Figure 4.3 (c)). At a reaction temperature of 75 °C, no significant change in the Mo chemical state is expected, as this low temperature is not expected to cause any change. This led to no noticeable change in the diffraction pattern during the first 75 °C run. As the reaction temperature increased to 225 °C under a CO_2/H_2 feed, the formation of the Mo^{4+} phase was observed, as evidenced by the broadening of the peak located between 12.72° and 12.8°. When the reaction temperature cooled to 75 °C (second run), the peak shifted to 12.8°, indicating the formation of Mo^{4+}. This finding suggests that the Mo species shifts toward a higher oxidation state (Mo^{4+}), which correlates with increased CO selectivity. The transition from Mo^0 to Mo^{4+} in the (1.5)Ir/(32)Mo/Al_2O_3-H catalyst can be attributed to the oxidative-reductive CO_2/H_2 reaction environment. Under these conditions, CO_2 acts as a mild oxidant, while H_2 serves as a reductant, creating a dynamic redox balance that governs the chemical state of Mo. The observed stabilization of Mo^{4+} is likely due to this redox interplay, further influenced by strong metal-support interactions that modify the reduction behavior of Mo species. This result is also consistent with the *operando* XANES result, which shows that more Mo^{4+} was measured in the second temperature sequence. In contrast to Ir/MoO_3 in the second temperature sequence, where in situ reduction was observed, this behavior was not observed over (1.5)Ir/(32)Mo/Al_2O_3-H, likely due to the strong metal-support interaction, as explained previously. Hence, a higher content of Mo^{4+} was measured in the

second temperature sequence, which is expected to shift the product selectivity from high MeOH-derived product to high CO.

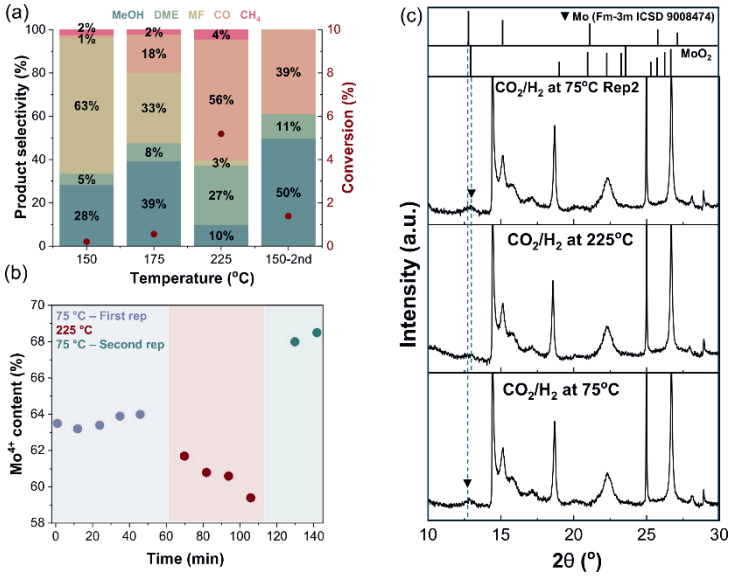


Figure 4.3 (a) The catalytic activity result of CO_2 hydrogenation over (1.5)Ir/(32)Mo/Al_2O_3-H performed at 300 bar and three different temperatures (150, 175, and 225 °C) followed by cooling down again to 150 °C using the R400 reduction protocol. The results indicate a negative impact on product selectivity when a second temperature sequence was implemented, as observed in the 150-2nd result. **(b)** The Mo^{4+} content during the CO_2 hydrogenation over (1.5)Ir/(32)Mo/Al_2O_3-H. The results obtained from applying LCF on the *operando* XANES experiment, performed at 20 bar and three different temperatures. The results show an increase in Mo oxidation state in the second implemented 75 °C. **(c)** *Operando* XRD, which was conducted during CO_2 hydrogenation for (1.5)Ir/(32)Mo/Al_2O_3-H at 10 bar, and three different temperatures.

4.3.4 Effect on the surface species environment with different Mo dispersion

To provide insight into the surface species environment during CO_2 hydrogenation, *operando* DRIFTS was performed on the catalysts (1.5)Ir/(32)Mo/Al_2O_3-L and -H. During the experiment, the catalysts were reduced using the R400 reduction protocol (400 °C for 1.5 h). The catalysts were then cooled to 150 °C and pressurized to 10 bar with He, followed by the introduction of the feed (H_2/CO_2 = 3). The collected spectra were analyzed in different regions, *v*(C-O) region (1000 - 1800 cm^{-1}), *v*(Carbonyl) region (1900 - 2100 cm^{-1}) and *v*(C-H) region (2500 - 3200 cm^{-1}). Figure 4.4 shows

the evolution of the surface species in the *v*(C-O) vibration region (1000 - 1800 cm^{-1}) with time for both catalysts (a) (1.5)Ir/(32)Mo/Al_2O_3-L and (b) (1.5)Ir/(32)Mo/Al_2O_3-H. The spectra of (1.5)Ir/(32)Mo/Al_2O_3-L reveal two broad bands: the first, positioned between 1300 and 1400 cm^{-1}, and the second, between 1550 and 1700 cm^{-1}. Another small band was observed at 1453 cm^{-1}. The analysis of the spectra of these surface species is described in Section 2.6 of Chapter 3. In brief, the spectra indicate that the bands at 1392 and 1593 cm^{-1} correspond to the presence of formate species (type I, formate adsorbed on two Lewis acid (LA) sites) over Al_2O_3 [4–7]. The band at 1367 and 1648 cm^{-1} corresponds to formate species (type II, adsorption adjacent to LA sites) [6]. Additionally, the band at 1319 cm^{-1} is most likely the monodentate formate [6]. The band at 1616 cm^{-1} was not observed due to the overlap with other bands in the same region. Finally, the band at 1453 cm^{-1} corresponds to the symmetrical vibration of bicarbonate over Al_2O_3, while its asymmetrical vibration is expected within the broad band between 1550 - 1700 cm^{-1}.

The spectra for the *v*(C-O) region of (1.5)Ir/(32)Mo/Al_2O_3-H, shown in Figure 4.4 (b), exhibited a large broad band between 1500 and 1700 cm^{-1}, which is an overlap of different bands: at 1640, 1612, and 1588 cm^{-1}. Another three bands were observed over 1453, 1392, and 1324 cm^{-1}. The spectra analysis reveals the existence of formate type I via the bands at 1392 and 1588 cm^{-1} and the monodentate formate via the bands at 1319 and 1646 cm^{-1}. The absence of a band at 1367 cm^{-1} indicates that formate type II was not formed. To confirm the presence of formate type I and the absence of formate type II, the C-H stretching region was analyzed. The results are shown in Figure 4.5-S (Appendix). (1.5)Ir/(32)Mo/Al_2O_3-H exhibited a clear band at 2907 cm^{-1} corresponds to the C-H vibration of formate type I; however, the band at 2845 cm^{-1} was only observed in (1.5)Ir/(32)Mo/Al_2O_3-L and not in in (1.5)Ir/(32)Mo/Al_2O_3-H, shows the absence of formate type II over (1.5)Ir/(32)Mo/Al_2O_3-H. This band at 2845 cm^{-1} was assigned to the C-H stretching vibration of formate type II (Section 2.6, Chapter 3). Additionally, the shoulder feature, which was identified in Section 2.5, Chapter 3 as the C-H stretching vibration of the monodentate formate, was also observed in (1.5)Ir/(32)Mo/Al_2O_3-H, as shown in Figure 4.5-S (b), Appendix. This result suggests that the presence of well-dispersed Mo species modifies the surface chemistry, leading to a higher coverage of formate species type I and, consequently, higher selectivity for MeOH-derived products. Furthermore, the band at 1453 and 1612 cm^{-1} corresponds mainly to bicarbonate, similar to what was observed over (1.5)Ir/(32)Mo/Al_2O_3-L. In summary, the formate

species type I, which binds to the surface via two LA sites, and the monodentate formate were identified as the key intermediates for higher MeOH-derived products. However, since formate type II was not observed over (1.5)Ir/(32)Mo/Al_2O_3-H, it is expected that this formate (type II) is not directly related to the formation of MeOH-derived product.

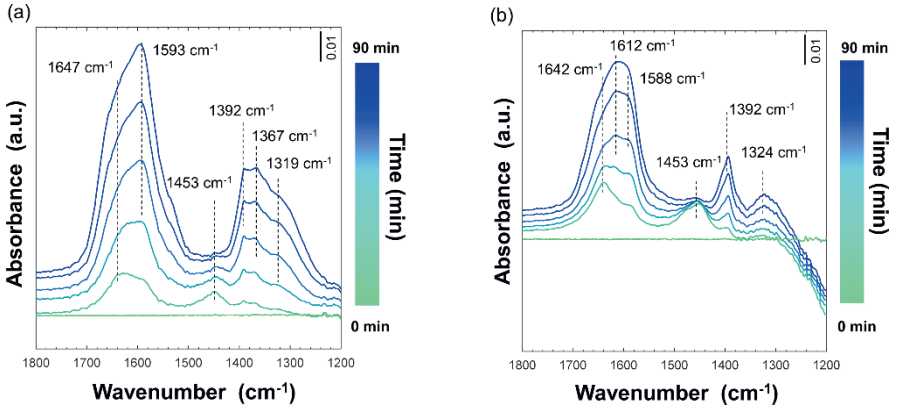


Figure 4.4 Temporal evolution of surface species obtained from *operando* DRIFTS during CO_2 hydrogenation at 150 °C and 10 bar over **(a)** (1.5)Ir/(32)Mo/Al_2O_3-L and **(b)** (1.5)Ir/(32)Mo/Al_2O_3-H. The result here shows the C-O vibration region (1200-1800 cm^{-1}), indicating a significant difference in the surface species environment between the two catalysts.

4.3.5 Effect of the Ir state over (1.5)Ir/(32)Mo/Al_2O_3-L and -H

To further investigate the differences between the two systems, (1.5)Ir/(32)Mo/Al_2O_3-L and -H, the carbonyl region (1900 - 2100 cm^{-1}) was analyzed, and the spectra for both catalysts are shown in Figure 4.5. For the (1.5)Ir/(32)Mo/Al_2O_3-L (Figure 4.5 (a)), the spectra show mainly four distinct bands with different shapes. The band at 2077 cm^{-1} was sharp, indicating a well-defined vibration mode of linear Ir-carbonyl species [8–10]. The other three bands were observed at 2008, 2060, and 2094 cm^{-1}, corresponding to the vibrations of bridged carbonyl and dicarbonyl species over Ir (v-s and v-as, respectively) [8–11]. For the (1.5)Ir/(32)Mo/Al_2O_3-H (Figure 4.5 (b)), the spectra show three distinct bands at 2064, 2077, and 2094 cm^{-1}. The band at 2077 cm^{-1} corresponds to linear Ir-carbonyl. The other two bands (2064 and 2094 cm^{-1}) are assigned mainly to dicarbonyl species over Ir (*v*-s and *v*-as).

Two findings were obtained from this investigation: first, the peak-to-peak ratio between 2077 and 2064 cm^{-1} indicates that the 2077 cm^{-1} band in (1.5)Ir/(32)Mo/Al_2O_3-H is noticeably broader and less intense than that in (1.5)Ir/(32)Mo/Al_2O_3-L. Additionally, the band at 2008 cm^{-1}, which is observed over (1.5)Ir/(32)Mo/Al_2O_3-L, was not observed over (1.5)Ir/(32)Mo/Al_2O_3-H, and since this band is assigned to bridged carbonyl [11]. Then, the Ir-bridged carbonyl is unlikely to be present on (1.5)Ir/(32)Mo/Al_2O_3-H. This indicates a more dispersed Ir over (1.5)Ir/(32)Mo/Al_2O_3-H than over (1.5)Ir/(32)Mo/Al_2O_3-L.

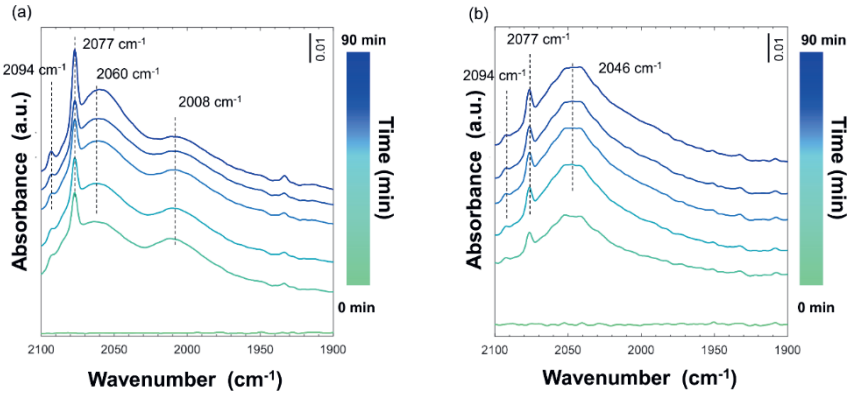


Figure 4.5 Temporal evolution of surface species obtained from *operando* DRIFTS during CO_2 hydrogenation at 150 °C and 10 bar over **(a)** (1.5)Ir/(32)Mo/Al_2O_3-L and **(b)** (1.5)Ir/(32)Mo/Al_2O_3-H. The result shows the carbonyl vibration region (1900-2100 cm^{-1}), indicating differences in the peak-to-peak ratio between the two catalysts.

4.3.6 The effect of the reduction protocol on the catalytic performance of (1.5)Ir/(32)Mo/Al_2O_3-H

To assess the effect of the reduction protocol on catalytic performance, two reduction procedures were compared: one at 200 °C for 1.5 h (R200) and another at 400 °C for 1.5 h (R400). The catalyst (1.5)Ir/(32)Mo/Al_2O_3-H was chosen for this study because it exhibited high selectivity toward MeOH-derived products when reduced using the R400 protocol in the first temperature sequence. Catalytic testing was carried out for CO_2 hydrogenation at 150 °C and 300 bar. The conversion of CO_2 and product selectivity at different reduction protocols is shown in Figure 4.6. A notable difference in the conversion was also observed. The CO_2 conversion achieved after R200 reduction was approximately four times higher than that obtained after R400 reduction. This significant increase in conversion indicates the potential for more accessible Ir sites, leading to a faster

hydrogenation reaction. The faster hydrogenation reaction was confirmed by observing the product selectivity when R200 was applied, where CH_4 was the dominant product, with a selectivity of 74%, as shown in Figure 4.6.

Regarding product selectivity, the graph clearly demonstrates the strong influence of the reduction protocol. After R200, 74% CH_4 selectivity was observed, as reported previously, while the remaining selectivity (26%) corresponds to MeOH-derived products. In contrast, reduction under the R400 protocol drastically shifted the selectivity toward MeOH-derived products, achieving 97% selectivity. The substantial shift in product distribution also suggests that significant structural or chemical changes occur during the reduction step. To further understand these changes, *in situ* XANES and *operando* DRIFTS measurements were performed to characterize the catalyst state following each reduction protocol.

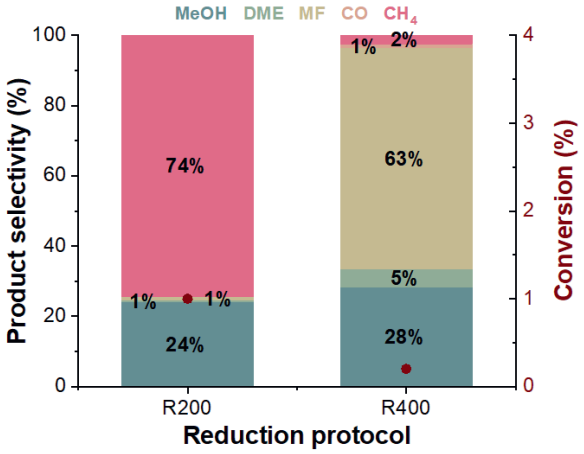


Figure 4.6 The CO_2 conversion and product selectivity of the (1.5)Ir/(32)Mo/Al_2O_3-H during CO_2 hydrogenation at 300 bar and 150 °C using the two selected reduction protocols, 200 °C for 90 min (R200) and 400 °C for 90 min (R400). The results show the increase in MeOH-derived product selectivity when the R400 was implemented.

4.3.6.1 The investigation of the chemical state of the catalyst during each reduction protocol

To explore the catalyst's chemical state, *in situ* XANES was performed during reduction. Hydrogen was fed under conditions similar to those used during catalytic performance testing. The reduction temperature was

increased gradually to 200 °C. After reaching the desired temperature of 200 °C, XANES spectra of Ir L_3-edge and Mo K-edge were obtained. Following completion of this step, the temperature was increased to 400 °C, and measurements of the Ir L_3-edge and Mo K-edge were obtained again. The Ir L_3-edge and the Mo K-edge measured for the fresh catalyst at room temperature (RT), after reaching 200 °C (R200), and after reaching 400 °C (R400) are shown in Figure 4.7.

The Ir L_3-edge shown in Figure 4.7 (a) shows that the Ir chemical state experienced a significant change from Ir^{4+} and Ir $^{3+}$ to almost metallic Ir^0 when the reduction temperature reached 200 °C. The progressive measurement obtained during the temperature ramping indicates that the change in Ir chemical began at ~150 °C. Following the reduction at 200 °C, the temperature was increased further to 400 °C. Negligible spectral changes were observed, confirming that the Ir state was nearly fully metallic at 200 °C.

The Mo K-edge was analyzed for the fresh catalyst at room temperature (RT), and the results are shown in Figure 4.7 (b). The Mo K-edge of (1.5)Ir/(32)Mo/Al_2O_3-H was compared with the Mo K-edge of the reference crystalline MoO_3. The linear combination fitting (LCF) confirmed that the Mo oxidation state is predominantly +6. However, in the post-edge region, changes in the spectra were observed, indicating a difference in the local coordination environment. This is consistent with the XRD data (Figure 4.1, (1.5)Ir/(32)Mo/Al_2O_3-H), which showed no diffraction peaks corresponding to crystalline MoO_3, confirming that the Mo species is amorphous.

As the temperature increased to 200 °C, a slight change was observed in the Mo K-edge results, as shown in Figure 4.7 (c). The LCF indicates that the Mo oxidation state remains dominant at +6, which shows a 95.7% match to MoO_3. The remaining 4.3% of Mo species indicate the presence of both Mo^0 and Mo^{4+}. When the temperature increased to 400 °C (R400), the pre-edge feature changed in the Mo K-edge, as shown in Figure 4.7 (d), indicating a change in the Mo coordination environment. Additionally, the LCF shows Mo^{6+} content of 15.5%, Mo^{4+} of 53.5%, and Mo^0 of 31%, indicating a significant change in the Mo chemical state when the R400 reduction protocol is applied. In summary, *in situ* XANES analysis was performed to monitor the chemical states of Ir and Mo during the R200 and R400 reduction protocols, which corresponded to the observed changes in catalytic performance. The results indicate that the oxidation state of Ir changed to metallic after R200 reduction and remains mainly unaffected by the reduction temperature. In contrast, the Mo species undergoes a significant chemical change. This major change in

the Mo chemical state is proposed as the primary factor responsible for the shift in catalytic performance between the two protocols.

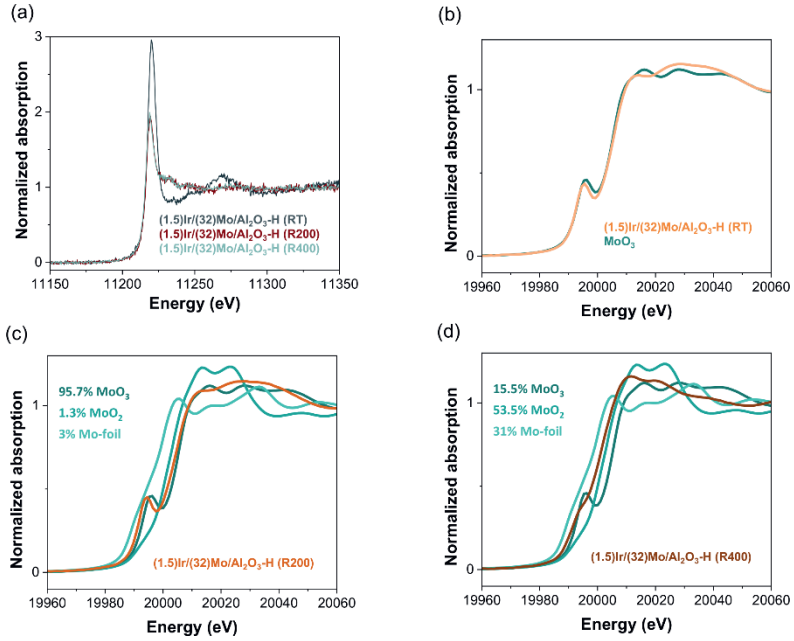


Figure 4.7 *In situ* XANES results, obtained from (1.5)Ir/(32)Mo/Al_2O_3-H during the reduction using the R200 and R400 under a hydrogen environment, **(a)** the Ir L_3-edge measured for the fresh sample, R200, and R400. The Mo K-edge for the catalyst at **(b)** room temperature (RT) with the reference MoO_3, **(c)** after implementing the R200 reduction protocol (200 °C for 1.5 h) alongside other references, and **(d)** after implementing the R400 reduction protocol (400 °C for 1.5 h) alongside other references.

4.3.6.2 The structural change during each reduction protocol

To investigate the structural changes under different reduction protocols, *in situ* XRD measurements were performed on the fresh catalyst at RT, after the R200 and R400 reduction protocols. The resulting diffraction, along with the references for computed Mo^0, MoO_2, γ-Al_2O_3, and orthorhombic MoO_3, is shown in Figure 4.8. The XRD data for (1.5)Ir/(32)Mo/Al_2O_3-H at room temperature (RT) shows four identified and five unidentified reflections. The unidentified reflections at 14.8°, 15°, 18.5°, 25°, and 27° correspond to boron nitride (BN), which was used to dilute the catalyst during the XRD measurements. The identified reflections at 12.1°, 16°, 18.3°, and 22.5° are attributed to α-MoO_3 (12.1° and 18.3°) and γ-Al_2O_3 (16° and 22.5°). The small

diffraction peaks observed in the Mo-related component confirm the presence of very small crystallites of the Mo-related component (which was not detected in the previous XRD equipment, Figure 3.1). Upon heating to 200 °C in R200, no major change in the diffraction was observed, as shown in Figure 4.8 (R200). This result is consistent with our *in situ* XANES observations, which showed no major change in the Mo chemical state (Figure 4.7(c)). With a further increase in the reduction temperature to 400 °C, the reflections at 12.1° and 18.3° disappeared, and a broad reflection emerged at 12.72°, indicative of the presence of Mo^0 (Figure 4.8, R400). This result indicates that the α-MoO_3-related reflections disappeared, suggesting a partial or complete reduction of this phase to Mo^0, as evidenced by the appearance of the Mo-metallic peak. This result is also consistent with the *in situ* XANES data, which show a significant decrease in Mo^{6+} content accompanied by a corresponding increase in Mo^0. In addition, the catalyst maintained an amorphous structure throughout all reduction temperatures, indicating good thermal stability.

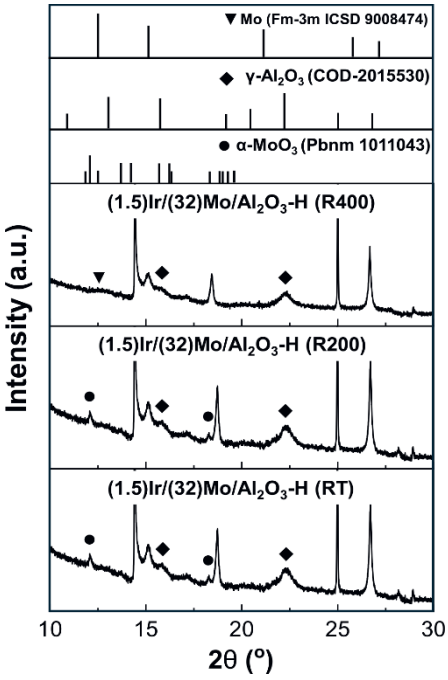


Figure 4.8 The XRD result of the (1.5)Ir/(32)Mo/Al_2O_3-H catalyst after different reduction conditions: room temperature (RT) for the fresh catalyst, at 200 °C (R200), and at 400 °C (R400). Reference patterns for crystalline α-MoO_3 (ICSD 1011043), MoO_2 (ICSD 9008474), and Al_2O_3 (COD 2015530) are provided for comparison. The catalyst shows an amorphous feature overall; the peaks that were not identified correspond to boron nitride (BN) diffraction.

4.3.6.3 The investigation of the surface species difference between each reduction protocol

To further explore the difference in the catalytic activity when changing the reduction protocol, the surface species environment was investigated via *operando* DRIFTS. During the DRIFTS experiment, the catalyst (1.5)Ir/(32)Mo/Al_2O_3-H was reduced using the selected reduction protocols (R200 and R400). After reduction, the temperature was lowered to 150 °C, and the pressure was increased to 10 bar using helium. Following these steps, the H_2/CO_2 = 3 feed was introduced. The spectra were collected during the reaction. The analysis was conducted across three regions, as mentioned previously. The carbonyl region (1900 - 2100 cm^{-1}) obtained from the (1.5)Ir/(32)Mo/Al_2O_3-H when applying the R200 reduction protocol is shown in Figure 4.9 (b). When applying the R400 reduction protocol, the results are shown in Figure 4.5 (b).

The spectra of the carbonyl region for R200 show the emergence of four distinct bands, 2010, 2067, 2077, and 2094 cm^{-1}. The assignment of those bands was already discussed in section 2.5, where the 2077 cm^{-1} band is assigned to linear carbonyl species over metallic Ir [8–10]. The bands at 2067 and 2094 cm^{-1} are assigned to dicarbonyl over Ir [8–10,12]. The band at 2010 cm^{-1} is assigned to Ir-bridged carbonyl species [12]. R400 spectra are also discussed in Section 2.5. The band at 2010 cm^{-1} was not observed in the case of R400, indicating the absence of Ir-bridged carbonyl species at R400. Furthermore, the peak-to-peak ratio between 2077 and 2067 cm^{-1} varied between the R200 and R400. Although *in situ* XANES analysis (Figure 4.7 (a)) revealed no substantial change in the Ir oxidation state, the observed spectral differences suggest a modification in Ir dispersion or surface site distribution, leading to this change in the collected spectra. Additionally, the catalytic activity presented in Figure 4.6 shows that applying the R200 reduction results in a CO_2 conversion that is four times higher than that obtained after R400. This difference is attributed to a faster hydrogenation reaction, likely due to a higher number of accessible Ir active sites following reduction at 200 °C, indicating the different Ir environment after applying each reduction protocol. This difference in the Ir environment can be further confirmed by the difference in the collected spectra, as shown in Figure 4.5 (b) for R400 and 4.9 (b) for R200. Thus, it is also suggested that the Ir plays also a significant role in this difference in catalytic performance.

The (C-O) region of (1.5)Ir/(32)Mo/Al_2O_3-H using R200 is shown in Figure 4.9 (a), and using R400 is shown in Figure 4.4 (b). The spectra when R200 was applied indicate the existence of five distinct bands, at 1394 with a shoulder at 1367, 1452, 1587, 1618, and 1646 cm^{-1} (Figure 4.9 (a)). The bands at 1394 and 1587 cm^{-1} correspond to formate species [7,13]. To confirm if this formate is type I, the C-H stretching vibration, which normally appears at 2904 cm^{-1}, was investigated. In this case, the spectra of the C-H region, shown in Figure 4.6-S, Appendix, do not show this band. However, another bands were observed at 2917 and 2955 cm^{-1}, indicating a new formate type. Additionally, the bands at 1367 and 1618 cm^{-1} correspond to formate type II, as previously explained. The monodentate band, normally observed at 1325 cm^{-1}, and its C-H stretching, shown as a shoulder at 2895 cm^{-1}, were not observed in this case. However, the spectra at R400 (Figure 4.4(b)) show the existence of six distinct bands: 1324, 1392, 1453, 1589, 1612, and 1642 cm^{-1}, which were explained and assigned in Section 2.4.

It is worth mentioning that the formate species types I and monodentate formate were not observed when R200 was implemented. At the same time,

the catalytic activity indicates very minimal MeOH-derived product selectivity. This observation is consistent with our finding that formate type I and monodentate formate are the key intermediates for high selectivity toward MeOH-derived products. In addition, formate type II was absent when the reduction protocol R400 was used, but present when R200 was used, indicating that formate type II is not directly related to the formation of high levels of MeOH-derived products.

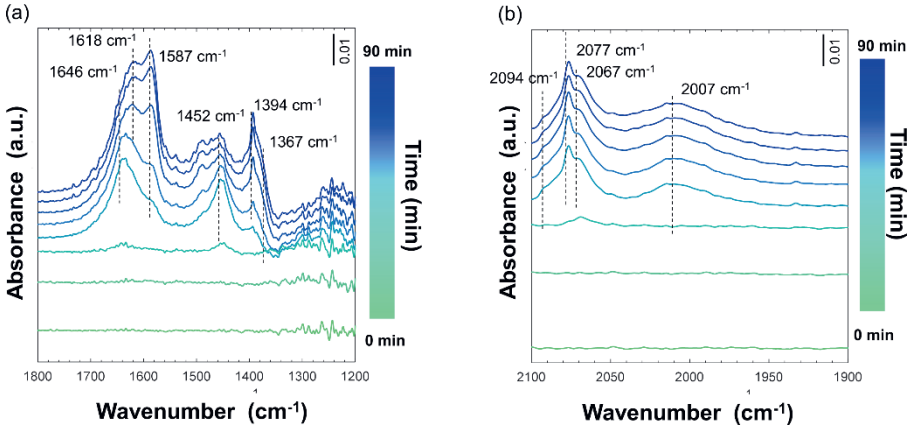


Figure 4.9 Temporal evolution of surface species obtained from the *operando* DRIFTS during CO_2 hydrogenation at 150 °C and 10 bar over (1.5)Ir/(32)Mo/Al_2O_3-H when applying the reduction protocol R200 **(a)** the (C-O) region (1200 - 1800 cm^{-1}) **(b)** the carbonyl vibration region (1900 - 2100 cm^{-1})

4.4 Conclusion

This study demonstrates that Mo dispersion, along with Mo loading, plays a decisive role in determining the structural, electronic, and catalytic properties of Ir/Mo/Al_2O_3 catalyst for CO_2 hydrogenation. By preparing two catalysts with identical Mo loading but different Mo dispersions, it was demonstrated that highly dispersed Mo species significantly influence both the catalytic activity and the surface species environment. Catalytic testing revealed that Mo dispersion significantly influences product selectivity. Under the R400 reduction protocol, the highly dispersed Mo catalyst ((1.5)Ir/(32)Mo/Al_2O_3-H) exhibited exceptional MeOH-derived product selectivity (97%), whereas the low dispersed Mo catalyst ((1.5)Ir/(32)Mo/Al_2O_3-L) produced mainly CO. *Operando* DRIFTS confirmed that formate type I and monodentate formate intermediates correlate strongly

with high MeOH selectivity. Moreover, the second temperature sequence was also implemented over (1.5)Ir/(32)Mo/Al_2O_3-H, and the result revealed the opposite behavior, with a decline in MeOH selectivity observed, which is found to be due to the increase in Mo^{4+} content, as confirmed by the XANES data. Finally, the reduction protocol investigation was also performed, which indicated that R200 resulted in high CH_4, while R400 resulted in almost full MeOH-derived product selectivity. The chemical state of Mo was investigated using XANES, which revealed a significant change in the Mo chemical state when the reduction protocol was altered. The surface species investigated using *operando* DRIFTS confirm our finding regarding the formate type I and monodentate formate intermediates, which were found to be the active intermediates for MeOH formation, since they were observed when R400 was implemented and were absent when R200 was implemented.

References

[1] X. Zhang, Y. Xu, D. Li, Y. Zhang, The effect of metal ions doping on the electrochemical performance of molybdenum trioxide, Electrochimica Acta 283 (2018) 149–154.

[2] Y. Pepe, Y. Tutel, A.D. Ucar, E. Cevik, A. Karatay, H.E. Unalan, A. Elmali, Enhanced nonlinear absorption and photoluminescence properties of Zn, Fe, Cu, V and Ni doped MoO_3 transition metal oxide thin films, Physica Scripta 99 (2024).

[3] D.K. Ponelakkia, K.M. Eswari, V. Balaji, P. Sakthivel, S. Asaithambi, R. Yuvakkumar, G. Ravi, Enhanced pseudocapacitive performance of transition metal doped MoO3 nanorods, Electrochimica Acta 511 (2025).

[4] G.S. Medeiros Leão, M.D. Silva Ribeiro, R.L. de F. Filho, L.B. Saraiva, R.R. Peña-Garcia, A.P. de C. Teixeira, R.M. Lago, F.A. Freitas, S. de Sá Barros, S.D. Junior, Y.L. Ruiz, F.X. Nobre, The Synergic Effect of h-MoO_3, α-MoO_3, and β-MoO_3 Phase Mixture as a Solid Catalyst to Obtain Methyl Oleate, ACS Applied Materials and Interfaces 16 (2024) 60103–60121.

[5] M.H. Wai, J. Ashok, N. Dewangan, S. Das, S. Xi, A. Borgna, S. Kawi, Influence of Surface Formate Species on Methane Selectivity for Carbon Dioxide Methanation over Nickel Hydroxyapatite Catalyst, ChemCatChem 12 (2020) 6410–6419.

[6] N. Ishito, K. Hara, K. Nakajima, A. Fukuoka, Selective synthesis of carbon monoxide via formates in reverse water – gas shift reaction over alumina-supported gold catalyst, Journal of Energy Chemistry 25 (2016) 306–310.

[7] D. Heyl, U. Rodemerck, U. Bentrup, Mechanistic Study of Low-Temperature CO_2 Hydrogenation over Modified Rh/Al_2O_3 Catalysts, ACS Catalysis 6 (2016) 6275–6284.

[8] M. Mihaylov, E. Ivanova, F. Thibault-Starzyk, M. Daturi, L. Dimitrov, K. Hadjiivanov, New types of nonclassical iridium carbonyls formed in Ir-ZSM-5: A fourier transform infrared spectroscopy investigation, Journal of Physical Chemistry B 110 (2006) 10383–10389.

[9] G.A. Ozin, A.J. Lee Hanlan, Rhodium and Iridium Atom Chemistry: Binary Carbonyls of Rhodium and Iridium, Inorganic Chemistry 18 (1979) 2091–2101.

[10] R. Della Pergola, L. Garlaschelli, F. Demartin, M. Manassero, N. Masciocchi, Chemistry of iridium carbonyl cluster complexes. Synthesis, chemical characterization and solid state structure of the mixed-metal carbonyl cluster $[PPh_4][Ir_6(\mu\text{-}CO)_3(CO)_{12}\{\mu 3\text{-}Cu(NCMe)\}] \cdot CH_2Cl_2$ and its conversion to the dianion $[Ir_{12}(CO)_{26}]^{2-}$, J. Organomet. Chem. 436 (1992) 241–253.

[11] M. Cowie, G. Vasapollo, B.R. Sutherland, J.P. Ennett, Inorganic Chemistry Concepts, Springer Verlag, (1986).

[12] Russell Howe, An infrared study of a supported Iridium cluster carbonyl complex, J. Catal. (1977).

[13] A. Bansode, B. Tidona, P.R. Von Rohr, A. Urakawa, Impact of K and Ba promoters on CO_2 hydrogenation over Cu/Al_2O_3 catalysts at high pressure, Catal. Sci. Technol. 3 (2013) 767–778.

Appendix

Chapter 4

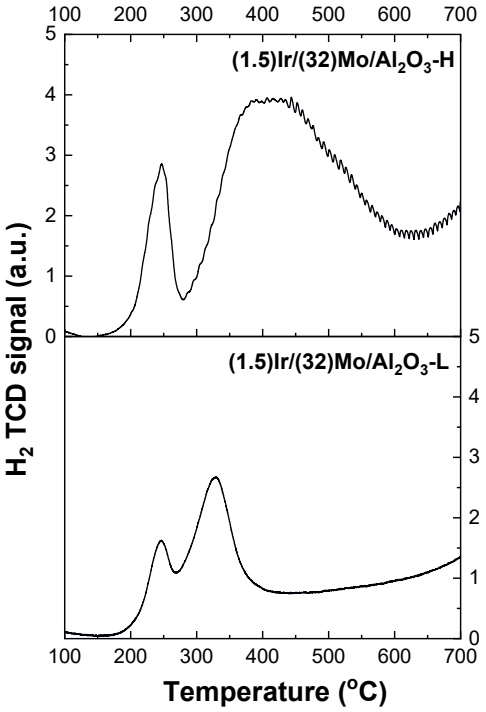


Figure 4.1-S H_2 reduction profile of (1.5)Ir/(32)Mo/Al_2O_3-H and -L, which was performed under hydrogen from room temperature to 700 °C

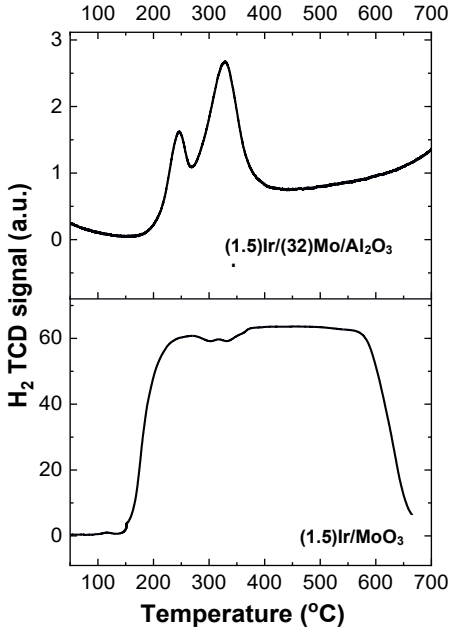


Figure 4.2-S H_2 reduction profile of (1.5)Ir/(32)Mo/Al_2O_3-L and (1.5)Ir/MoO_3, which was performed under hydrogen from room temperature to 700 °C

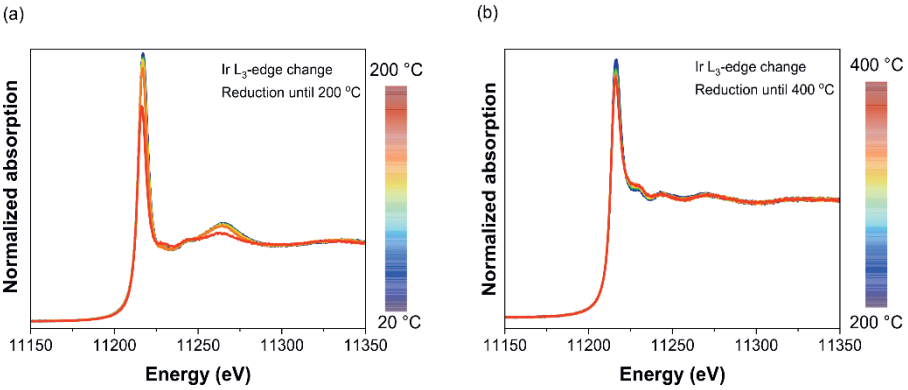


Figure 4.3-S *In situ* XANES results obtained during the reduction of the (1.5)Ir/(32)Mo/Al_2O_3-H system showing the progressive change in Ir L_3-edge. The reduction protocol used is **(a)** R200 and **(b)** R400. The result indicates that the reduction of Ir species started when the temperature reached ~ 160 °C, but when R400 was implemented, no significant change was observed

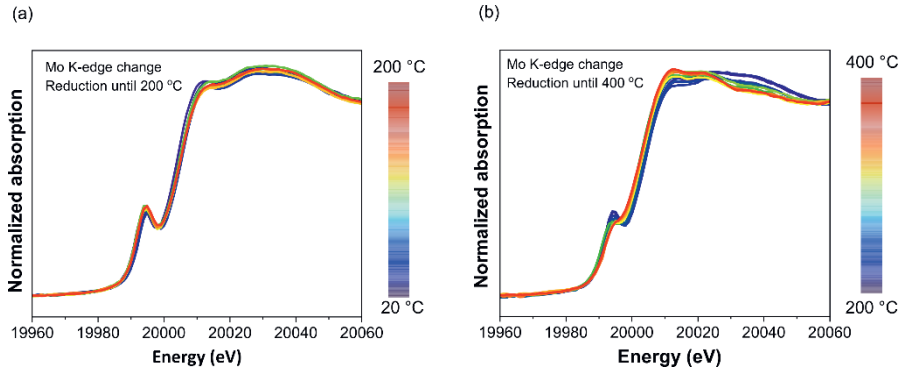


Figure 4.4-S *In situ* XANES results obtained during the reduction of the (1.5)Ir/(32)Mo/Al_2O_3-H system showing the progressive change in Mo K-edge. The reduction protocol used is **(a)** R200 and **(b)** R400. The result indicates no significant change when R200 was implemented, but when R400 was implemented, a change in the pre-edge feature was observed at ~260 °C

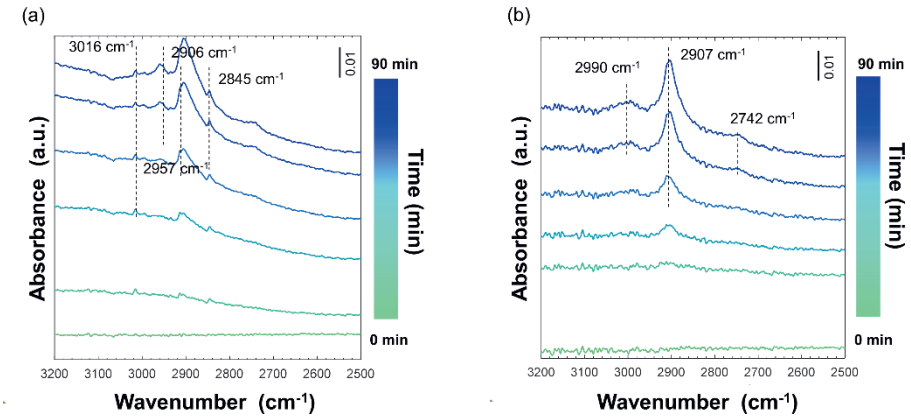


Figure 4.5-S Surface species evolution that was obtained during the *operando* DRIFTS experiment at 150 °C and 10 bar under CO_2 hydrogenation using the R400 reduction protocol. The results shown correspond to the C-H region (2500 - 3200 cm^{-1}) of **(a)** (1.5)Ir/(32)Mo/Al_2O_3-L and **(b)** (1.5)Ir/(32)Mo/Al_2O_3-H

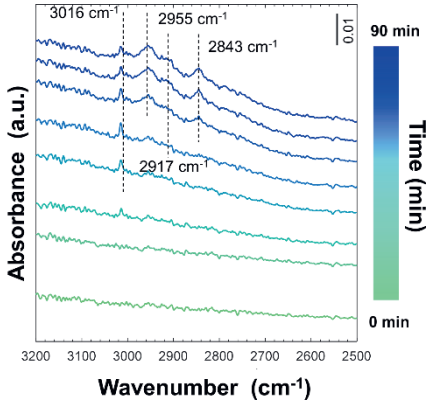


Figure 4.6-S Surface species evolution that was obtained during the *operando* DRIFTS experiment at 150 °C and 10 bar under CO_2 hydrogenation using the R200 reduction protocol. The results shown correspond to the C-H region (2500 - 3200 cm^{-1}) of (1.5)Ir/(32)Mo/Al_2O_3-H

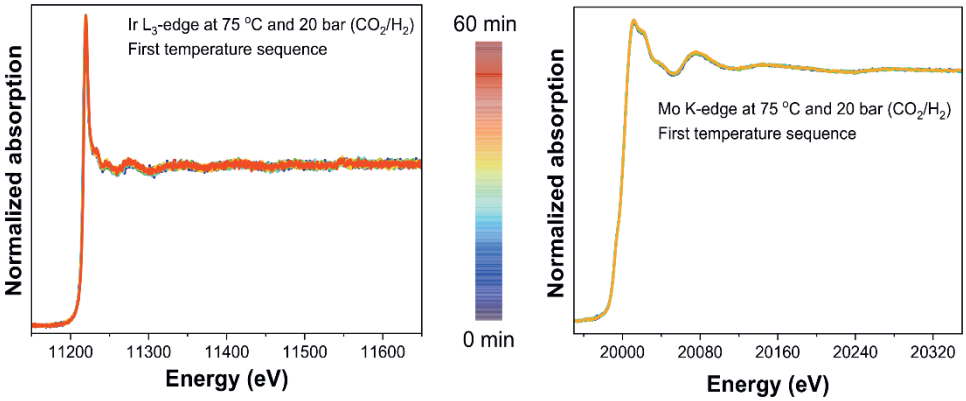


Figure 4.7-S *In situ* XANES results obtained for the (1.5)Ir/(32)Mo/Al_2O_3-H at 20 bar and 75 ºC (first temperature sequence) under CO_2/H_2 feed. Left side is the Ir L_3-edge and right side is the Mo K-edge. The spectra collected after reaching and fixing the temperature at 75 ºC for 60 min.

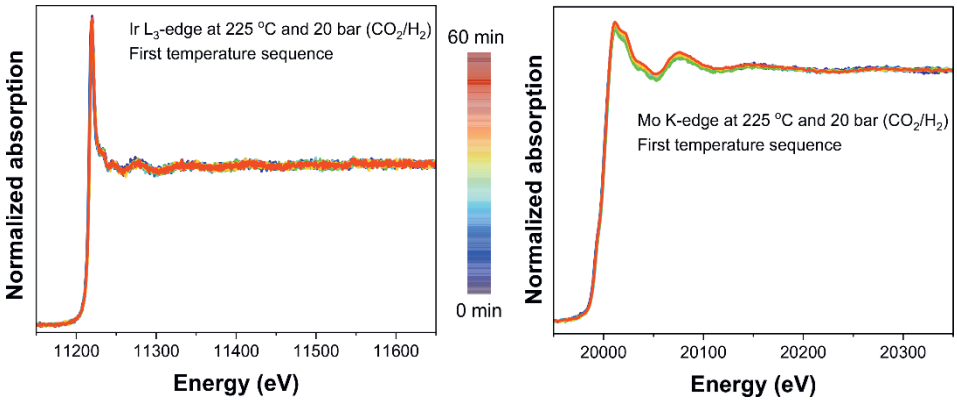


Figure 4.8-S *In situ* XANES results obtained for the (1.5)Ir/(32)Mo/Al_2O_3-H at 20 bar and 225 °C under CO_2/H_2 feed. Left side is the Ir L_3-edge and right side is the Mo K-edge. The spectra collected after reaching and fixing the temperature at 75 °C for 60 min.

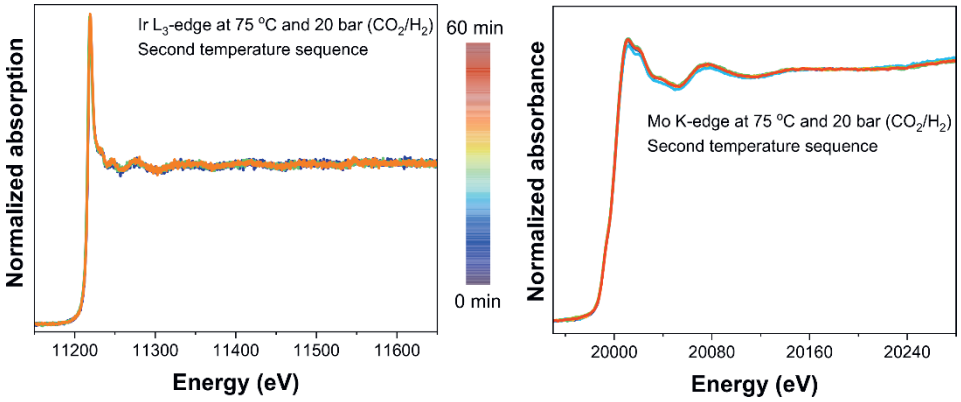


Figure 4.9-S *In situ* XANES results obtained for the (1.5)Ir/(32)Mo/Al_2O_3-H at 20 bar and 75 °C (Second temperature sequence) under CO_2/H_2 feed. Left side is the Ir L_3-edge and right side is the Mo K-edge. The spectra collected after reaching and fixing the temperature at 75 °C for 60 min.

5 On the kinetics of CO_2 hydrogenation to CO on Ir/Mo-based catalytic systems

Martino Saita, Ahmad Alrefaei, José Palomo, Atsushi Urakawa

In preparation
The first three authors contributed equally to this work

Summary

This study investigates the catalytic behavior of Ir/MoO_3 and $Ir/MoO_3/Al_2O_3$ systems in the reverse water-gas shift (RWGS) reaction, a crucial process for converting CO_2 into CO, which is an important feedstock for sustainable fuel synthesis. The catalysts were investigated over a wide range of operating conditions at atmospheric pressure. Both catalytic systems exhibited 100% selectivity toward CO over the entire operational range, confirming their effectiveness and suitability for promoting the RWGS reaction. Stability with time-on-stream experiments revealed partial deactivation at high temperatures for the Ir/MoO_3 catalytic system, attributed to its low surface area and consequent Ir sintering. Conversely, the $Ir/MoO_3/Al_2O_3$ catalytic system exhibited high thermal stability, with no sensitive deactivation with time-on-stream. A comprehensive kinetic study of the RWGS reaction over $Ir/MoO_3/Al_2O_3$ was conducted, assuming a direct CO_2 dissociation pathway with C-O bond cleavage of adsorbed CO_2 as the rate-determining step. Oxygen vacancies in MoO_x were considered the active sites for CO_2 activation, while Ir facilitated H_2 activation and regenerated oxygen vacancies via hydrogen spillover. Kinetic parameters were estimated, yielding a model that accurately described the system's catalytic performance. Sensitivity analysis revealed that CO and H_2O adsorption were negligible, allowing reduction of the number of kinetic parameters from 12 to 8 without loss of predictive accuracy.

5.1 Introduction

In recent times, the ever-increasing amount of post-combustion emissions released into the atmosphere has led to significant increases in pollution levels and climate disruptions [1]. CO_2 is claimed to be one of the primary causes of climate change, as it is by far the most emitted pollutant on a daily mass basis [2]. Driven by global political and social efforts toward decarbonization, carbon capture and storage (CCS) has emerged as a reliable and sustainable approach to mitigate CO_2 emissions from industrial processes. If captured CO_2 is chemically converted with green H_2 to produce products such as CO and methanol (MeOH), new sustainable market solutions can be pursued. The effectiveness and economic feasibility of this strategy significantly depend on the availability of green hydrogen to react with CO_2 [3]. In particular, the Reverse-Water-Gas-Shift (RWGS) reaction is considered a feasible method for transforming CO_2 into CO, which can be used as a raw chemical in other processes, such as MeOH synthesis, Fischer-Tropsch synthesis, and olefin and hydrocarbon production [4]. Due to the endothermic nature of RWGS, high temperatures are required to avoid thermodynamic constraints and achieve high, relevant CO_2 conversion values.

Catalytic approaches are necessary to lower the high activation barrier related to CO_2 activation, which is a consequence of the significant thermodynamic stability of CO_2, thus enabling a higher reaction rate. In particular, thermal catalysis has been the preferred method for promoting this reaction due to its greater scalability and feasibility. In this line, many homogeneous and heterogeneous catalysts have been thoroughly investigated over the years for CO_2 hydrogenation [5], mostly based on transition metals.

Platinum (Pt), palladium (Pd), ruthenium (Ru), nickel (Ni) and rhodium (Rh)-based catalysts are known for their high activity; however, they often suffer from CO selectivity issues due to the strong adsorption of CO on their surfaces, which promotes C-O bond dissociation and subsequent carbon hydrogenation, resulting in the formation of more highly hydrogenated products, such as methane [6]. Among them, Ni-based catalysts such as Ni/Al_2O_3 [7] and Ni/CeO_2 [8] have been widely investigated for CO_2 hydrogenation purposes, given their high activity and lower price compared to the aforementioned transition-noble metal [7]. Despite their remarkable thermal stability and high activity, these catalysts exhibit limited CO selectivity, particularly at lower reaction temperatures, leading to methane formation [7].

On the other hand, Cu-based catalysts have been reported to exhibit weak CO adsorption features, leading to the desorption of this compound without being further hydrogenated, hence attaining a higher CO selectivity [5]. In this line, Cu-based catalysts have been reported to reach up to 100% CO selectivity. However, these materials suffer from sintering because of the high surface mobility of Cu nanoparticles at reaction conditions [9], thus creating challenges for their industrial applicability.

In light of the issues exposed above, catalyst development for the RWGS reaction still requires significant effort to further improve catalytic activity, selectivity, and thermal stability.

Recently, Sun *et al.* [10] reported the use of novel Ir/Mo-based catalytic systems as suitable materials for promoting RWGS. This material has been reported to be remarkably active, selective, and stable for this reaction, achieving 100% CO selectivity at 600 °C. Despite these promising results, there is still no sufficient deep mechanistic understanding or kinetic studies on this catalytic system. It is worth mentioning that this specific system (Ir-Mo) was investigated in the previous Chapters (2, 3, and 4) for its high performance in MeOH synthesis, which can be tuned with reaction conditions. Therefore, it was attractive to test the catalysts and assess their performance under high-temperature and low-pressure conditions. This study could deepen understanding of Ir/Mo-based systems, ultimately leading to rational catalyst design.

In this study, we investigated Ir/Mo-based catalytic systems for the RWGS reaction to gain mechanistic and kinetic insights. A detailed reaction mechanism was proposed and in-depth analyzed, and a kinetic model was developed, which was found to be robust enough to describe the experimental data over a wide range of operating conditions. In addition, the subsequent kinetic analyses identified key steps in the process and the main features of the different compounds present in the catalytic system.

5.2 Experimental section

5.2.1 Catalyst synthesis

The following reagents were used as received. Iridium(III) chloride hydrate ($IrCl_3 \cdot xH_2O$) (CAS No. 10025-83-9) was purchased from Precious Metals Online, and Molybdenum trioxide (MoO_3) (CAS No. 1313-27-5) was obtained

from Alfa Aesar. In addition, MoO_3/Al_2O_3 catalyst (3E) 211456 was supplied by AzkoNobel and used as received as catalyst support.

The Ir-containing catalysts were prepared by the incipient wetness impregnation (IWI) method. The MoO_3 or MoO_3/Al_2O_3 support was previously pelletized and sieved to a particle size of 90-180 μm. The supports were impregnated with an $IrCl_3$ in water solution, containing the corresponding amount of $IrCl_3$ so as to achieve an Ir loading of 6 % in the final calcined catalyst. After impregnation, the resulting material was dried overnight at 120 °C under static air conditions and subsequently calcined at 500 °C for 3 hours. The resulting samples were denoted as Ir/MoO_3 and $Ir/MoO_3/Al_2O_3$.

5.2.2 Characterization of the catalysts

The porous texture of the materials was characterized by N_2 physisorption at -196 °C using a Tristar II 3020 instrument (Micromeritics). Samples were previously outgassed under vacuum overnight at 150 °C. From the N_2 adsorption-desorption isotherm, the apparent surface area (ABET) was determined by applying the BET equation [11].

X-ray diffraction patterns (XRD) of the prepared materials were recorded on a Bruker D8 Advance X-ray diffractometer using Cu Kα radiation (wavelength of 1.5406 Å) at a scan step of 0.05 °/s over the range 5-90°. All patterns were background-subtracted to eliminate contributions from air scatter and potential fluorescence.

The reducibility of the catalysts was studied by temperature programmed reduction (H_2-TPR). In these experiments, 50 mg of the sample was loaded into a quartz fixed-bed microreactor, which was placed inside a vertical furnace with temperature control. The sample was heated from 25 to 700 °C at a heating rate of 10 °C/min, under a constant flow of 30 mL/min (10 % H_2 in Ar). H_2-TPR profile was registered using a TCD detector.

5.2.3 CO_2 hydrogenation catalytic experiments

Catalytic experiments were carried out using a customized laboratory-scale, continuous-flow reaction system provided with a quartz fixed-bed microreactor (i.d. 4 mm). The catalyst bed temperature was controlled by a Watlow heating control with a K-type thermocouple inserted at the end of the catalyst bed. In a typical experiment, the catalyst (pelletized to a 90-180 μm particle size) was loaded in the quartz reactor and fixed with quartz wool. Prior to starting the reaction, the catalyst was *in situ* reduced at 450 °C, under a constant flow of 10 % H_2 in He (50 mL/min), for 90 minutes. Once the

reduction stage was completed, the temperature was set to the reaction value, and the reaction mixture was introduced. Experiments were performed at atmospheric pressure in the temperature range 400 - 550 ºC, with varying space velocity (in the range 40 - 600 NL/g_{cat} h), the H_2 to CO_2 ratio (from 1 to 4), and the CO_2 partial pressure (0.025 - 0.065 bar). The outlet gas concentration was analyzed by gas chromatography (GC, Agilent 7890B, equipped with two FIDs and one TCD). N_2 was used as an internal standard for GC analyses.

CO_2 conversion was defined as the ratio of the amount of CO_2 converted to the amount supplied to the reactor and was expressed in molar %. The selectivity to each product, also expressed in molar %, was defined as the ratio of carbon moles in a specific product to the moles of CO_2 converted.

5.3 Result and discussion

5.3.1 Catalytic activity result

The catalytic activity of the Ir-based catalysts, Ir/MoO_3 and Ir/MoO_3/Al_2O_3, was evaluated in CO_2 hydrogenation at atmospheric pressure over the temperature range 400 - 550 °C, and the results are shown in Figure 5.1. At these temperatures, the RWGS reaction was observed to occur, with 100% selectivity towards CO at all studied temperatures. Catalytic experiments at different space velocities were also conducted, with the results showing a higher CO_2 conversion value with reducing the space velocity, while keeping the high selectivity to CO at all the studied conditions (see Table 5.1-S), for both Ir/MoO_3 and Ir/MoO_3/Al_2O_3 catalytic systems, which evidences the high activity and selectivity for the RWGS reaction.

When comparing the catalytic activity of both systems, it was noticed that Ir/MoO_3 achieved a higher CO_2 conversion than Ir/MoO_3/Al_2O_3 (see Figure 5.1). However, it is important to mention that stability tests, performed for both catalytic systems, with the results shown in Figure 5.1-S, evidenced a deactivation process with time on stream for the Ir/MoO_3 system, which was accentuated at high temperatures (≥ 500 °C). Conversely, Ir/MoO_3/Al_2O_3 showed no deactivation with time on stream, and the attainment of a steady state CO_2 conversion value.

The loss of activity with time on stream, intensified at high temperatures, observed for the Ir/MoO_3 catalyst, is consistent with a deactivation process due to sintering of the active metal [12]. The sintering of the active Ir metal is

not surprising considering the low specific surface area of the MoO_3 support, which was calculated as 3.98 m^2/g, using the BET method (see Figure 5.2-S(a)). This low surface development may hinder the dispersion of Ir species, making it more prone to agglomeration under high-temperature reaction conditions. These larger Ir particles lose active surface area, thus catalytic activity. Conversely, the MoO_3/Al_2O_3 support presented a much higher porosity and specific surface, with a BET surface area value larger than 220 m^2/g (see Figure 5.2-S(b)). This considerably higher textural development in the support promoted a better dispersion and may have led to a more stable anchoring of Ir particles, hindering the agglomeration process leading to sintering of these metal particles. In addition to the evident increase in the textural properties, it is worth mentioning the presence of Al_2O_3 in the Ir/MoO_3-Al_2O_3 catalytic system, which can also impact the Ir-support interactions. To investigate this latter effect, H_2-TPR was conducted on the studied catalysts (see Figure 5.3-S). For the $Ir/MoO_3/Al_2O_3$ catalytic system, the results showed that the H_2 consumption peak associated with the reduction of the Ir species appeared at a temperature of 250 °C, whereas the reduction process for the Ir/MoO_3 started at 150 °C. These findings suggest an enhanced metal-support interaction due to the presence of Al_2O_3 in the system, which could minimize the sintering of the Ir phase and, consequently, catalyst deactivation. Besides, H_2-TPR results indicated that the presence of Ir lowered the reduction temperature of MoO_3, which highlights the intimate contact between these two phases in both catalytic systems.

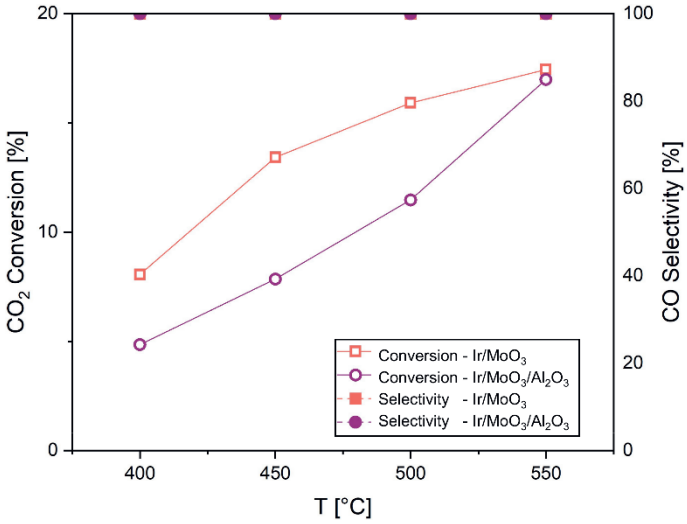


Figure 5.1 Catalytic activity results of CO_2 hydrogenation over Ir/MoO_3 and $Ir/MoO_3/Al_2O_3$ at atmospheric pressure and different temperatures. The CO_2 to H_2 ratio is 1:2, CO_2 partial pressure is 0.05 bar and the space velocity used is 600 NL/g_{cat} h.

Figure 5.2 shows the Arrhenius plots for both catalytic systems, assuming a pseudo-first-order reaction model with respect to CO_2. Apparent activation energies were estimated as 50 and 62 kJ/mol for $Ir/MoO_3/Al_2O_3$ and Ir/MoO_3, respectively. These values are higher than those reported by Sun et al. [13], who estimated a value of 35 kJ/mol for an Ir/MoO_3 catalyst prepared by flame spray pyrolysis. When comparing the values obtained for the two catalytic systems prepared in the present study, it was found that the presence of Al_2O_3 in the catalytic system not only impacted the metal-support interactions and the stability with time on steam, but also slightly lowered the apparent activation energy.

Table 5.1 summarizes the catalytic performance of active catalysts for RWGS. The thermally stable system studied in this work, $Ir/MoO_3/Al_2O_3$, showed superior catalytic performances compared to non-noble metal-based catalysts. $Ir/MoO_3/Al_2O_3$ outperforms 5% Ni/Al_2O_3 [7] from the CO selectivity point of view, while reaching slightly lower conversion, operating at much lower reactant pressure. Moreover, $Ir/MoO_3/Al_2O_3$ was able to convert significantly more CO_2 than $Pd\text{-}In/SiO_2$ [14], a noble metal containing catalyst, even when operating with lower reactant concentrations and residence time. Similarly, $Ir/MoO_3/Al_2O_3$ gave rise to a higher CO yield than 5% Cu/Al_2O_3 [7] even when operating with lower reactant concentration and residence time.

Table 5.1 Catalytic performance data for different systems reported in literature.

Catalyst	**GHSV [L/g_{cat}/h]**	**T [°C]**	**P_{CO2} [bar]**	**P_{H2} [bar]**	**Conv. [%]**	**Sel. [%]**	**Ref.**
MoO_3/Al_2O_3	300	600	0.05	0.1	14.8	100	This work
6% $Ir/MoO_3/Al_2O_3$	300	600	0.05	0.1	30.0	100	This work
5% Ir/MoO_3	300	600	0.24	0.72	44.0	100	[10]
5% Ni/Al_2O_3	240	600	0.4	0.4	35.8	79.7	[7]
5% Cu/Al_2O_3	240	600	0.4	0.4	16.5	100	[7]
3% $Pd\text{-}In/SiO_2$	60	600	0.2	0.2	9.57	100	[14]
4Cu/Al_2O_3 spinel	300	600	0.33	0.66	47.0	100	[15]
0.3% Pt/CeO_2	72	450	0.15	0.45	35.0	98.0	[16]
2% Pt/CeO_2	200	290	0.01	0.04	21.7	100	[17]

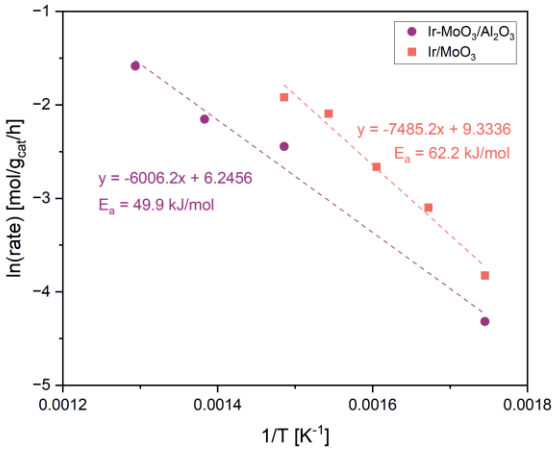


Figure 5.2 Arrhenius plots and apparent activation energies (E_a) of Ir/MoO_3 and $Ir/MoO_3/Al_2O_3$ catalysts.

Overall, the results previously presented evidence of the potential and effectiveness of the prepared materials as a suitable catalyst for promoting the RWGS reaction, especially for the $Ir/MoO_3/Al_2O_3$ catalytic system, which presented not only remarkable activity but also very high stability with time on stream. Therefore, this catalytic system was further studied through a comprehensive kinetic investigation.

5.3.2 Detailed mechanistic and kinetic study

This section presents the results related to the analysis of the reaction mechanism and kinetics -including modelling- of the RWGS reaction on $Ir/MoO_3/Al_2O_3$ catalytic. This includes the identification of plausible detailed reaction pathways, the derivation of the corresponding reaction rate describing the reaction mechanism, the estimation of the associated kinetic parameters, the validation of the model, and a sensitivity analysis for the identification of kinetically relevant reaction steps.

5.3.2.1 Reaction mechanism of RWGS on $Ir/MoO_3/Al_2O_3$

Several studies in the literature report multiple plausible reaction pathways for the reverse RWGS reaction over metal-based catalysts [18]. These studies identify two main reaction mechanisms: the redox mechanism and the associative mechanism [5]. In the redox mechanism, CO_2 acts as an oxidant, donating one of its oxygen atoms to the support, resulting in the formation of

CO as a product. The hydrogen role in this pathway is indirect, facilitating the regeneration of the active sites for the subsequent CO_2 activation and closing the catalytic cycle [5]. In contrast, the associative mechanism involves the direct participation of hydrogen in the reaction by its interaction with adsorbed CO_2, leading to the formation of hydrogen-containing (partially hydrogenated) intermediates such as formate (HCOO*) or carboxyl (COOH*) species, which subsequently decompose to produce CO.

Catalytic systems containing reducible supports, such as TiO_2 and CeO_2, are known to generate oxygen vacancies, which can strongly interact with CO_2, potentially activating the molecule and facilitating its further transformation [19]. In this line, a previous study on $Pt/MoO_x/TiO_2$ identified the redox pathway to occur on MoO_x species during RWGS at 250 °C [20]. The catalytic system analyzed in the present study contains MoO3, which is susceptible to being reduced in the presence of H_2, as can be seen in the H_2-TPR analysis (See Figure 5.3-S). The partial reduction of MoO_3 to MoO_x could lead to the generation of oxygen vacancies, which are one of the proposed active sites for CO_2 activation [21]. Based on this, a direct CO_2 dissociation mechanism (redox pathway) was considered in the present study. Besides, in order to elucidate the role of the different component conforming the catalytic system (i.e., Ir, MoO_3, Al_2O_3) in the reaction mechanism, the catalytic behavior of MoO_3/Al_2O_3 was also addressed. MoO_3/Al_2O_3 showed low-to-moderate activity for CO_2 hydrogenation to CO, and thus it was further investigated from a kinetic and reaction mechanism perspective.

5.3.2.2 Direct CO_2 -redox- dissociation mechanism for MoO_3/Al_2O_3

A parametric study of the RWGS reaction over this catalyst was conducted, with the results, presented in the Appendix (Figure 5.4-S), showing a selectivity to CO close to unity for all the operation conditions analyzed. The catalytic activity of this material was associated with the presence of partially reduced molybdenum oxide species (i.e., MoO_x), which can generate oxygen vacancies that are considered as active sites for the reaction. In line with this single type of active species, one type of active site was assumed for the subsequent reaction mechanism derivation. Table 5.2 presents the elementary steps of the proposed reaction mechanism for the RWGS reaction, in which oxygen vacancies associated with MoO_x serve as the catalytically active sites. This reaction mechanism assumes that CO_2 adsorbs on the active sites (Step 1) and is further activated on the active site via a redox surface reaction (Step 2), yielding an adsorbed carbonyl and an oxidized active site, as reported for other metal oxides [22]. The adsorbed carbonyl species may undergo further hydrogenation to methane. However,

given the high selectivity to CO observed for this catalyst, the only consumption of the carbonyl species was related to its CO desorption (Step 3). Active site regeneration is assumed to be hydrogen-mediated, proceeding through two consecutive elementary steps followed by H_2O desorption (Steps 4-6).

Table 5.2 Elementary steps of the direct CO_2 dissociation reaction mechanism on MoO_3/Al_2O_3.

Reaction step number	Elementary reaction step
1	$CO_{2\,(g)} + * \rightleftharpoons CO_2*$
2	$CO_2* + * \rightleftharpoons CO* + O*$
3	$CO* \rightleftharpoons * + CO_{\,(g)}$
4	$H_{2\,(g)} + 2O* \rightleftharpoons 2OH*$
5	$2OH* \rightleftharpoons O* + H_2O*$
6	$H_2O* \rightleftharpoons * + H_2O_{\,(g)}$

To derive the reaction rate expression, all the steps were considered as reversible elementary reactions, and the mass action law was applied to determine the reaction rate expression for each individual elementary step. C-O bond cleavage (i.e. Step 2) was assumed to be the rate-determining step, and the reaction equilibrium assumption (REA) was considered for the remaining steps. By enforcing the site balance for the active sites, the following reaction rate expression was derived (Eq. 1). See the Appendix for full derivation details.

$$r = \frac{k_{app}\left(P_{CO_2}P_{H_2} - \frac{P_{CO}P_{H_2O}}{K_{eq(T)}}\right)}{P_{H_2}\left(1 + K_{CO}P_{CO} + K_{CO_2}P_{CO_2} + K_{H_2O}P_{H_2O} + K_A\left(\frac{P_{H_2O}}{K_B P_{H_2}} + \frac{P_{H_2O}}{\sqrt{K_B P_{H_2}}}\right)\right)^2} \quad \text{Eq. 1}$$

In this expression, k_{app} represents the apparent kinetic rate constant, defined as the product of k_{intr} and K_{CO2}, where k_{intr} is the intrinsic reaction rate constant (kinetic constant of the r.d.s., i.e., elementary step 2). K_{CO2}, K_{CO}, and K_{H2O} account for the adsorption equilibrium constant of carbon dioxide, carbon monoxide, and water vapor. K_{eq} represents the equilibrium constant of the RWGS reaction, calculated from the thermodynamic properties of the reactants and products. K_A describes the lumped reaction effects of the regeneration of MoO_x sites via consumption of adsorbed OH* species,

production of adsorbed water, and ultimately desorption. K_B describes the equilibrium constant related to the reaction between gas-phase H_2 and the oxygenated sites on MoO_x. P_i represents the partial pressures of the i-th compound.

5.3.2.3 Direct CO_2 -redox- dissociation mechanism for $Ir/MoO_3/Al_2O_3$

The reaction mechanism for the RWGS reaction on $Ir/MoO_3/Al_2O_3$ was developed by extending the previously established mechanism for MoO_3-Al_2O_3 to account for the contribution of Ir. As previously stated, H_2-TPR results (see Figure 5.2-S) indicated that the presence of Ir facilitated the reduction of MoO_3. This was attributed to the high H_2 activation activity of this metal [23], and the close interaction between the Ir and MoO_3 phases within the catalyst. Based on these results, Ir was considered as an active site for hydrogen activation, and the reaction mechanism for MoO_3/Al_2O_3 was integrated with the hydrogenation reactions occurring on Ir. Therefore, two different types of active sites were assumed for the proposed reaction mechanism. Table 5.3 presents the elementary steps included in the RWGS reaction mechanism proposed in the present study. The inclusion of Ir in the catalytic system resulted in three additional elementary steps in the reaction mechanism (Steps 7, 8, and 9). These steps are related to H_2 activation, by dissociative adsorption on an Ir metal active site (Step 7), and the hydrogen spillover from Ir to an oxidized MoO_x active site (in the form of O* or OH*), in a similar fashion to the spillover phenomena reported for Pt/MoO_3 [24]. Subsequent to spillover, adsorbed water vapor is generated (Steps 8 and 9), and it is finally desorbed into the gas phase, closing the catalytic cycle and regenerating MoO_x, the active site. As can be seen in the resulting reaction mechanism, two routes may take place, in parallel, for the regeneration of the MoO_x active sites (i.e., Steps 4 and 5, and Steps 7-9). Given the high hydrogenation activity of Ir, the catalytic route involving this active phase (Steps 7-9) was assumed to be kinetically faster than the direct gas-solid reaction between H_2 and the oxidized sites of the MoO_x phase (Steps 4 and 5). Therefore, these latter steps were neglected for the derivation of the reaction rate expression.

Table 5.3 Elementary steps of the direct CO_2 dissociation reaction mechanism on $Ir/MoO_3/Al_2O_3$.

Reaction step number	Elementary reaction step
1	$CO_{2\,(g)} + * \rightleftharpoons CO_2*$
2	$CO_2* + * \rightleftharpoons CO* + O*$
3	$CO* \rightleftharpoons * + CO_{\,(g)}$
4	$H_{2\,(g)} + 2O* \rightleftharpoons 2OH*$
5	$2OH* \rightleftharpoons O* + H_2O*$
6	$H_2O* \rightleftharpoons * + H_2O_{\,(g)}$
7	$H_{2\,(g)} + 2{\square} \rightleftharpoons 2H{\square}$
8	$O* + H{\square} \rightleftharpoons + OH* + {\square}$
9	$OH* + H{\square} \rightleftharpoons + H_2O* + {\square}$

As in the previous section, all steps were considered as reversible elementary reactions, and the mass action law was applied to determine the reaction rate expression for each individual elementary step. C-O bond cleavage (i.e. Step 2) was assumed to be the rate-determining step, and the reaction equilibrium assumption (REA) was considered for the remaining steps. By applying the site balance to the two distinct active sites, the reaction rate expression was obtained (Eq. 2). Full derivation details can be found in the Appendix.

$$r = \frac{k_{app}\left(P_{CO_2}P_{H_2} - \frac{P_{CO}P_{H_2O}}{K_{eq(T)}}\right)}{P_{H_2}\left(1 + K_{CO}P_{CO} + K_{CO_2}P_{CO_2} + K_{H_2O}P_{H_2O} + K_A\frac{P_{H_2O}}{P_{H_2}} + K_B\frac{P_{H_2O}}{\sqrt{P_{H_2}}}\right)^2} \quad \text{Eq. 2}$$

In this expression, k_{app} represents the apparent kinetic rate constant, defined as the product of k_{intr} and K_{CO2}, where k_{intr} is the intrinsic reaction rate constant (kinetic constant of the rds, i.e., elementary step 2). K_{CO2}, K_{CO}, and K_{H2O} account for the adsorption equilibrium constant of carbon dioxide, hydrogen, carbon monoxide, and water vapor. K_{eq} represents the equilibrium constant of the RWGS reaction, calculated from the thermodynamic properties of the reactants and products. K_A describes the lumped reaction

effects of the regeneration of MoO_x sites via consumption of adsorbed OH* species, production of adsorbed water, and ultimately desorption. K_B describes the equilibrium constant related to the reaction between gas-phase H_2 and the oxygenated sites on MoO_x. P_i represents the partial pressures of the i-th compound.

5.3.2.4 Reactor model and parameters estimation

RWGS catalytic experiments were carried out in a laboratory-scale fixed-bed reactor (i.d. 4 mm) using the $Ir/MoO_3/Al_2O_3$ catalyst diluted with SiC pellets/particles. All experiments were carried out at atmospheric pressure, under isothermal, steady-state conditions. The catalyst particle/pellet size was set to the range of 90-180 μm, aiming to minimize the possible contribution of heat and mass transport limitations. The presence of internal and/or external mass transfer limitations (MTL) was evaluated by applying the Weisz-Prater and Mears' criterion [25], respectively, which indicated the absence of such limitations. The absence of intraparticle and extraparticle heat-transfer limitations was also theoretically checked following the criteria suggested by Moulijn et al. [26]. On the other hand, axial dispersion was evaluated using Mears' criteria [27] and found to be negligible. Therefore, transport limitations were ruled out for the kinetic analysis in the present work. Wall effects were analyzed according to the criteria reported by Perez-Ramirez et al. [28]. Wall effects were neglected, given that the ratio between the bed diameter and the particle diameter is larger than 10. Axial dispersion phenomena were also considered negligible, since the smallest ratio of the bed length and the particle diameter was 50. In addition, it was assumed that the active sites were uniformly distributed on the catalyst surface and that the reactor operated at steady-state conditions. These assumptions allowed us to consider a plug flow integral reactor for the interpretation of the experimental data. The reactor model is obtained by applying the mole balance equation (Eq. 3) to each of the individual species.

$$\frac{\partial F_i}{\partial W_{cat}} = \nu_i \cdot r_i \quad \text{Eq. 3}$$

Where F_i denotes the molar flow rate of species i in mol h^{-1}, W_{cat} is the weight of the catalyst in the bed, ν_i is the stoichiometric factor, and r_i is the reaction rate expression.

The reactor model (i.e., mole balance for the chemical species involved in the reaction mechanism) constitutes a system of ordinary differential

equations that was numerically integrated to estimate the kinetic parameters, namely k_i and K_i, involved in the corresponding reaction mechanism. The dependence on temperature for the kinetic rate constants, k_i, was considered to follow an Arrhenius law (Eq. 4), whereas the equilibrium constant, K_i, was described by the Van't Hoff equation (Eq. 5).

$$k_i = k_{0,i} \exp\left(\frac{-E_{a,i}}{RT}\right) \quad \text{Eq. 4}$$

$$K_i = K_{0,i} \exp\left(\frac{-\Delta H_i}{RT}\right) \quad \text{Eq. 5}$$

In these equations (Eq. 4 and 5), $k_{0,i}$ and $K_{0,i}$ are the preexponential factor, R is the universal gas constant, T is the temperature, $E_{a,i}$ is the activation energy, and ΔH_i is the enthalpy of adsorption/reaction.

The kinetic parameters were estimated by numerically integrating the reactor model equations and minimizing an objective (cost) function defined as the mean absolute relative residual (MARR; Eq. 6). CO_2 conversion was used as the comparison variable between experimental data and model predictions. Given the virtually complete selectivity toward CO, CO_2 conversion was equivalent to CO yield. The minimization procedure was performed using a genetic algorithm routine (MATLAB R2024a), followed by local refinement with the built-in lsqnonlin function.

$$\mathrm{MARR}\,[\%] = \frac{1}{N_{exp}} \sum_{i=1}^{N_{exp}} \frac{\left|\chi_i^{exp} - \chi_i^{mod}\right|}{\chi_i^{exp}} \cdot 100 \quad \text{Eq. 6}$$

Physical constraints were imposed during parameter estimation to ensure the physical consistency of the adsorption enthalpies and pre-exponential factors of the adsorption constants (Eqs. 7 and 8) as reported by Vannice et al. [29]:

$$\Delta H_{ads} < 0,\ 0 < -\Delta S_{ads} < S_{gas}^0 \quad \text{Eq. 7}$$

$$K_{i,ads} = K_i^0 \exp\left(\frac{-\Delta H}{RT}\right) = \exp\left(\frac{-\Delta S_{ads}}{RT}\right) \exp\left(\frac{-\Delta H_{ads}}{RT}\right) \quad \text{Eq. 8}$$

No constraints were applied to lumped kinetic terms describing the surface fractional coverage of reaction intermediates. The thermodynamic equilibrium constant, K_{eq} was computed by using thermodynamic data from [30].

5.3.2.5 Kinetic modelling results for MoO_3/Al_2O_3

Table 5.4 summarizes the kinetic parameter values of the activation energy or enthalpy of adsorption and the preexponential factors ($k_{0,i}$, $K_{0,i}$) for the reactions implied in the proposed mechanism for the MoO_3/Al_2O_3, obtained from the numerical fitting of the experimental data to the reaction model schemed in section 2.2.1. The results showed an activation energy value of 101 kJ/mol. In addition, low values were obtained for the adsorption constant values of CO and H_2O, indicating a weak interaction of these components with the catalyst surface. This weak CO-catalyst interaction implies rapid CO desorption upon formation and is consistent with the high CO selectivity observed for this catalyst. This is also consistent with DFT studies and experimental data, which indicate that CO adsorption is weak in systems presenting a high selectivity towards CO [31]. Figure 5.3 shows the parity plot containing the CO_2 conversion calculated by the kinetic model vs. the experimental CO_2 conversions. As can be seen, a good agreement can be found between the experimental and calculated datasets (MARR = 10.91 %), with the majority of the points lying within the 10 % deviation. These results indicated that the reaction mechanism and kinetic model developed in this study are consistent with the experimental observations and can effectively describe the catalytic behavior of the system.

Table 5.4 Kinetic parameters of the MoO_3/Al_2O_3 kinetic model.

Kinetic parameter	k^0 or K_i^0	Unit	E_a or ΔH_{ads}	Unit
k_{app}	5.7894E+03	mol/h/g_{cat}/bar	48.7996	kJ/mol
K_{CO}	8.3309E-10	bar^{-1}	-23.6350	kJ/mol
K_{CO_2}	3.5353E-03	bar^{-1}	-52.6434	kJ/mol
K_{H_2O}	2.3537E-10	bar^{-1}	-50.3730	kJ/mol
K_A	1.071eE-04	bar^{-1}	-41.5248	kJ/mol
K_B	2.2871E-03	bar^{-1}	-1.2290	kJ/mol

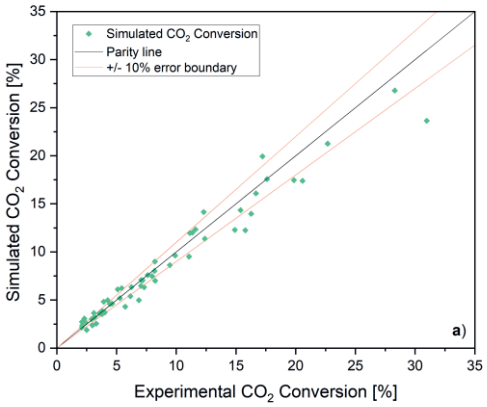


Figure 5.3 Parity plot resulting from the MoO_3/Al_2O_3 kinetic model.

5.3.2.6 Kinetic modelling results for Ir/MoO_3/Al_2O_3

As previously stated in section 2.2.2, the reaction mechanism for the RWGS reaction on $Ir/MoO_3/Al_2O_3$ was developed by extending the MoO_3/Al_2O_3 mechanism to account for the contribution of Ir through the addition of elementary steps associated with active-site regeneration. This latter set of reactions was assumed to be predominant over those present in the MoO_3/Al_2O_3 catalytic system. To confirm the validity of this assumption, the kinetic model developed for MoO_3/Al_2O_3 was used to fit the experimental data for $Ir/MoO_3/Al_2O_3$, and the results are shown in Figure 5.5-S. The catalytic performance of the Ir-containing system cannot be described by the kinetic model developed for MoO_3/Al_2O_3, which accounts for only approximately 12% of the experimentally observed activity (see Appendix for calculation details). This discrepancy highlights the critical role of Ir in promoting the RWGS reaction and confirms the validity of the initial assumption.

Table 5.5 presents the estimated values of the kinetic parameters associated with the reactions included in the proposed $Ir/MoO_3/Al_2O_3$ mechanism, obtained by numerical fitting of the experimental data to the reaction model described in section 5.2.2.2. The activation energy of the intrinsic reaction kinetic constant showed a value of 51 kJ/mol, which is lower than the one obtained for the MoO_3/Al_2O_3. This activation energy value is in line with the apparent measured activation energy of other active RWGS

catalysts, such as Pd/Al_2O_3 [32] and Cu/CeO_2 [33]. The adsorption constant values for CO and H_2O were very low, indicating, for this catalytic system, a very weak CO-catalyst interaction, in line with the very high CO selectivity observed, and revealing no further sensitive CO-catalyst interaction due to the presence of Ir. Figure 5.4 (a) shows the parity plot of simulated CO_2 vs. experimental CO_2 conversions, and a fairly good agreement is observed, with most of the points lying within 10 % deviation. The computed MARR value was 6.62 %. The quality and robustness of the kinetic model are also observed in Figure 5.4 (b), which presents the CO_2 conversion as a function of temperature for different H_2:CO_2 ratios at the reactor inlet. The CO_2 conversion values predicted by the model are shown in solid lines for comparison, and it is remarkable that there is good agreement between the experimental data and the calculated values provided by the model.

Table 5.5 Kinetic parameters of the $Ir/MoO_3/Al_2O_3$ kinetic model.

Kinetic parameter	k^0 or K_i^0	Unit	E_a or ΔH_{ads}	Unit
k_{app}	1.2271E+03	mol/h/g_{cat}/bar	24.2139	kJ/mol
K_{CO}	5.6237E-07	bar^{-1}	-0.4671	kJ/mol
K_{CO_2}	2.1344E-01	bar^{-1}	-26.9993	kJ/mol
K_{H_2O}	1.3915E-09	bar^{-1}	-2.1486	kJ/mol
K_A	4.0543E-02	-	-43.4498	kJ/mol
K_B	1.0048E-01	$bar^{-0.5}$	-30.4451	kJ/mol

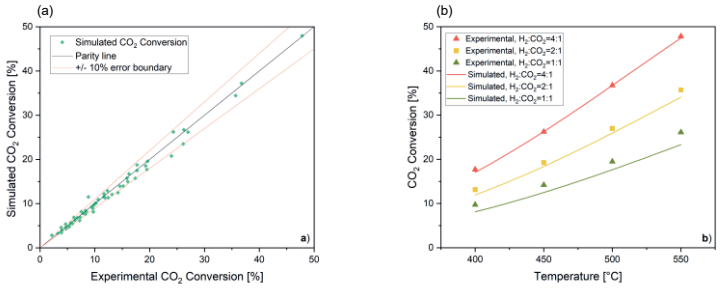


Figure 5.4 (a) Parity plot for the $Ir/MoO_3/Al_2O_3$ kinetic model. **(b)** Comparison of simulated and experimental CO_2 conversion at 80 NL/g_{cat}/h and P_{CO2}=0.05 bar.

Figure 5.5 presents the simulated evolution of CO_2 conversion, the fraction of free active sites, and the fractional coverage of the intermediate species

involved in the RWGS reaction mechanism on $Ir/MoO_3/Al_2O_3$ as a function of the dimensionless reactor coordinate for a constant temperature of 500 °C. The fractional coverages corresponding to the CO and H_2O were negligible as compared to the rest of the surface species and the fraction of free sites. On the other hand, the fractional coverage of free sites, i.e. oxygen vacancies present in the MoO_x phase, decreased as advancing in the reactor. This effect could arise from the progressive depletion of H_2 as advancing in the reactor, which reduces the availability of activated Ir-H species necessary for fully regenerating the active sites, thereby increasing the fractional coverage of oxidized surface species, O* and OH*.

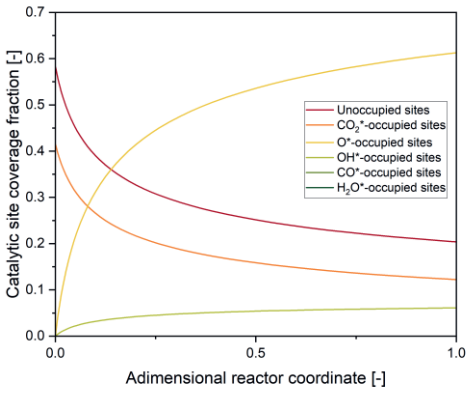


Figure 5.5 Simulation of site (oxygen vacancies) coverage along the reactor coordinate at 500°C, 300 $NL/g_{cat}/h$, P_{CO2}=0.05 bar, and P_{H2}=0.1 bar.

5.3.2.7 *Ir/MoO₃/Al₂O₃ model simplification*

Kinetic models usually involve a large number of parameters. Reducing this number is highly desirable, especially for reactor design and simulation purposes, where reducing computational effort is critical. Nevertheless, this model simplification must be carried out carefully, while preserving the chemical essence of the process. The analysis of the fractional coverages shown in the previous section highlighted the predominance of some surface species. This indicated that the developed kinetic model could be simplified through proper data analysis and kinetic interpretation. This objective was achieved through a sensitivity analysis.

The sensitivity analysis and simplification procedure were applied to the adsorption terms. For this, sensitivity coefficients were computed for each adsorption term to identify which parameters are essential for model accuracy

and which can be neglected without compromising predictive capability. For more information about the sensitivity analysis procedure and details about the calculation, please refer to the Appendix.

Figure 5.6 shows the scaled sensitivity bars for each adsorption term in each rate equation. Negative values imply a reduction in the reaction rate associated with the corresponding adsorption term. Conversely, positive values imply an increase in the reaction rate associated with this parameter. The magnitude of the sensitivity bar corresponds to the parameter's impact on the overall reaction rate. The results show that CO and H_2O adsorption terms have a negligible effect on the overall reaction rate. This is in line with the low fractional coverage calculated for the surface species generated by the adsorption of these two species. On the other hand, the highest relative value of sensitivity bars was found for the kinetic parameters that describe the fractional coverage of the oxidized active sites, namely: O* and OH*, especially the former.

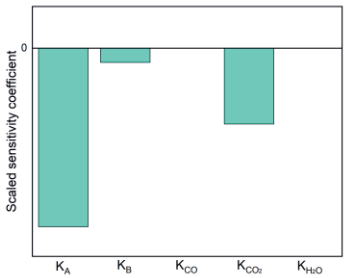


Figure 5.6 Scaled sensitivity bars for the kinetic parameters of the $Ir/MoO_3/Al_2O_3$ model.

Based on these results, the model was simplified by neglecting the terms associated with CO and H_2O adsorption, which, mechanistically, assumes the desorption of these two species (steps 3 and 6 in Table 5.3) to be instantaneous. This simplification process reduces the number of kinetic parameters from 12 to 8 and yields a new reaction rate expression governing the process, shown in Eq. 9.

$$r = \frac{k_{app}\left(P_{CO_2}P_{H_2} - \frac{P_{CO}P_{H_2O}}{K_{eq(T)}}\right)}{P_{H_2}\left(1 + K_{CO_2}P_{CO_2} + K_A\frac{P_{H_2O}}{P_{H_2}} + K_B\frac{P_{H_2O}}{\sqrt{P_{H_2}}}\right)^2} \qquad \text{Eq. 9}$$

Figure 5.6-S compares the performance of the simplified model to the original rate equation by showing the parity plots for both models. As shown, the simplified models can still represent the experimental data with excellent accuracy. The MARR values were 6.62% and 6.70% for the original (full) and simplified models, respectively. These results further confirm that the model simplification, based on mechanistic understanding and sensitivity analysis, did not compromise the accuracy of the original model.

5.4 Conclusions

The RWGS reaction was investigated over two catalytic systems, Ir/MoO_3 and $Ir/MoO_3/Al_2O_3$, at high-temperature and atmospheric-pressure conditions. Catalytic performance experiments revealed that both Ir/MoO_3 and $Ir/MoO_3/Al_2O_3$ are highly active and fully selective toward CO formation at elevated temperatures, confirming the dominance of the RWGS reaction pathway. Ir/MoO_3 showed a deactivation with time on stream, which was accentuated at higher temperatures, and was related to sintering of the active phase. Conversely, $Ir/MoO_3/Al_2O_3$ exhibited superior thermal stability and resistance to deactivation, with the attainment of a stable catalytic activity, which was associated with its higher surface area provided by the alumina, allowing a much higher dispersion of the active phases.

A comprehensive kinetic study of the RWGS reaction over the $Ir/MoO_3/Al_2O_3$ catalyst was conducted, assuming a direct CO_2 dissociation pathway in which C-O bond cleavage of adsorbed CO_2 was the rate-determining step. The detailed reaction mechanism was developed stepwise, with a first mechanistic and kinetic inspection of the MoO_3/Al_2O_3 component of the catalytic system, followed by the inclusion of the elementary steps associated with Ir. Oxygen vacancies associated with MoO_x were considered as the catalytically active sites for CO_2 activation. The role of the Ir metal phase was associated with H_2 activation and its subsequent involvement in the catalytic cycle, through the regeneration of oxygen vacancies via hydrogenation of oxidized surface species via hydrogen spillover.

Kinetic parameters were estimated, minimizing the mean absolute relative residual (MARR). The resulting kinetic model demonstrated excellent accuracy in representing the catalytic behavior of the RGWS process on this catalyst. The kinetic model developed for the $Ir/MoO_3/Al_2O_3$ catalyst was simplified through detailed mechanistic inspection and sensitivity analysis of

the estimated parameters, in which sensitivity coefficients were computed to identify those essential for model accuracy. The analysis revealed that CO and H_2O adsorption were negligible. Consequently, the number of kinetic parameters was reduced from 12 to 8, without compromising the accuracy of the resulting simplified model. These results further validated this model simplification process, based on mechanistic understanding and sensitivity analysis.

In conclusion, and in correlation with the findings presented in Chapter 4, Chapter 5 provides valuable insights into the effect of Ir dispersion on catalytic activity. Under high-temperature conditions, Ir sintering was observed, leading to a decrease in dispersion. This observation is consistent with the results in Chapter 4, where variations in Ir dispersion were identified under different reduction conditions during the DRIFTS investigation, despite no significant change in the chemical state of Ir

References

[1] IEA, «CO_2 Emissions in 2023,» 2023.

[2] M. Filonchyk et al, «Greenhouse gas emissions and reduction strategies for the world's largest greenhouse gas emitters,» *Science of The Total Environment,* vol. 944, n. 15, pp. 9221-9232, 2021.

[3] A. Alvarez et al, «Challenges in the Greener Production of Formates/Formic Acid, Methanol, and DME by Heterogeneously Catalyzed CO_2 Hydrogenation Processes,» vol. 117, n. 14, pp. 9804-9838, 2017.

[4] D. Williamson et al, «N-Doped Fe@CNT for Combined RWGS/FT CO 2 Hydrogenation,» *ACS Sustainable Chemistry and Engineering,* vol. 7, n. 7, pp. 7395-7402, 2019.

[5] M. L. Trivino et al., «Transforming CO_2 to valuable feedstocks: Emerging catalytic and technological advances for the reverse water gas shift reaction,» *Chemical Engineering Journal,* vol. 487, 2024.

[6] A. M. Bahmanpour et al., «Recent progress in syngas production via catalytic CO_2,» *Applied Catalysis B: Environmental,* vol. 295, n. 0926-3373, 2021.

[7] E. Gioria et al, «Boosting the performance of Ni/Al_2O_3 for the reverse water gas shift reaction through formation of CuNi nanoalloys,» *Catalysis Science and Technology,* vol. 12, pp. 474-487, 2022.

[8] J. Gandara-Loe et al., «Design of Full-Temperature-Range RWGS Catalysts: Impact of Alkali Promoters on Ni/CeO_2,» *Energy & Fuels,* vol. 36, n. 12, p. 6362-6373, 2022.

[9] R.-P. Ye et al., «Recent progress in improving the stability of copper-based catalysts for hydrogenation of carbon-oxygen bonds,» *Catalysis Science & Technology,* vol. 8, n. 14, pp. 3428-3449, 2018.

[10] X. Sun et al., «Reaction-induced unsaturated Mo oxycarbides afford highly active CO_2 conversion catalysts,» *Nature Chemistry,* vol. 16, p. 2044-2053, 2024.

[11] S. Brunauer, P. H. Emmet, E. Teller, «Adsorption of Gases in Multimolecular Layers,» *Journal of the American Chemical Society,* vol. 60, n. 2, pp. 309-319, 1938.

[12] C. H. Bartholomew, «Mechanisms of catalyst deactivation,» *Applied Catalysis A: General,* vol. 212, n. 1-2, pp. 17-60, 2001.

[13] X. Sun et al., «Reaction-induced unsaturated Mo oxycarbides afford highly active CO_2 conversion catalysts,» *Nature Chemistry,* vol. 16, pp. 2044-2053, 2024.

[14] J. Ye et al., «Effect of PdIn bimetallic particle formation on CO_2 reduction over the Pd-In/SiO_2 catalyst,» *Chemical Engineering Science,* vol. 135, pp. 193-201, 2015.

[15] A. Bahamanpour et al., «Cu-Al spinel as highly active and stable catalyst for the reverse water gas shift reaction,» *ACS Catalysis,* vol. 9, pp. 6243-6251, 2019.

[16] Z. Zhao et al., «Atomically dispersed Pt/CeO_2 catalyst with superior CO selectivity in reverse water gas shift reaction,» *Applied Catalysis B: Environmental,* vol. 291, 2021.

[17] A. Goguet et al., «Study of the origin of the deactivation of a Pt/CeO_2 catalyst during reverse water gas shift (RWGS) reaction,» *Journal of Catalysis,* vol. 226, n. 2, pp. 382-392, 2004.

[18] Y. A. Daza e J. N. Kuhn, «CO_2 conversion by reverse water gas shift catalysis: comparison of catalysts, mechanisms and their consequences for CO_2 conversion to liquid fuels,» *RCS Advances,* vol. 6, n. 55, p. 49675-49691, 2016.

[19] M. Zhu et al., «Catalytic Reduction of CO_2 via Reverse Water Gas Shift reaction: recent Advances in the Design of Active and Selective Supported Metal Catalysts,» *Transactions of Tianjin,* vol. 26, pp. 172-187, 2020.

[20] S. Mine et al., «Reverse water-gas shift reaction over Pt/MoO_x/TiO_2: reverse Mars-van Krevelen mechanism via redox of supported MoOx,» *Catalysis Science and Technology,* vol. 11, pp. 4172-4180, 2021.

[21] A. Goguet et al., «Spectrokinetic Investigation of Reverse Water-Gas-Shift Reaction Intermediates over a Pt/CeO_2 Catalyst,» *Journal of Physical Chemistry B,* vol. 108, n. 52, pp. 20240-20246, 2004.

[22] «Recent Advances in Supported Metal Catalyst and Oxide Catalyst for the Reverse Water-Gas Shift Reaction,» *Frontiers in Chemistry,* vol. 8, 2020.

[23] S. Subramanian e J. A. Schwarz, «Structure and Activity of Composite Oxide-Supported Iridium and Platinum Catalysts,» *Journal of Catalysis,* vol. 7, pp. 201-212, 1991.

[24] J. G. Kim e J. R. Regalbuto, «The Effect on Calcination on H2 Spillover on Pt/MoO_3,» *Journal of Catalysis,* vol. 139, n. 1, pp. 175-190, 1993.

[25] D. Mears, «Tests for Transport Limitations in Experimental Catalytic Reactor,» *Industrial & Engineering Chemistry Process Design and Development,* vol. 10, n. 4, pp. 541-547, 1971.

[26] J. A. Moulijn et al., «General aspects of catalyst testing,» *Catalysis Today,* vol. 11, n. 1, pp. 1-12, 1991.

[27] D. E. Mears, «The role of axial dispersion in tricke-flow laboratory reactors,» *Chemical Engineering Science,* vol. 26, pp. 1361-1366, 1971.

[28] J. Perez-Ramirez et al., «The six-flow reactor technology. A review on fast catalyst screening and kinetic studies,» *Catalysis Today,* vol. 60, pp. 93-109, 2000.

[29] M. Vannice et al., «Entropies of Adsorption in Heterogeneous Catalytic Reactions,» *Journal of Catalysis,* vol. 56, n. 3, pp. 358-362, 1979.

[30] C. Yaws, «Yaw's Handbook of Thermodynamic Properties and Chemical Compounds,» 2003.

[31] L. Dietz, S. Piccinin e M. Maestri, «Mechanistic Insights Into CO_2 Activation Via Reverse Water-Gas Shift On Metal Surfaces,» *Journal of Physical Chemistry,* vol. 119, n. 9, p. 4959-4966, 2015.

[32] X. G. Wang et al., «Constructing efficient Pd/Al_2O_3 catalyst for reverse water-gas shift via alkali-modification,» *Chemical Engineering Journal,* vol. 500, n. 156937, 2024.

[33] K. Kandasamy et al., «Insights into Mechanisms of Reverse Water Gas ShiftActivity Enhancement over Reverse Microemulsion-Synthesized $CuCeO_2$,» *ChemNanoMat,* vol. 10, n. 11, 2024.

[34] The Mathworks Inc., «MATLAB Version R2024b,» 2024.

[35] X. Zhang et al, «Highly dispersed Copper over β-Mo_2C as Efficient and Stable Catalysts for RWGS Reaction,» *ACS Catalysis,* vol. 7, 2016.

Appendix
Chapter 5

Table 5.1-S CO_2 conversion [%] and CO selectivity [%] on Ir/MoO_3/Al_2O_3 and Ir/MoO_3 at 400°C and at different space velocities and partial pressures of reactants.

Catalyst	GHSV [L/g_{cat}/h]	P_{CO2}=0.025 bar P_{H2}=0.05 bar		P_{CO2}=0.05 bar P_{H2}=0.05 bar		P_{CO2}=0.065 bar P_{H2}=0.05 bar	
		Conv.	Sel.	Conv.	Sel.	Conv.	Sel.
Ir/MoO_3/Al_2O_3	450	7.22	100	4.03	100	3.22	100
	600	4.66	100	3.60	100	2.16	100
Ir/MoO_3	450	12.32	100	6.34	100	5.03	100
	600	11.27	100	5.31	100	4.04	100

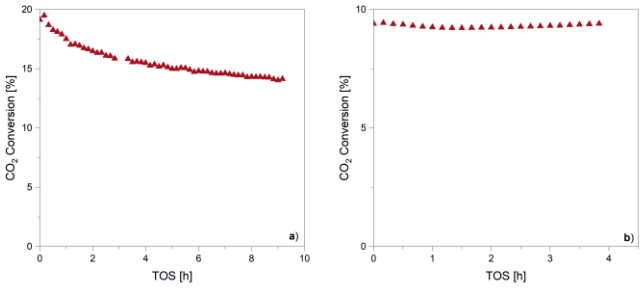


Figure 5.1-S Conversion vs time on stream (TOS) of **(a)** Ir/MoO_3 and **(b)** Ir/MoO_3/Al_2O_3 at 500°C and the same feed conditions.

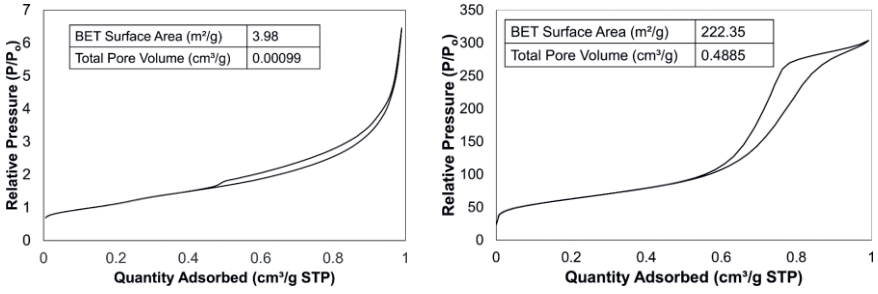


Figure 5.2-S N_2 adsorption-desorption isotherms of **(a)** Ir/MoO_3 and **(b)** Ir/MoO_3/Al_2O_3.

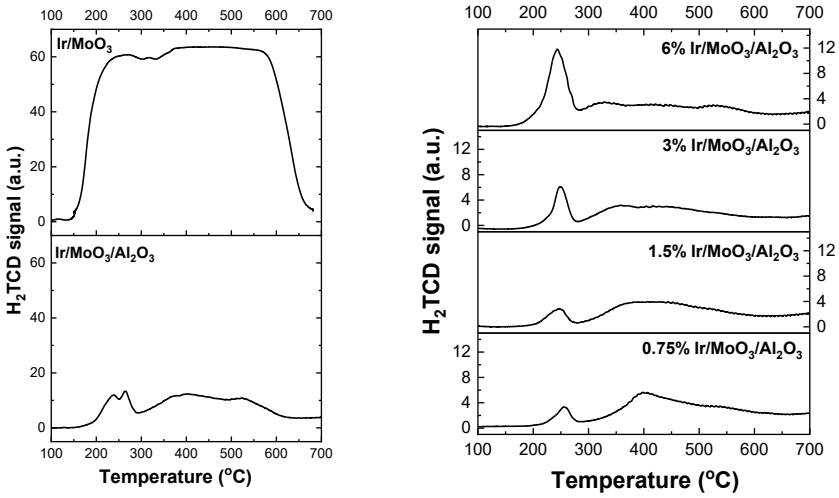


Figure 5.3-S H_2-TPR result of **(a)** the Ir/MoO_3 and $Ir/MoO_3/Al_2O_3$ systems and **(b)** $Ir/MoO_3/Al_2O_3$ systems with different Ir content.

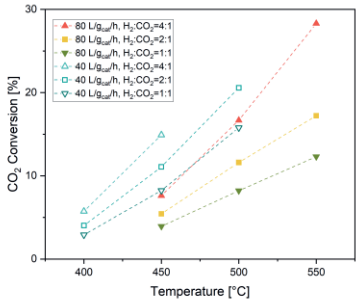


Figure 5.4-S Example of the results of the parametric study on MoO_3/Al_2O_3. Data obtained at P_{CO2}=0.05 bar.

Derivation of the kinetic models

The following steps describe the derivation of the mechanism for MoO_3/Al_2O_3, according to the steps shown in Table 2 of the main manuscript. The symbol $\theta_{Mo,i}$ is used to quantify the surface coverage fraction of the i-th adsorbed species on MoO_x sites. θ_{Mo} is used to quantify the fraction of unoccupied MoO_x sites. θ_{Ir} is used to quantify the fraction of unoccupied Ir sites and $\theta_{Ir/H}$. It is used to quantify hydrogen that dissociates and is adsorbed on Ir sites.

Table 5.3-S Mathematical development steps for the MoO_3/Al_2O_3 reaction rate.

Step	Reaction rate	Mathematical elaboration
1	$r_1 \approx 0 = k_1 P_{CO_2} \theta_{Mo} - k_{-1} \theta_{Mo/CO2}$	$\theta_{Mo/CO2} = K_1 P_{CO_2} \theta_{Mo}$
2	$r = r_2 = k_2 \theta_{Mo/CO_2} \theta_{Mo} - k_{-2} \theta_{Mo/CO} \theta_{Mo/O}$	$r = k_2 K_1 P_{CO_2} \theta_{Mo}^2 - k_{-2} \frac{P_{H_2O} P_{CO} \theta_{Mo}^2}{K_3 K_4 K_5 K_6 P_{H_2}}$
3	$r_3 \approx 0 = k_3 \theta_{Mo/CO} - k_{-3} P_{CO} \theta_{Mo}$	$\theta_{Mo/CO} = K_3^{-1} P_{CO} \theta_{Mo}$
4	$r_4 \approx 0 = k_4 P_{H_2} \theta_{Mo/O}^2 - k_{-4} \theta_{Mo/OH}^2$	$\theta_{Mo/H_2O} = K_6^{-1} P_{H_2O} \theta_{Mo}$
5	$r_5 \approx 0 = k_5 \theta_{Mo/OH}^2 - k_{-5} \theta_{Mo/O} \theta_{Mo/H_2O}$	$\theta_{Mo/O} = \frac{P_{H_2O} \theta_{Mo}}{K_4 K_5 K_6 P_{H_2}}$
6	$r_6 \approx 0 = k_6 \theta_{Mo/H_2O} - k_{-6} P_{H_2O} \theta_{Mo}$	$\theta_{Mo/OH} = \frac{P_{H_2O} \theta_{Mo}}{K_5 K_6 \sqrt{K_4 P_{H_2}}}$

The site balance on Mo-type sites (oxygen vacancies) yields:

$$1 = \theta_{Mo} + \theta_{Mo/CO} + \theta_{Mo/CO_2} + \theta_{Mo/H_2O} + \theta_{Mo/O} + \theta_{Mo/OH}$$

$$1 = \theta_{Mo} \left(1 + K_3^{-1} P_{CO} + K_1 P_{CO_2} + K_6^{-1} P_{H2O} + \frac{P_{H_2O}}{K_4 K_4 K_5 P_{H2}} + \frac{P_{H_2O}}{K_5 K_6 \sqrt{K_4 P_{H2}}} \right)$$

Proceeding with the derivation, the site balance and the expression of the rate equation can be combined and rearranged:

$$r = \frac{k_2 K_1 \left(P_{CO_2} P_{H_2} - \frac{P_{H_2O} P_{CO}}{K_1 K_2 K_3 K_4 K_5 K_6} \right)}{P_{H_2} \left(1 + K_3^{-1} P_{CO} + K_1 P_{CO_2} + K_6^{-1} P_{H_2O} + \frac{P_{H_2O}}{K_4 K_5 K_6 P_{H2}} + \frac{P_{H_2O}}{K_5 K_6 \sqrt{K_4 P_{H2}}} \right)^2}$$

In particular, K_3^{-1} represents the adsorption constant of CO, K_1 the adsorption constant of CO_2 and K_6^{-1} the adsorption constant of H_2O. Moreover, at thermodynamic equilibrium, the following two conditions are verified:

$$\begin{cases} r = 0 \\ \frac{P_{CO_2} P_{H_2}}{P_{H_2O} P_{CO}} = K_{eq}(T) \end{cases}$$

By imposing such conditions, it follows that $K_1 K_2 K_3 K_4 K_5 K_6 = K_{eq}(T)$. Finally, $k_2 K_1$ are lumped in a single kinetic term k_{app} describing the apparent kinetic constant (while k_2 represents the intrinsic kinetic constant). Finally, K_5 and K_6 into the term K_A. Finally, the rate expression for MoO_3/Al_2O_3 is obtained:

$$r = \frac{k_{app} \left(P_{CO_2} P_{H_2} - \frac{P_{CO} P_{H_2O}}{K_{eq}(T)} \right)}{P_{H_2} \left(1 + K_{CO} P_{CO} + K_{CO_2} P_{CO_2} + K_{H_2O} P_{H_2O} + K_A \left(\frac{P_{H_2O}}{K_B P_{H_2}} + \frac{P_{H_2O}}{\sqrt{K_B P_{H_2}}} \right) \right)^2}$$

The following steps describe the derivation of the mechanism for $Ir/MoO_3/Al_2O_3$, according to the steps shown in Table 3 of the main manuscript.

Table 5.4-S Mathematical development steps for the $Ir/MoO_3/Al_2O_3$ reaction rate.

Step	Reaction rate	Mathematical elaboration
1	$r_1 \approx 0 = k_1 P_{CO_2} \theta_{Mo} - k_{-1} \theta_{Mo/CO2}$	$\theta_{Mo/CO2} = K_1 P_{CO_2} \theta_{Mo}$
2	$r = r_2 = k_2 \theta_{Mo/CO_2} \theta_{Mo} - k_{-2} \theta_{Mo/CO} \theta_{Mo/O}$	$r = k_2 K_1 P_{CO_2} \theta_{Mo}^2 - k_{-2} \frac{P_{H_2O} P_{CO} \theta_{Mo}^2}{K_3 K_6 K_7 K_8 K_9 P_{H_2}}$
3	$r_3 \approx 0 = k_3 \theta_{Mo/CO} - k_{-3} P_{CO} \theta_{Mo}$	$\theta_{Mo/CO} = K_3^{-1} P_{CO} \theta_{Mo}$
6	$r_6 \approx 0 = k_6 \theta_{Mo/H2O} - k_{-6} P_{H_2O} \theta_{Mo}$	$\theta_{Mo/H2O} = K_6^{-1} P_{H_2O} \theta_{Mo}$
7	$r_7 \approx 0 = k_7 P_{H_2} \theta_{Ir}^2 - k_{-7} \theta_{Ir/H}^2$	$\theta_{Mo/H2O} = \theta_{Ir} \sqrt{K_7 P_{H_2}}$
8	$r_1 \approx 0 = k_8 \theta_{Mo/O} \theta_{Ir/H} - k_{-1} \theta_{Mo/OH} \theta_{Ir}$	$\theta_{Mo/O} = \frac{P_{H_2O} \theta_{Mo}}{K_6 K_7 K_8 K_9 P_{H_2}}$
9	$r_9 \approx 0 = k_9 \theta_{Mo/OH} \theta_{Ir/H} - k_{-9} \theta_{Mo/H2O} \theta_{Ir}$	$\theta_{Mo/OH} = \frac{P_{H_2O} \theta_{Mo}}{K_6 K_9 \sqrt{K_7 P_{H2}}}$

The site balance on Mo-type sites (oxygen vacancies) yields:

$$1 = \theta_{Mo} + \theta_{Mo/CO} + \theta_{Mo/CO_2} + \theta_{Mo/H_2O} + \theta_{Mo/O} + \theta_{Mo/OH}$$

$$1 = \theta_{Mo} \left(1 + K_3^{-1} P_{CO} + K_1 P_{CO_2} + K_6^{-1} P_{H2O} + \frac{P_{H_2O}}{K_6 K_7 K_8 K_9 P_{H2}} + \frac{P_{H_2O}}{K_6 K_9 \sqrt{K_7 P_{H2}}} \right)$$

Proceeding with the derivation, the site balance and the expression of the rate equation can be combined and rearranged:

$$r = \frac{k_2 K_1 \left(P_{CO_2} P_{H_2} - \frac{P_{H_2O} P_{CO}}{K_1 K_2 K_3 K_6 K_7 K_8 K_9} \right)}{P_{H_2} \left(1 + K_3^{-1} P_{CO} + K_1 P_{CO_2} + K_6^{-1} P_{H_2O} + \frac{P_{H_2O}}{K_6 K_7 K_8 K_9 P_{H_2}} + \frac{P_{H_2O}}{K_6 K_9 \sqrt{K_7 P_{H_2}}} \right)^2}$$

In particular, K_3^{-1} represents the adsorption constant of CO, K_1 the adsorption constant of CO_2 and K_6^{-1} the adsorption constant of H_2O. Moreover, at thermodynamic equilibrium, the following two conditions are verified:

$$\begin{cases} r = 0 \\ \frac{P_{CO_2} P_{H_2}}{P_{H_2O} P_{CO}} = K_{eq}(T) \end{cases}$$

By imposing such conditions, it follows that $K_1 K_2 K_3 K_6 K_7 K_8 K_9 = K_{eq}(T)$. Finally, $k_2 K_1$ are lumped in a single kinetic term k_{app} describing the apparent kinetic constant (while k_2 represents the intrinsic kinetic constant). Finally, products of kinetic terms such as K_6, K_7, K_8 and K_9 into the respective terms K_A and K_B. Finally, the rate expression for $Ir/MoO_3/Al_2O_3$ is obtained:

$$r = \frac{k_{app}\left(P_{CO_2}P_{H_2} - \frac{P_{CO}P_{H_2O}}{K_{eq}(T)}\right)}{P_{H_2}\left(1 + K_{CO}P_{CO} + K_{CO_2}P_{CO_2} + K_{H_2O}P_{H_2O} + K_A\frac{P_{H_2O}}{P_{H_2}} + K_B\frac{P_{H_2O}}{\sqrt{P_{H_2}}}\right)^2}$$

Analysis of kinetic mechanisms

It is of interest to evaluate how much the performance of the MoO_3/Al_2O_3 model is distant from the ability to accurately represent the experimental data of $Ir/MoO_3/Al_2O_3$. Figure 5.5-S(a) shows the parity plot resulting from the attempt to reproduce $Ir/MoO_3/Al_2O_3$ data with the MoO_3/Al_2O_3 mechanism. It is clear that MoO_3/Al_2O_3, being less active than $Ir/MoO_3/Al_2O_3$, yielded a kinetic model that consistently underestimates the conversion on Ir-MoO_3/Al_2O_3. A more in-depth analysis was also performed: the rate equation of MoO_3/Al_2O_3 (with the previously estimated parameters) is implemented in a parameter optimization script, as well as the rate equation of $Ir/MoO_3/Al_2O_3$ with no kinetic parameters implemented a priori. Hence, the reactor mole balance is described by Eq. S1:

$$\frac{\partial F_i}{\partial W_{cat}} = \nu_i \cdot \left(r_{MoO_3/Al_2O_3} + r_{Ir/MoO_3/Al_2O_3}\right) \qquad \text{Eq. S1}$$

Combining the two rate equations conceptually describes the interaction of Ir-poor regions of $Ir/MoO_3/Al_2O_3$, simulated with the MoO_3/Al_2O_3 model, and Ir-rich regions. Quantifying the numerical contributions of the Ir-rich regions highlights the critical role of Ir in promoting RWGS, providing grounds for neglecting steps 4 and 5 in Table 5.3 in the main manuscript. After estimating the missing kinetic parameters, the numerical contributions of Ir-poor regions in the i-th experiment are computed by comparing the total amount of CO_2 converted to the amount converted by Ir-poor regions only. In mathematical terms, the computation is described by Eq. S2:

$$\text{contribution}_i = \frac{\int_0^{W_{cat}} r_{MoO_3/Al_2O_3}\, dW_{cat}}{\int_0^{W_{cat}} r_{MoO_3/Al_2O_3}\, dW_{cat} + \int_0^{W_{cat}} r_{Ir-MoO_3/Al_2O_3}\, dW_{cat}} \qquad \text{Eq. S2}$$

Figure 5.5-S(b) demonstrates that integrating the two rate equations can accurately describe the experimental data with MARR = 7.08%. Figure 5.5-S (c) quantifies the contributions of the MoO_3/Al_2O_3 mechanism, which accounts for only 12% on average of the total converted CO_2. The result indicates that

the $Ir/MoO_3/Al_2O_3$ system can be successfully modelled with a single rate equation derived from the assumption of homolytic dissociation of H_2 on Ir.

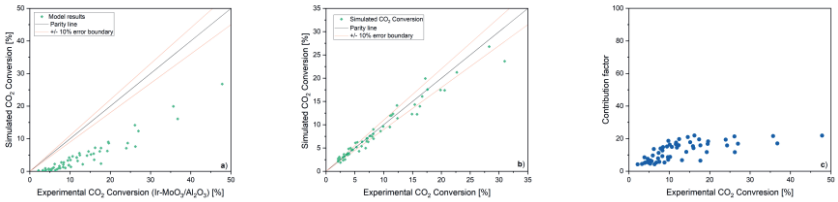


Figure 5.5-S (a) Parity line resulting from the attempt to model $Ir/MoO_3/Al_2O_3$ experimental data with the MoO_3/Al_2O_3 model **(b)** Parity line resulting from the refitting of the two-rate model **(c)** mapping for the MoO_3/Al_2O_3 model contribution with respect to $Ir/MoO_3/Al_2O_3$ data.

Sensitivity analysis

The method is based on the evaluation of the sensitivity coefficients $S_{i,j}$ that describes the extent of change of the i-th variable of interest (or objective function) with respect to the j-th parameter. To make sensitivity coefficients comparable, they should be normalized and nondimensionalized. In this study, the impact of each kinetic term at the denominator of the rate equation (K_j) on the modelled CO_2 conversion (χ_i) was computed, then an averaged value for each conversion datapoint was estimated, ultimately resulting in the sensitivity bar plots. CO_2 conversion is used as the objective function since it is directly related to the numerical behavior of the rate equation.

$$S_{i,j} = \frac{K_j}{\chi_i} \cdot \frac{\partial \chi_i}{\partial K_j}$$

Sensitivity analysis can be performed according to different procedures and normalization techniques. In this study, the use of a brute-force approach was deemed sufficient. Hence, multiple numerical perturbations were applied to each K_j term ($\pm$10%, $\pm$20%, $\pm$30%), thus resulting in the value ∂K_j. Then, the numerical ODE system was solved multiple times for each perturbation value, ultimately resulting in an average $S_{i,j}$ coefficient. The resulting sensitivity coefficients, plotted as bars, are nondimensional and lack physical meaning, making sensitivity analysis a qualitative rather than quantitative method. Hence, the absolute value of the sensitivity bars is not reported, as relevant insights only lie in comparing the sign and quantitative height between one bar and another.

Comparison of original and simplified Ir-MoO_3/Al_2O_3 models

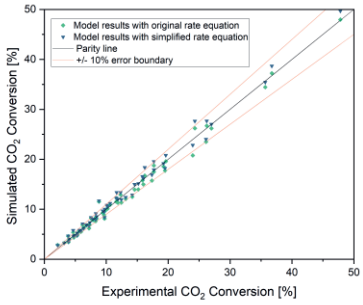


Figure 5.6-S Comparison between the original $Ir/MoO_3/Al_2O_3$ model (all kinetic parameters) and the simplified model.

Conclusions and Outlook

The development of human society has been closely linked to rising energy demand. Despite the progress in energy technologies, fossil fuels continue to dominate the global energy market. With the world's population growing, the development of sustainable, renewable energy solutions has become increasingly urgent. Although renewable energy technologies have expanded rapidly, carbon-intensive industries still play a major role, underscoring the need for carbon capture, utilization, and storage (CCUS) to mitigate emissions. Within CCUS strategies, CO_2 hydrogenation to chemical energy carriers is a particularly attractive pathway for producing clean fuels and value-added chemicals. This reaction is thermodynamically favored at low temperatures and high pressures, necessitating the use of catalysts with excellent selectivity to minimize undesired side reactions and high activity to increase the CO_2 conversion. Recent studies have highlighted the potential of iridium- and molybdenum-based catalytic systems for efficient CO_2 hydrogenation. Iridium catalysts exhibit support-dependent and tunable selectivity, while molybdenum-based materials offer distinctive structural flexibility that promotes CO_2 activation. In this chapter, the outlook of the iridium and molybdenum-based systems was discussed.

Developing high-performance catalysts for low-temperature CO_2 hydrogenation to chemical energy carriers remains a significant challenge. Copper-based catalysts have demonstrated good performance for high methanol (MeOH) selectivity at elevated temperatures. However, overcoming the limitations of this reaction requires efficient operation at lower temperatures, since CO_2 hydrogenation to MeOH is exothermic. Noble metals, such as iridium (Ir), exhibit strong hydrogen-activation capabilities at low temperatures, making them particularly attractive for this application.

This work aimed to elucidate the role of Ir–support interactions in high-pressure CO_2 hydrogenation to MeOH. To this end, Ir was impregnated onto different reducible supports, which were selected based on their previously reported unique interactions with noble metals. Among the systems investigated, Ir/MoO_3 was identified as a highly promising catalyst for further study. Nevertheless, supports with different chemical natures were not explored in this work. Investigating Ir-based catalysts supported on a wider range of support materials with different natures would provide deeper insight into the specific role of Ir-support interactions, as each support can induce distinct electronic and structural effects on the active metal sites.

Following the identification of Ir/MoO_3 as a promising catalytic system, this work focused on developing a comprehensive understanding of the structural and electronic interplay between Ir and Mo species during high-pressure CO_2 hydrogenation. The results presented in **Chapter 2** highlight the critical role of the reduction environment in governing catalytic performance and steering product selectivity toward MeOH. These findings emphasize the importance of exploring the chemical state of both metals under reaction conditions. Accordingly, the chemical states of Ir and Mo were investigated using *in situ* XANES. The results revealed no significant change in the oxidation state of Ir, whereas pronounced changes were observed in the Mo oxidation state. Such variations in the Mo chemical state are expected to strongly influence its interaction with Ir species, ultimately leading to distinct catalytic behaviors. Another key observation was the change in MeOH selectivity during the second temperature sequence. Since the Ir chemical state remained unchanged, this behavior can be attributed to the further reduction of Mo species.

In addition, *operando* DRIFTS was performed on Ir/MoO_3 during the CO_2 hydrogenation. The technique offered valuable insights into the formation and evolution of surface intermediates, particularly formate species, and their role in governing MeOH-derived product selectivity. The enhanced formation of

formate species observed during the second temperature sequence correlates strongly with the increase in MeOH selectivity, reinforcing the role of formate as a key intermediate in methanol synthesis.

Looking forward, further studies are needed to deepen the understanding of the interaction between Ir and Mo, potentially indicating the formation of a unique Ir-Mo interfacial phase. This could be achieved through extended *operando* extended X-ray absorption fine structure (EXAFS) measurements of both metals under reaction conditions to improve structural resolution. The low Ir loading presents a challenge for such analysis, which requires these extended measurements. The extended measurement will provide valuable information on the Ir bonding environment, leading to a deeper understanding of its states under reaction conditions. In summary, the dynamic behavior of the Ir/MoO_3 system clearly arises from the unique interaction between the two metals. These insights could provide a foundation for the rational design of highly efficient catalysts for CO_2 hydrogenation to chemical energy carriers.

Following the identification of changes in Mo's chemical state as a potential driver of the pronounced shift in product selectivity, further efforts were devoted to elucidating the specific role of Mo in the catalytic system. In **Chapter 3**, catalysts with varying Mo loadings were prepared by impregnating Mo onto γ-Al_2O_3 while maintaining a constant Ir loading. The results clearly demonstrate that increasing the Mo loading significantly affects catalytic performance during high-pressure CO_2 hydrogenation to MeOH, with higher Mo loadings leading to lower MeOH selectivity. This observation indicates that excessive Mo content can adversely affect MeOH formation.

Structural characterization revealed that catalysts with higher Mo loading exhibit lower Mo dispersion, whereas those with lower Mo content exhibit much higher dispersion. This finding highlighted the critical role of Mo dispersion, suggesting that the high MeOH selectivity observed at low Mo loading is closely linked to the highly dispersed Mo species. Directed by this finding, **Chapter 4** focused on separating Mo loading from dispersion effects by preparing Mo/γ-Al_2O_3 catalysts with similar Mo loadings but different dispersion states. The catalytic results revealed a clear distinction in MeOH selectivity, with the highly dispersed Mo catalyst exhibiting substantially full selectivity towards MeOH-derived products. These findings confirm that Mo dispersion plays a key role in governing catalytic activity and product selectivity.

Looking ahead, the observation that highly dispersed Mo species can drive almost full selectivity toward MeOH-derived product makes this system

particularly attractive for further exploration. In this context, investigating single-atom Mo catalysts represents a promising direction for future catalyst design for this system. Additionally, further studies could focus on developing preparation strategies that enable high Mo loadings while maintaining high dispersion, thereby combining high metal content with optimal catalytic performance and potentially leading to higher conversion and MeOH selectivity. Furthermore, the selection of Al_2O_3 was based on its high surface area. However, the Al_2O_3 acidity function directed MeOH toward MeOH-derived products, such as methylformate (MF) and dimethyl ether (DME). Investigating the same system with different supports and different natures could possibly lead to full selectivity towards MeOH or one of the derived products.

Previous studies have reported the potential of the Ir/MoO_3 system for the reverse water-gas shift (RWGS) reaction under specific operating conditions. In **Chapter 5**, the performance of Ir/MoO_3 and $Ir/MoO_3/Al_3O_3$ catalysts was systematically evaluated under identical RWGS conditions, followed by a detailed kinetic investigation of the most suitable system. The results demonstrate that $Ir/MoO_3/Al_3O_3$ exhibits high thermal stability across the investigated temperature range, whereas Ir/MoO_3 undergoes partial deactivation at elevated temperatures. Consequently, kinetic modeling was performed exclusively for the $Ir/MoO_3/Al_3O_3$ catalyst.

Looking forward, further investigation of the deactivation mechanisms affecting the Ir/MoO_3 catalyst is recommended, as such an investigation could guide rational catalyst design for RWGS applications and deepen the understanding of Ir-Mo-based catalytic systems under varying reaction conditions. Moreover, as demonstrated in **Chapter 2**, the dynamic evolution of Mo species in the Ir/MoO_3 system under reaction conditions results in significant changes in catalytic activity and selectivity. Therefore, future studies should incorporate *operando* XANES measurements under RWGS conditions to obtain more detailed insight into the chemical states and structural evolution of both Ir and Mo during reaction.

Curriculum Vitae

Ahmad Alrefaei was born on 10 February 1989 in Jeddah, Saudi Arabia. He obtained his Bachelor of Engineering degree in Chemical Engineering from Dalhousie University, Halifax, Canada, in 2012. In the same year, he joined Saudi Aramco as a Process Engineer in the Crude Distillation Unit at the Jeddah Refinery, where he worked until 2015. In 2015, he moved to the Platformer Unit as a Process Engineer, where he developed a strong interest in catalysis. While working at Saudi Aramco, he earned his Master's degree in Chemical Engineering from King Abdulaziz University, Jeddah, Saudi Arabia. In 2018, he transitioned to the Research and Development Department at Saudi Aramco to further expand his expertise in catalysis. During this period, he contributed to several major projects, including CO_2 to olefins, butane dehydrogenation, and the one-step crude-to-chemicals project. In 2020, he decided to pursue a PhD at Delft University of Technology (TU Delft), where he joined the Catalysis Engineering group led by Prof. Atsushi Urakawa. The primary outcomes of his doctoral research are presented in this dissertation. Professionally, he obtained the Professional Engineer (PE) Chemical certification from the National Council of Examiners for Engineering and Surveying (NCEES) in 2017.



